Programmable and Responsive Superhydrophobic Surfaces

Anas Al-Azawi

A! Aalto University

Programmable and Responsive Superhydrophobic Surfaces

Anas Al-Azawi

A doctoral dissertation completed for the degree of Doctor of Science (Technology) to be defended, with the permission of the Aalto University School of Science, at a public examination held online via remote connection link (e.g. Zoom), on 12 March 2021 at 12:00.

Aalto University
School of Science
Department of Applied physics
Soft Matter and Wetting

Supervising professor
Professor Robin Ras, Aalto University, Finland

Thesis advisor
Professor Sami Franssila, Aalto University, Finland

Preliminary examiners
Professor Wouter van der Wijngaart, KTH Royal Institute of Technology, Sweden
Professor Rafael Taboryski, DTU Technical University of Denmark, Denmark

Opponent
Professor Rafael Taboryski, DTU Technical University of Denmark, Denmark

NORDIC SWAN ECOLABEL

Printed matter
4041-0619

Author
Anas Al-Azawi

Name of the doctoral dissertation
Programmable and Responsive Superhydrophobic Surfaces

Abstract

Progress in the field of superhydrophobic surfaces requires precise characterization techniques and synthesis of surfaces that exhibit robust non-wettability. In this thesis, microfabrication techniques are used to produce static as well as bioinspired responsive superhydrophobic structures. In addition, transverse droplet oscillations are implemented to accurately evaluate superhydrophobicity of micropillared surfaces.

  Variations in surface properties that influence the degree of superhydrophobicity were successfully probed by relating friction and viscous dissipation of dynamic droplets to pattern density and chemical coating. Additionally, controlling the normal force exerted on the water-based ferrofluid droplet allows the measurement of impalement pressure necessary to induce wetting transition for a droplet in motion.

  A new fabrication process was introduced for rapid prototyping of cilia-inspired magnetic micropillars. The fabricated array of sub-10 μm diameter pillars are based on polydimethylsiloxane (PDMS) loaded with carbonyl iron particles (CIP). Lubricating in silicone oil allowed controlled droplet motion at the sub-mm scale facilitated by fast actuation and superhydrophobicity of the oil infused PDMS magnetic micropillars. Lack of mechanical stability due to flexibility of the high aspect ratio PDMS micropillars restricted the application of the array to liquid media only. Thiol-ene based magnetic micropillar arrays were introduced to address the stability issue of the high-aspect ratio micropillars. The remarkable properties of thiol-ene including tunability of surface and mechanical properties allowed topography modification of the magnetic micropillars using photo-induced thiol-ene click coupling. Decorating the surface of the high aspect ratio thiol-ene micropillars with polyvinyltrimethoxysilane (PVTMS) colloidal micro- and nanoparticles enhanced the mechanical stability of the flexible micropillars without compromising powerful bending actuation. This allowed actuation of the micropillar arrays in air as well as in liquid media. The magnetic micropillars were rendered superhydrophobic by grafting hydrophobic self-assemnled monolayer onto the PVTMS micro- and nanoparticles that are covalently bonded to the surface. This enabled directed water droplet motion by repetitive bending and recovery of the micropillars.

  Combining mechanical stability with robust superhydrophobicity can lead to numerous practical applications of cilia-inspired thiol-ene magnetic micropillars.

Preface

Before the start of my PhD, the subject of superhydrophobicity has fascinated me. I remember when I was working on my master project in Denmark, the thought of applying micro- and nanostructures that I was developing at that time in DTU Danchip cleanroom into the field of superhydrophobic surfaces was always in my mind. Few months after my graduation, I saw announcement that Aalto University is hiring PhD students and postdoctoral researchers to work on superhydrophobic surfaces. I sent my application without hesitation and later moved to Finland to work on this interesting field.

I would like to express my gratitude to Professor Robin Ras for granting me the opportunity to work in his group, for his trust and for motivating me to aim high when doing research. To be part of Soft Matter and Wetting group was an enjoyment because of the good atmosphere, amazing colleagues and high level of research. I could not succeed without the support and encouragement of my dear group members; Hedar Al-Terke, Mika Latikka, Maja Vuckovac, Topi Tupasela, Tommi Huhtamäki, Isabel Díez, Matilda Backholm, Muhammad Junaid, Kai Liu, Roni Mäenpää and Sakari Lepikko and other members who contributed to the group.

Moreover, I thank my thesis advisor Professor Sami Franssila for integrating me in his group. I value the collaboration and the help that I obtained from the Microfabrication group in Micronova. I would like to especially thank Dr. Ville Jokinen for always giving me a constructive feedback through all these years. My gratitude also extends to current and past members of Microfabrication group; Gianmario Scotti, Akanksha Singh, Sasha Hoshian, Farzin Jahangiri, Giovanni Marin, Maria Berdova, Joonas Heikkinen, Anand Tatikonda, Juan Li and Ville Rontu. I never forget the social atmosphere and the activities that were arranged by Microfabrication and Soft Matter and Wetting groups. These were some of my best memories during my time in Finland.

I appreciate the friendship of Ashkan Bonabi and Benedek Poor from University of Helsinki, whom I met through my work in Micronova.

I am grateful for the support I received from the Department of Applied Physics and from Aalto Nanofab in Micronova. I would like to thank Timo Kajava for taking care of all of the practical issues. Also, I want to thank Pegah Khanjani, Kia Bertula and Amanda Eklund for the assistance in handling orders of chemicals used in my work. The support I received from Aalto Nanofabrication Center at Micronova was also an important factor for the

Risskov, Denmark, January 18, 2021

Anas Al-Azawi

Contents

List of Abbreviations and Symbols

IC	Integrated circuit
ψ	Tilt angle
SEM	Scanning electron microscopy
SA	Sliding angle
SF_6	Sulfur hexafluoride
AR	Aspect ratio
F^*	Fluorine radical
O^*	Oxygen radical
SiF_4	Silicon tetrafluoride
PECVD	Plasma enhanced chemical vapor deposition
CHF_3	Trifluoromethane
G	Gibbs free energy
γ	Liquid-vapor interfacial tension, Surface tension
A	Surface area
n	Number of molecules
P	Pressure
T	Temperature
L	Length
w	Width
F_{ext}	External force
δA	Change in area
δG	Change in Gibbs free energy
δV	Change in volume
$\Delta P_{Y\text{-}L}$	Laplace pressure
R_1, R_2	Radii of curvature
γ_{SL}	Solid-liquid interfacial tension
γ_{SV}	Solid-vapor interfacial tension
S_P	Spreading parameter
θ_{SL}	Equilibrium contact angle on smooth solid surface, Young contact angle

θ	Apparent contact angle
r	Roughness factor
θ_W	Apparent contact angle of the Wenzel state
φ_s	Solid-liquid fraction
θ_C	Apparent contact angle of the Cassie-Baxter state
φ_a	Liquid-air fraction
θ_{LV}	Liquid-vapor contact angle
r_w	Factor of wetted roughness
CAH	Contact angle hysteresis
ACA, θ_A	Advancing contact angle
RCA, θ_R	Receding contact angle
A_{wt}	Wetted area
d	Diameter of cylindrical micropillars
h	Height of cylindrical micropillars
s	Edge-to-edge spacing between the micropillars
A_c	Unit cell area
p	Pitch
G_C	Free energy of the wetting system in Cassie state
G_W	Free energy of the wetting system in Wenzel state
CW transition	Cassie-to-Wenzel transition
$\Delta G_{CW\ transition}$	Surface free energy change associated with CW transition
$\theta_{critical}$	Critical contact angle
P_c	Critical pressure
P_{total}	Total pressure inside a droplet
H_d	Mean depth of a droplet
S	Perimeter of the micropillar
L_{TCL}	Three-phase contact line length
P_{ext}	External pressure
F_{CAH}	Contact angle hysteresis force
F_g	Gravitational force
m	Mass
g	Gravitational acceleration
R	Radius of the drop's contact patch
λ_c	Capillary length
K	Retentive factor
SDAM	Scanning droplet adhesion microscopy
FDTS	Perfluorododecyltrichlorosilane
U_{total}	Total potential energy of the magnetic droplet

μ_o	Vacuum permeability
H	Magnetic field strength
M	Magnetization
V	Droplet volume
H_o	Magnetic field strength at the center axis of the magnet
c	Curvature of the magnetic field
x	Distance from the center of the magnetic potential well
F_N	Normal force
β	Viscous damping coefficient
F_μ	Contact angle hysteresis force, measured
μ	Contact angle hysteresis force coefficient
F_S	Substrate force
ω_o	Natural angular frequency
λ	Viscous damping coefficient divided by the mass
ω	Angular frequency of damped harmonic motion
T	Period of oscillation
τ	Time interval within a half-oscillation
$\tilde{F}$	Dimensionless contact angle hysteresis force
$\tilde{B}$	Dimensionless viscous dissipation coefficient
ζ	Damping ratio
c	Damping coefficient
c_c	Critical damping coefficient
Q	Quality factor
E	The energy of a damped harmonic oscillator
E_o	Initial energy of a damped harmonic oscillator
HMDS	Hexamethyldisilazane
RIE	Reactive ion etch
ICP-RIE	Inductively coupled plasma reactive ion etch
RF	Radio frequency
sccm	Standard cubic centimeters per minute
C_4F_8	Octafluorocyclobutane
ASE	Advanced silicon etching
CVD	Chemical vapor deposition
SAMs	Self-assembled monolayers
$-SiCl_3$	Trichlorosilane based group
$-CF_3$	Trifluoromethyl
ODTS	Octadecyltrichlorosilane
FDT	Perfluorodecanethiol

Φ	Volume fraction of the dispersed solid in ferrofluid
κ	Contact line fraction
W_a	Work of adhesion
W_{TPCL}	Work of adhesion along the three-phase contact line length
L_{SL}	Contact line length of solid-liquid interface
L_{LV}	Contact line length of liquid-vapor interface
W_{SL}	Work of adhesion along the solid-liquid contact line length
W_{LV}	Work of adhesion along the liquid-vapor contact line length
κ_s	Solid-liquid contact line fraction
κ_v	Liquid-vapor contact line fraction
PDMS	Polydimethylsiloxane
CIP	Carbonyl iron particles
S_W	Swelling ratio
D	PDMS segment length in a solvent
D_o	Length of the dry PDMS segment
M_B	Bending moment
T_m	Magnetic field torque
E	Elastic modulus, Young modulus
I	Second moment of area
$\delta(z)$	Deflection along the height of the magnetic pillar
V_M	Volume of the magnetic material
M	Magnetization of the pillar
B	External magnetic field
ϑ	Deflection angle of the pillar
α	Angle of the magnetic field
K_ϑ	Angular spring constant
c_o	Correction coefficient
δ	Deflection at the free-end of the micropillar
Trithiol	Trimethylolpropane tris[3-mercaptopropionate]
Diallyl	Trimethylolpropane diallyl ether
Triallyl	1,3,5-triallyl-1,3,5-triazine-2,4,6($1H$,$3H$,$5H$)-trione
SLIPS	Slippery liquid-infused porous surfaces
PVTMS	Polyvinyltrimethoxysilane
F_a	Adhesion force
R_b	Radius of the bubble
ε	Angle between horizontal direction and the tangent of the gas bubble at the contact points between the surface and

	the bubble
ρ_f	Density of the ambient fluid
V_b	Volume of the bubble
GMI	Giant magneto impedance

List of Publications

This thesis consists of an overview and of the following publications which are referred to in the text by their Roman numerals.

I. Al-Azawi, Anas; Latikka, Mika; Jokinen, Ville; Franssila, Sami; Ras, Robin H. A. 2017. Friction and Wetting Transitions of Magnetic Droplets on Micropillared Superhydrophobic Surfaces. *Small*, 13, 38, 1700860. ISSN: 1613-6829. DOI: 10.1002/smll.201700860.

II. Al-Azawi, Anas; Hörenz, Christoph; Tupasela, Topi; Ikkala, Olli; Jokinen, Ville; Franssila, Sami; Ras, Robin. H. A. 2020. Slippery and Magnetically Responsive Micropillared Surfaces for Manipulation of Droplets and Beads. *AIP Advances*, 10, 8, 085021. ISSN: 2158-3226. DOI: 10.1063/5.0012852.

III. Al-Azawi, Anas; Cenev, Zoran; Tupasela, Topi; Peng, Bo; Ikkala, Olli; Zhou, Quan; Jokinen, Ville; Franssila, Sami; Ras, Robin. H. A. 2020. Tunable and Magnetic Thiol–ene Micropillar Arrays. *Macromolecular Rapid Communications*, 41, 2, 1900522. ISSN: 1521-3927. DOI: 10.1002/marc.201900522.

Author's Contribution

Publication I: "Friction and Wetting Transitions of Magnetic Droplets on Micropillared Superhydrophobic Surfaces"

The author planned and executed droplet oscillation experiments. The author fabricated all the samples and analyzed the majority of the experimental results. The author had the main responsibility of writing and editing the manuscript. Ferrofluid synthesis and the experimental set-up adjustments were performed by Mika Latikka.

Publication II: "Slippery and Magnetically Responsive Micropillared Surfaces for Manipulation of Droplets and Beads"

The author developed the fabrication process and produced all the samples used in the experimental work. The author planned and performed actuation as well as directional droplet motion experiments. The author wrote the manuscript and edited the revisions based on the feedback received from the co-authors.

Publication III: "Tunable and Magnetic Thiol–ene Micropillar Arrays"

The author was responsible for planning the work, developing the fabrication process, synthesizing all the samples used in the experimental work and writing the manuscript. The author was responsible for tuning the elastic as well as the surface properties of the magnetic pillars and performed droplet motion experiments. Local actuation experiments by electromagnetic needle and interpretation of the obtained results were performed in collaboration with Zoran Cenev. Colloidal micro- and nanoparticles synthesis was performed by Dr. Bo Peng.

1. Introduction

Superhydrophobicity refers to the remarkable enhanced super water repellency of surfaces. Water droplets roll off easily collecting any contaminants on their path leaving the surface dry. The self-cleaning property otherwise known as the lotus effect; Lotus leaves (*Nelumbo nucifera*) are known for their superhydrophobicity, has intrigued scientists and engineers.[1] The enormous potential of designing and implementing superhydrophobic surfaces to benefit from advantages, only possible when water adhesion to the surface is extremely minimized, like drag reduction,[2–4] anti-biofouling[5–8] and self-cleaning[9] has triggered a spike in research and development during the last decade.

The main challenges facing the advancement of this field are: First, the development of scalable superhydrophobic surfaces that display essential features such as wear resistance, robustness of non-wetting state and if the application requires the ability to respond to an external stimulant. Second, is establishing reliable measurement techniques and protocols to quantify the degree of non-wettability of the fabricated surfaces.

Progress achieved in this field stems from the inspiration of superhydrophobic surfaces found in nature like the lotus leaf and the cicada wings combined with micro- and nanofabrication techniques established as a result of the semiconductor revolution.[9–12] Superhydrophobicity of several functional surfaces that are found in nature is attributed to surface roughness caused by different micro- and nanostructures as well as epicuticular waxes responsible for lowering the surface energy.[13] Wide variety of plant and insect surfaces have been investigated by advanced microscopy,[13,14] which is now an indispensable tool for surface characterization. Advances in micro- and nanotechnology confirmed that there is "*plenty of room at the bottom*",[15] a known title of one of the most significant lectures in physics given by Richard Feynman before the semiconductor revolution and the invention of the scanning probe microscopy.

Planar technology used for integrated circuits (IC) fabrication witnessed a boost in development driven by the requirement of ever shrinking minimum feature lengths. AMD Zen 2 processers used today have a minimum feature length of 7 nm.[16] The miniaturization led to device improvements and reduced cost. Microfabrication techniques including lithography, etch and metallization made technical advances as a result of the semiconductor revolution. These are now established techniques in the development of

myriad of engineering and scientific fields including superhydrophobic surfaces.

1.1   Natural superhydrophobic surfaces

Through evolution, nature adopted solutions that enabled living organisms to thrive in their environment. Confining our attention to functional surfaces involving non-wettability, nature provides us with several examples such as rose petal and cicada wings.

The rose petal and the cicada wings correspond to two different states of non-wettability. A water droplet with a high level of adhesion to the surface is known to be in Wenzel state. In this state, the water interface at the base of the droplet impales the surface microstructure resulting in a pinned droplet.[17] A water droplet deposited on the rose petal is in Wenzel state evident from the co-existence of high contact angle and strong adhesion between water and the solid surface. On the other hand, Cassie state refers to the unpinned state of the droplet. The water interface in this state partially wets surface features meaning that the base of the droplet forms a composite liquid-solid-air interface resulting in a weak adhesion to the surface.[17] Cicada wings are known to sustain water droplets in Cassie state. Cassie and Wenzel wetting states will be defined in detail in the next chapter.

Water droplets deposited on the rose petal do not spread and have almost spherical shape with high contact angle (**Figure 1.1**a). This effect is attributed to the microscopic nature of the surface consisting of dense micropattern as shown in **Figure 1.1**b-d. Rose petals are known for their ability to impede surface wetting and pin water droplets with strong level of adhesion[18,19] (**Figure 1.1**g-h).

Wetting characterization of the rose petal was performed by the tilting plate method and by pushing and retracting a water droplet attached to a needle. Depositing a 5 µL water droplet on the surface of the rose petal followed by tilting the plate from tilt angle $\psi = 0°$ to $\psi = 42°$ did not result in sliding of the droplet as shown in **Figure 1.1**e-f. High adhesion level of the droplet was also confirmed by retracting a 3 µL water droplet from the surface of the rose petal. The droplet stretches and elongates before detachment from the surface in one spot (**Figure 1.1**g). In the other spot, the droplet was detached from the needle and left pinned on the surface during retraction of the needle (**Figure 1.1**h).

High solid-water adhesion of droplets is caused by the impalement of water between the densely packed micropapillae present on the surface.
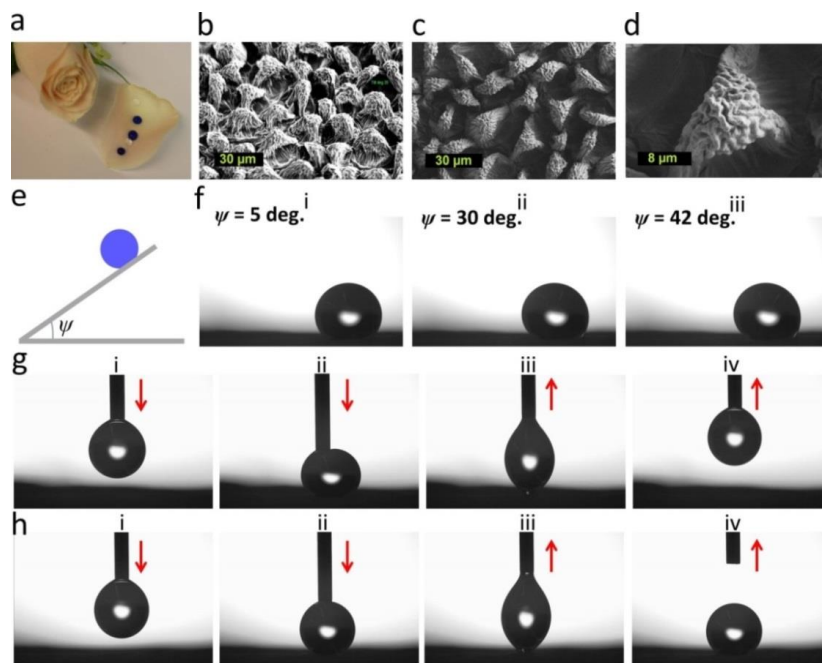
Figure 1.1. Non-wettability of the rose petal. a) Water droplets beading on the surface of the rose petal. The water droplets have high contact angles and do not spread. b) Scanning electron microscopy characterization of dried surface of the rose petal showing the densely packed micropapillae in bird view. c) Top view image of the micropapillae structure. d) Zoom-in image of a single dried micropapilla showing the nanofolds on the surface. e) Sketch of the sliding droplet experiment using tilting plate method. The tilt angle is denoted ψ. f) A series of optical images of a movie recorded during tilting of a 5 µL water droplet deposited on the surface of non-dried rose petal. g, h) Image sequence from a video recording showing pushing and retracting of a 3 µL water droplet attached to a needle moving at velocity of 10 mm/min. The droplet is detached in (g) and pinned in (h) during retraction of the needle. (Al-Azawi et al. Unpublished).

Another example of a superhydrophobic surface found in nature is the cicada wing. Similar to the surface of rose petal, the cicada wings exhibit non-wettability caused by a dense array of nanoscale pillars.[20–22] In contrast to the rose petal, the adhesion level of the water droplets to the surface is low so droplets are easily shed from the surface taking any contaminants with them. This self-cleaning property is also observed on the lotus leaf plant, which surface is decorated with micro bumps with secondary nanoroughness.[23] The superhydrophobicity of the cicada wings shown in **Figure 1.2**a is evident from the high contact angle, the water droplet forms on the wing's surface (**Figure 1.2**b). Nanoroughness was revealed by scanning electron microscopy (SEM) inspection of a surface made of crosslinked thiol-ene polymer that resembles the cicada wing. This thiol-ene surface was produced by double replication process using the actual cicada wing as a template (**Figure 1.2**c).

The low adhesion of water droplets on the superhydrophobic cicada wing was confirmed by the tilting plate method. A 5 µL water droplet was deposited on the surface, which was then gradually tilted until the sliding angle (SA) was reached (**Figure 1.2**d). The droplet starts sliding at $\psi = 13°$ as shown in **Figure 1.2**e. In addition, the low adhesion of water to the surface was

manifested by pushing a 3 μL water droplet attached to a needle moving with a velocity of 10 mm/min. onto the surface followed by retraction in the opposite direction away from the surface (**Figure 1.2**f-g). On two different spots, the droplet remained attached to the needle after retraction without leaving any residues.
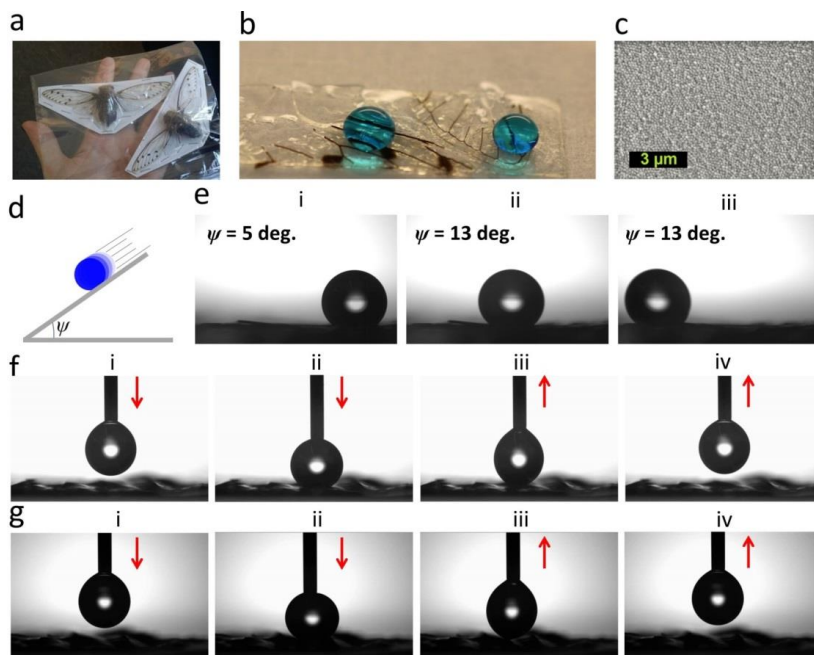

Figure 1.2. Superhydrophobicity of the cicada wings. a) Cicada insects as they were received from the vendor. Image was taken by Dr. Maja Vuckovac. b) Dyed water droplets deposited on the cicada wings. c) Scanning electron micrograph reveals the nanoroughness of thiol-ene surface obtained by double replication from the cicada wing shown in (a). d) Sketch showing the sliding angle of the droplet. e) Image sequence from a video recording of a 5 μL water droplet during tilting of the plate to the sliding angle ψ = 13°. f, g) Optical images of a video recording showing a 3 μL water droplet (i) approaching the surface, (ii) pushing the surface, (iii) before separation from the surface and (iv) during retraction. (Al-Azawi et al. Unpublished).

Cicada wings are known for their bactericidal effect, which is exclusively attributed to the surface nanostructure rather than an effect of surface chemistry.[22,24] Combatting the colonization of bacteria or biomatter on surfaces is important to avoid the undesired change of surface functionalities.[25,26] Biofouling constitutes a major issue in wide range of applications, such as biomedical devices including implants and marine industry.[27]

Mimicking nature provide a promising route to engineer surfaces with enhanced functionalities. Implementing various micro- and nanofabrication techniques, structures made of numerous materials with varying degrees of complexity are patterned with the purpose of attaining specific functionality.[28–30] Superhydrophobic surfaces similar to lotus leaf and cicada wings can provide an alternative way to achieve self-cleaning and anti-biofouling.[6,22,24]

Interesting wetting phenomena are not only observed on cicada wings and rose petals, the spines of the cactus plant achieve directional wettability, which an integral part of the fog collection system of the plant.[31] Water droplets are collected at the spines and directed towards the stem. At the spine, the droplet experiences a net driving force that moves the droplet along it. SEM characterization of the spine reveals microgrooves along the surface with nanoroughness structures within them.[31] The wettability gradient resulting from degree of roughness variation along the spine is responsible for the driving force of the droplet.[31] Cactus like fog collector has been achieved by polymeric microstructures with microgrooves of secondary roughness.[32]

Another intriguing example is the shark skin, which surface is covered with microstructured V-shaped scales called dermal denticles.[2] These structures are responsible for drag and turbulence reduction allowing shark to swim faster and stealthier making it an infamous predator.[2,33] The low drag property has been an inspiration for the design of a professional swimsuit with texture that mimics the shark skin.[33,34]

1.2 Artificial superhydrophobic surfaces

Functional materials possess distinct properties due to geometrical features, chemical composition or combination of both. Superhydrophobicity arise from combination of low surface energy and micro, nano or hierarchical micro/nano surface features arranged in regular or random manner.[17]

Surface energy is the energy associated with intermolecular interactions at the interface between two media. High surface energy means strong molecular attraction whereas low surface energy refers to weak attractive force between interface molecules separating for example water and solid. In order to sufficiently wet/repel water, high/low surface energy is required. This can be achieved by surface activation to obtain high surface energy with hydroxyl termination or low surface energy with fluorine termination.

Micro- and nanostructures are produced by well-established techniques that can be categorized by two fundamental approaches. The first approach, known as bottom-up fabrication, harnesses the tendency of nanoparticles to self-assemble into functional ordered micro/nanostructures that can be rendered superhydrophobic.[35] The second approach is the top-down fabrication. Processes that fall under this technique utilize various lithography, thin film deposition techniques and etching to introduce micro/nanostructure pattern onto the surface (surface micromachining)[36] or into the bulk of the material (bulk micromachining).[37]

Replication using soft lithography is an essential fabrication technique that is used widely for prototyping in combination with surface or bulk micromachining. Soft lithography can be used for efficient pattern replication as shown in **Figure 1.2**c where the nanoscale structure of cicada wing is replicated into polymeric surface.

In this section, examples of artificial superhydrophobic surfaces are given. The first two examples describe surfaces based on silicon fabricated by top-

down approach. One consists of random nanoscale roughness whereas the other consists of regular array of microstructures with secondary nanoscale roughness. The third example presents regular array of thiol-ene micropillars fabricated by double replication using soft lithography. In this example, the micropillars are covered with micro- and nanoparticles by self-assembly.

In the first example, silicon nanograss structure is formed by implementing a top-down fabrication approach involving maskless etch of silicon surface using gas mixture of sulfur hexafluoride (SF_6) and O_2, results are shown in **Figure 1.3**. Random high aspect ratio (AR) silicon nanostructures formed as a result of etch/passivation competition mechanism.[38] SF_6/O_2 plasma produces fluorine radicals (F^*) and oxygen radicals (O^*). F^* radicals are responsible for etching silicon generating etching products such as SiF_x and the volatile gas silicon tetrafluoride (SiF_4). Reaction of etching products with O^* radicals at the surface lead formation of a passivation layer (SiO_xF_y) on cooled silicon substrate. The passivation layer is eroded by ion bombardment exposing silicon to F^*. Anisotropic nanostructures are produced by competition of passivation layer formation by O^* and silicon etching by F^*. Silicon samples subjected to this process appear pitch black (**Figure 1.3**a) because nanostructures (**Figure 1.3**b) generated by this process suppress light reflection and enhance both light scattering and absorption.

To achieve superhydrophobicity, the surface energy was lowered by applying 40 nm thick layer of -$(CF_2)_n$- Teflon®-like polymer by plasma enhanced chemical vapor deposition (PECVD) using precursor gas trifluoromethane (CHF_3). Water droplets pipetted on to the surface roll off easily witnessing the enhanced superhydrophobicity of black silicon (**Figure 1.3**a).
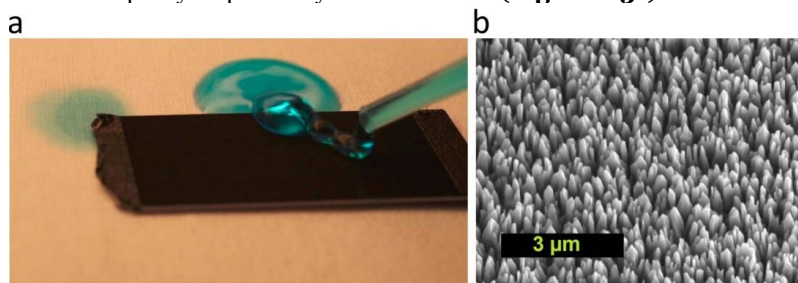
Figure 1.3. Superhydrophobicity of black silicon. a) Shedding of dyed water pipetted on the surface. b) Dense and random high aspect ratio nanostructures of the black silicon sample revealed by scanning electron microscopy. (Al-Azawi et al. Unpublished).

In the second example, a regular array of microstructures is etched into the silicon substrate using etch mask pattern of oxide layer defined by photolithography. In addition, secondary roughness of nanograss structure is etched into the periodic microstructure, which after treatment with Teflon®-like polymer coating by PECVD, rendered the surface superhydrophobic. Water droplets bounce on the superhydrophobic silicon surfaces without leaving any residues of water (**Figure 1.4**a). Array of microstructures with secondary black silicon structures (**Figure 1.4**b) exhibits excellent superhydrophobicity.

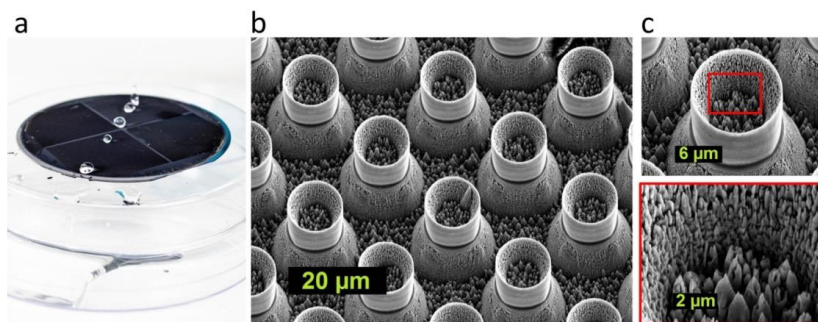**Figure 1.4.** Superhydrophobicity of hierarchical micro- and nanostructured silicon surface coated with thin layer of hydrophobic Teflon®-like polymer. a) Water droplets bounce off the surface without wetting it. The image was taken by Valeria Azovskaya (Aalto University Materials Platform). b) SEM characterization of the periodic array of hierarchical micro and nanostructure responsible for the superhydrophobic effect. c) Zoom-in on a single microstructure. (Al-Azawi et al. Unpublished).

Secondary roughness can also be applied through bottom-up self-assembly approach. Superhydrophobic surface of periodic array of polymeric thiol-ene micropillars with secondary layer of micro- and nanoparticles is shown in **Figure 1.5**. Superhydrophobicity demonstrated in **Figure 1.5**a is due to grafting of hydrophobic self-assembled monolayers onto the surface of micro- and nanoparticles, which are covalently bonded onto the micropillars (**Figure 1.5**b).
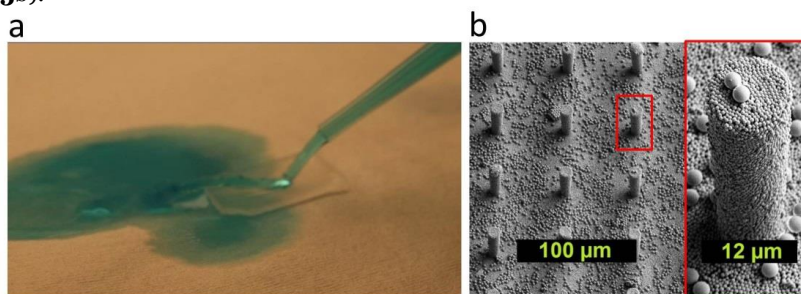
Figure 1.5. Superhydrophobicity of polymeric thiol-ene micropillars. a) Dyed water shedding on superhydrophobic and transparent thiol-ene micropillared sample. b) Periodic thiol-ene micropillar array functionalized with micro- and nanoparticles. (Al-Azawi et al. Unpublished).

Superhydrophobic surfaces have potential practical application ranging from controlled manipulation of droplets and liquids[39] to functional surfaces of advanced properties such as self-cleaning,[9] anti-icing,[40] drag reduction,[2] separation of liquids,[41,42] etc. Establishing a precise measurement technique of superhydrophobic surfaces and developing processes that produce scalable, affordable, robust and tunable superhydrophobic surfaces are the main challenges facing practical application of superhydrophobic surface. This thesis will address these challenges.

1.3 State-of-the-art superhydrophobic surfaces

A brief overview highlighting recent advances in the field of superhydrophobicity is given.

The design of surfaces that can repel water as well as low surface tension liquids such as oil and alcohols has been realized by the fabrication of arrays of mushroom-like microposts with doubly re-entrant nanoscale overhang topology.[43–47] Surfaces with the remarkable ability to repel droplets of polar and nonpolar liquids are known as superomniphobic surfaces. This topic has gained momentum within the field of superhydrophobic surfaces because it can lead to the production of surfaces with robust state of non-wettability and the repellence of wide range of liquids. The re-entrant surface topography makes it possible to achieve superomniphobicity even on materials that are inherently hydrophilic. Dry etching techniques are combined to produce silicon micropillars with nanoscale vertical overhangs capable of repelling droplets of surface tension as low as 22.5 mN/m.[43] Superomniphobic surfaces have also been successfully fabricated by employing two-photon polymerization based 3D printing.[47] This technique allows the fabrication of singly, doubly and triply re-entrant structures. In addition, the fabrication method enables construction of the structures on both rigid and flexible substrates. Repellency of liquids with wide range of surface tension ranging from 72.8 mN/m (water) to 12.0 mN/m (n-perflurooctane) was demonstrated.[47]

Synthesis of superhydrophobic surfaces with a high level of tolerance against abrasion wear is another hot topic within the research of water repellent surfaces. Robust superhydrophobic surfaces are fabricated by replication of high-aspect ratio re-entrant nanostructures from aluminum template via atomic layer deposition assisted sacrificial etching.[37,48] This fabrication method produces hybrid elastomer/metal-oxide superhydrophobic surfaces that are durable. The surfaces remain superhydrophobic even after exposure to harsh chemical and mechanical treatment. Free-form aluminum templates can also be utilized by this process. Fabrication of blood repellent flexible tubes has been demonstrated.[48]

Design of robust superhydrophobic surfaces that simultaneously feature superhydrophobicity and mechanical robustness was also demonstrated in another report.[49] Durable superhydrophobicity was accomplished by structuring surfaces in a way that the highly repellent mechanically fragile nanostructures are housed within pockets of interconnected honeycomb-like microstructure that act as an armor.[49] The nanostructures are prevented from damage by the protecting armor. This strategy can be applied to different types of substrates including transparent glass, silicon, ceramic and metal.

1.4 Outline of the thesis

This thesis addresses fabrication and characterization of superhydrophobic surfaces. Successful application of superhydrophobic surfaces depends on finding materials that can be easily utilized in synthesizing surfaces with key functionalities. Protocols for producing robust and responsive functional superhydrophobic surfaces that ensures minimized droplet adhesion and enables droplet manipulation are reported in this thesis. In addition, the use of oscillating droplet tribometer is reported to demonstrate precise characterization of superhydrophobic surfaces by relating damped harmonic oscillations of magnetic droplets to surface parameters like surface energy and pattern density.

After introducing several examples of natural and artificial superhydrophobic surfaces as a motivation in *Chapter 1*, the outline of the remaining chapters of the thesis is structured as follows:

Chapter 2: The basic concepts of surface wetting including surface tension, contact angle of water droplet, contact angle hysteresis and retention force are introduced. These concepts are important for understanding droplet mobility, wetting states and the transition between them.

Chapter 3: The two techniques utilized for characterization of superhydrophobic surfaces are detailed in this chapter. The first technique is based on measuring the contact angle of a water droplet deposited on the surface by analyzing the drop shape. The second technique is based on measuring the friction of droplets undergoing damped harmonic oscillations on superhydrophobic surfaces.

Chapter 4: Superhydrophobicity of silicon micropillared surfaces is determined by conducting droplet oscillations. As portrayed in **publication I**, friction values extracted from damped harmonic oscillations of droplets are related to the solid-liquid fraction of the micropillared surfaces. This allows precise characterization of superhydrophobic surfaces by relating the measured friction to surface properties. Furthermore, examples of probing friction variation against the type of chemical coating used for lowering the surface energy are presented.

Chapter 5: Responsive superhydrophobic surfaces that are capable for inducing controlled droplet motion are reported in this chapter. In **publication II**, a new fabrication method is introduced to produce arrays of PDMS magnetic micropillars, which after lubricant infusion, applied for controlled droplet motion. Moreover, in **publication III,** arrays of thiol-ene magnetic micropillars decorated with colloidal micro- and nanoparticles of low surface energy are presented.

Chapter 6: Contributions to the field of superhydrophobic surfaces are summarized in this chapter. Translation of the research results into practical applications and the insight the obtained results provides for future research are presented.

2. Fundamentals of Wettability

2.1 Surface Tension

Technological applications and the advancement in understanding intriguing phenomena involving superhydrophobic surfaces make it important to review basic concepts of capillarity and wetting including surface tension and Laplace pressure. Surface effects become dominant when considering liquid interaction at the microscale with natural or artificial microscopic features of different size and shape because of large surface-to-volume ratio.

The contact area and the geometrical shape of a given system consisting of two immiscible fluids in contact are dictated by the minimization of Gibbs free energy (G). The interfacial tension (γ) is defined as Gibbs free energy per surface area (A) for fixed number of molecules n, pressure P and temperature T and it depends on the substances on each side of the interface (**Equation 2.1**).[50]

$$\gamma = \left(\frac{\partial G}{\partial A}\right)_{n,P,T} \tag{2.1}$$

The interfacial tension is known as surface tension when a liquid is in contact with air. A molecule in the bulk is surrounded by other molecules so it can form non-permanent bonds with its neighbors thus gaining a certain amount of binding energy. In comparison, interface molecules lack intermolecular interactions from van der Waals forces and hydrogen bonds because they cannot form as many bonds (**Figure 2.1**). Therefore interface molecules have higher energy and the formation of such interface costs energy. The net effect is an inward force that causes the surface to be under tension and behave as it is covered with a stretched elastic membrane. The energy cost per unit area of a surface separating a liquid and immiscible fluid is expressed by the thermodynamic relation (**Equation 2.1**). The surface tension of water is 72.9 mN/m at 20 °C.[50] This is three times the value of common liquids because of water's strong hydrogen bonds.
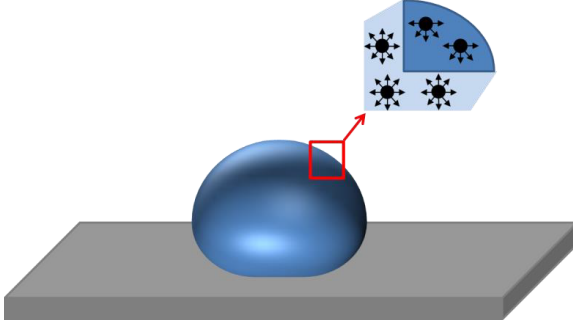
Figure 2.1. Sketch of a droplet in equilibrium deposited on a solid surface. A volume segment illustrates that interface molecules form fewer bonds indicated by arrows compared with bulk molecules.

Surface tension can also be defined as force per unit length (**Equation 2.2**). This is explained by considering a flat rectangular surface of length (L) and width (w). An external force (F_{ext}) acting uniformly on the length causing elongation from L to $L+\Delta L$ without changing the width must supply work $\Delta G = F_{ext}\Delta L$ to create a new surface area $\Delta A = w\Delta L$ containing the energy $\Delta G = \gamma w\Delta L$.[50]

$$\frac{F_{ext}}{w} = \frac{\Delta G}{w\Delta L} = \frac{\gamma w\Delta L}{w\Delta L} = \gamma \tag{2.2}$$

Surface tension depends on the imbalance of intermolecular forces of neighboring bulk phases and is a force per unit length parallel to the interface. Surface tension is responsible for the shape of a liquid droplet on a given surface as it tends to minimize the interfacial surface area, which is equivalent of minimizing the amount of free energy.

A manifestation of non-zero surface tension is a pressure difference known as Laplace pressure across a curved interface in thermodynamic equilibrium.[50] The expression of Laplace pressure (ΔP_{Y-L}) can be derived by considering a small section of an interface separating liquid and gas phases that is subject to expansion through an infinitesimal displacement (δz) as sketched in **Figure 2.2**. The energy associated with increasing the interfacial surface area by infinitesimal (δA) is expressed as ($\delta G = \gamma\delta A$). The total change in Gibbs free energy (δG) with respect to equilibrium configuration must equal zero. Therefore an increase of the surface energy as consequence of increased area is countered by a decrease of the pressure volume energy associated with the volume increase (δV). This means that the total change in Gibbs free energy is expressed as $\delta G = \gamma\delta A - \Delta P_{Y-L}\delta V = 0$. Consequently Young-Laplace equation is deduced as follows

$$\gamma\delta A = \Delta P_{Y-L}\delta V \tag{2.3}$$

The local radii of curvature increase from R_1, R_2 to $R_1+\delta z$, $R_2+\delta z$. The area ($A = \delta x\delta y$) also increases to $A+\delta A = A^* = \delta x^*\delta y^*$. The infinitesimal change in volume is $\delta V = A\delta z$.

The ratio of the arc length (δx) of the area element (A) to the radius of curvature (R_1) is equal to the ratio of the arc length (δx^*) of the expanded area element (A^*) to ($R_1 + \delta z$) because both arc lengths (δx, δx^*) are spanned by the same angle. Thus, the following relation is obtained

$$\frac{\delta x}{R_1} = \frac{\delta x^*}{R_1 + \delta z} \Longrightarrow \delta x^* = \delta x (1 + \frac{\delta z}{R_1}) \tag{2.4}$$

Following the same procedure for the arc lengths (y), (δy^*) and radii of the curvature (R_2), ($R_2 + \delta z$), we arrive to the following expression

$$\delta y^* = \delta y (1 + \frac{\delta z}{R_2}) \tag{2.5}$$

Young-Laplace equation is deduced by substituting **Equation 2.4** and **Equation 2.5** into **Equation 2.3**:

$$\Delta P_{Y-L} = \gamma \left(\frac{1}{R_1} + \frac{1}{R_2} \right) \tag{2.6}$$

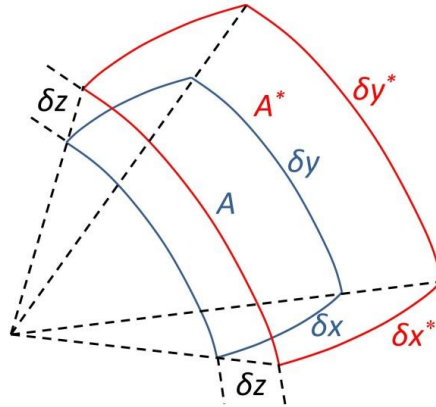**Figure 2.2.** Sketch of surface area element A subjected to an expansion through infinitesimal displacement δz.

The pressure difference across the curved interface commonly known as Laplace pressure is given by the product of surface tension (γ) and the curvature of the interface $\left(\frac{1}{R_1} + \frac{1}{R_2} \right)$ and is highest in the convex medium where the center of curvature is placed.

2.2   Definition of the contact angle and wetting states

The wetting of a solid surface falls into two possible scenarios. First of which is when liquid molecules favor interactions with the surface allowing the liquid to spread. In the second scenario, spreading is impeded because liquid molecules favor mutual interactions over surface interactions. The extent of wetting on a solid surface is controlled by the balance of solid-vapor (air) (γ_{SV}), liquid-vapor (air) (γ) and solid-liquid (γ_{SL}) interfacial tensions. The first entrains the liquid film and the sum of the latter two resist liquid spreading because complete wetting expands the two corresponding surface areas. The wetting scenario is thus determined by the spreading parameter (S_P).[51–53]

$$S_P = \gamma_{SV} - (\gamma_{SL} + \gamma) \qquad (2.7)$$

For $S_P > 0$ complete wetting is achieved and the liquid spreads readily on the substrate in order to minimize the free energy of the wetting system. Equilibrium is reached when a macroscopic thin layer covers the solid substrate. Partial wetting occurs for $S_P < 0$. In this case, the liquid assumes a shape that minimizes the interfacial area, and forms a spherical cap with a contact angle. It is the balance of the surface tensions triad that determines the contact angle, which is defined as the angle between solid-liquid and the tangent of liquid-vapor interface at the contact line where the three immiscible phases intersect.[50] The contact angle is dependent on the topography and chemical composition of the surface. In fact, only on ideal surfaces (atomically flat, isotropic, nonreactive, non-stretched, chemically homogeneous and insoluble) that the contact angle is determined by the balance of surface tensions triad alone. In this case the contact angle is known as the Young contact angle or the equilibrium contact angle on smooth solid surface (θ_{SL})[52,54]

$$\cos \theta_{SL} = \frac{\gamma_{SV} - \gamma_{SL}}{\gamma} \qquad (2.8)$$

The Young equation (**Equation 2.8**) relates the equilibrium contact angle to the triad of the interfacial tensions acting on the contact line. Two-dimensional representation of the force balance at the contact line where the three immiscible phases meet is shown in **Figure 2.3**.
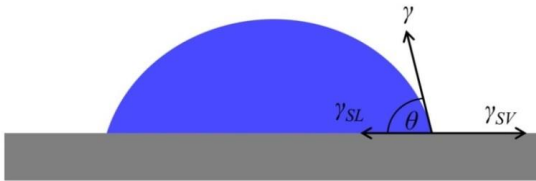

Figure 2.3. Sketch of a droplet in partial wetting showing the equilibrium contact angle the drop makes on the surface by the balance of the three interfacial tensions.

The contact angle is a widely used wetting property because it is a measure of the affinity of the liquid to the underlying surface. Contact angle acquired from measurements on real surfaces is known as the apparent contact angle (θ). If θ < 90°, the material is considered "philic" and if θ > 90°, the material is described to be "phobic" to the wetting liquid. When the wetting liquid is water the material is termed hydrophobic or hydrophilic if θ is larger or less than 90° respectively (**Figure 2.4**).[55,56]
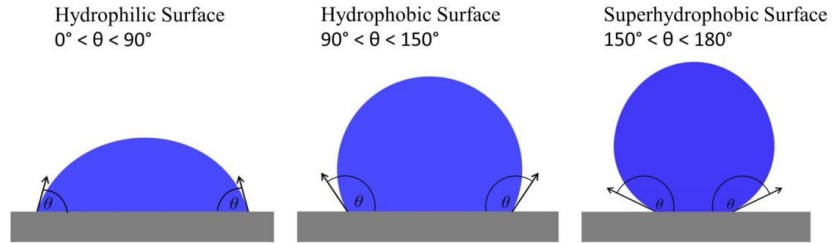

Figure 2.4. A schematic illustrating the range of contact angles that a liquid droplet can form on different solid surfaces according to the degree of wettability.

An alternative approach to deduce the contact angle is by considering the change of free energy of the wetting system resulting from infinitesimal displacement of the contact line of a droplet on the surface in equilibrium. As the contact line advances a distance δx, solid-vapor interface is replaced by solid-liquid interface and liquid-vapor interface is expanded by $\delta x \gamma \cos\theta$ (**Figure 2.5**). Thus the energy change per unit length (L) associated with the displacement of the contact line is expressed as following[53,57–59]

$$\frac{\delta G}{L} = (\gamma_{SL} - \gamma_{SV})\delta x + \gamma \delta x \cos\theta \tag{2.9}$$

At equilibrium $\delta G = 0$ because any variations away from the equilibrium must result in vanishing variation of the free energy. As a result, **Equation 2.9** can be rewritten to the form shown in **Equation 2.8**.[50]
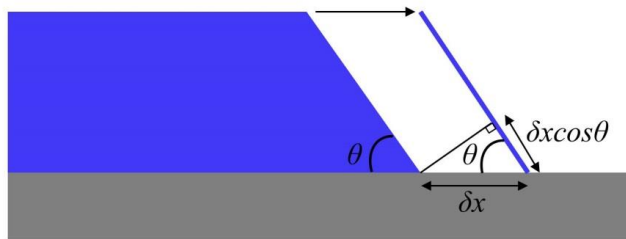

Figure 2.5. Sketch of the contact angle and the displacement of the three-phase contact line an infinitesimal distance δx along a smooth surface.

Real surfaces are never atomically flat and they deviate from ideal surfaces by single or several properties. Real surfaces can inherently exhibit roughness,

which is an important factor affecting the contact angle. Roughness factor is denoted (r) and defined as the ratio of the true surface area to the apparent one and thus it is larger than unity. Roughness can also be result of micro- and nanostructuring. For a surface decorated by random roughness or regular pattern, the free energy of the wetting system is multiplied by factor r hence surface roughness amplifies the hydrophobicity/hydrophilicity of the material because it can store more energy. As mentioned in section 1.1, the wetting state where liquid fully wets surface features and is in full contact with the solid at all points beneath the droplet's base is known as Wenzel state. Accounting for the surface topography, free energy change resulting from an infinitesimal displacement of the three-phase contact line (**Figure 2.6**) is expressed, per unit length of the contact line, as follows

$$\frac{\delta G}{L} = r(\gamma_{SL} - \gamma_{SV})\delta x + \gamma \delta x \cos\theta \qquad (2.10)$$

Re-arranging **Equation 2.10** and using the Young equation (**Equation 2.8**) lead to Wenzel equation (**Equation 2.11**)[17,51,65,53,58−64]

$$\cos\theta_W = r \cos\theta_{SL} \qquad (2.11)$$

According to Wenzel equation, the intrinsic hydrophobicity/hydrophilicity of the material is amplified by the surface roughness. The roughness ensures that the value of Wenzel contact angle reduces ($\theta_W < \theta_{SL} < 90°$) or increases ($\theta_W > \theta_{SL} > 90°$). However, the Wenzel condition (**Equation 2.11**) is only valid for moderate values of the roughness factor and $\cos\theta_{SL}$ because it predicts complete wetting ($\theta_W = 0°$) or complete non-wetting ($\theta_W = 180°$) provided that $r \geq 1/|\cos\theta_{SL}|$ contradicting experimental observations.

Figure 2.6. Sketch of the contact angle and the displacement of the three-phase contact line by an infinitesimal distance δx along a structured surface. The liquid fully wets the surface pattern.

Another possible wetting state on rough/structured surfaces is when the liquid only wets the top asperities and not fully impales the surface pattern, which in this case is surrounded by a thin air layer that is sustained underneath the continuous liquid phase. This wetting state is known as "Cassie-Baxter state", for simplicity, will be called "Cassie state". Given that $\gamma_{SL} > \gamma_{SV}$ for hydrophobic

surfaces, non-wettability is favored because energy is lowered when less solid surface is wetted. Consequently, when the value of roughness factor for hydrophobic surfaces increases beyond a critical value, a water droplet will more likely to be in Cassie state. Expression for the apparent contact angle of a droplet in Cassie state is obtained following the same procedure as Wenzel equation but in this case the contact line displacement occurs on microstructured surface with flat-topped protrusions (**Figure 2.7**). On this heterogeneous surface, the liquid only wets the flat tops. The wetted area in this case is equal to the product of the drop contact area and the solid-liquid contact area fraction (φ_s) – for simplicity will be referred to as the solid-liquid fraction or the solid fraction, which is the ratio of the solid surface area in contact with the liquid to the total contact area

$$\frac{\delta G}{L} = (\gamma_{SL} - \gamma_{SV})\delta x \varphi_s + \gamma(1 - \varphi_s)\delta x + \gamma \delta x \cos\theta \qquad (2.12)$$

Knowing that energy variation is equal to zero at equilibrium and using Young equation, Cassie equation is obtained[17,51,67,53,58,59,62–66]

$$\cos\theta_C = \varphi_s \cos\theta_{SL} + \varphi_s - 1 \qquad (2.13)$$

Alternatively, the Cassie equation can be formulated as

$$\cos\theta_C = \varphi_s \cos\theta_{SL} + \varphi_a \cos\theta_{LV} \qquad (2.14)$$

φ_a is the liquid-vapor contact area fraction and θ_{LV} is liquid-vapor contact angle.
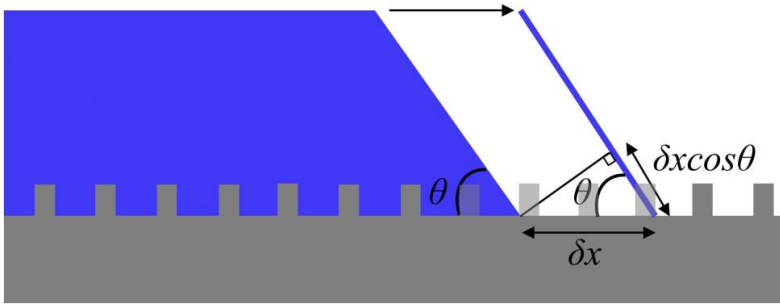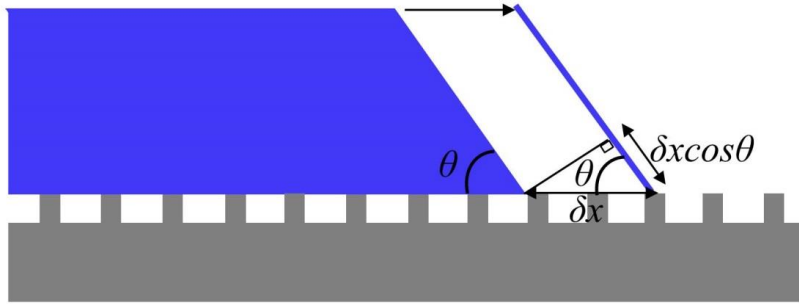

Figure 2.7. Sketch of the contact angle and the displacement of the three-phase contact line by an infinitesimal distance δx along a structured surface. Surface pattern is not impaled by the liquid.

The Cassie equation can also be generalized to any pattern with multiple components of the liquid-material interfaces at the contact line: $\cos\theta_C = \sum \varphi_i \cos\theta_i$. For two-component systems like solid and air, the Cassie equation is given by **Equation 2.13**.

The obstructed area of liquid-vapor interface not necessarily equals the area of solid that is in contact with liquid, the general Cassie equation can therefore

be written as $\cos\theta_c = r_w\varphi_s\cos\theta_{SL} + \varphi_s - 1$,[56,68] where r_w is the roughness ratio of the wet surface area. For a microstructured surface of flat-topped cylindrical pillars where the solid-liquid fraction is equal to the fraction of obstructed area of liquid-vapor interface, we have $r_w = 1$. In the limit of fully wetted surface, the general Cassie equation reduces to Wenzel equation since $r_w = r$ and $\varphi_s = 1$.

The difference between Cassie and Wenzel wetting states is shown in **Figure 2.8**. As shall be apparent throughout this thesis, droplet behavior on a superhydrophobic surface is greatly influenced by the wetting state of the droplet. Section 2.4 of this chapter establishes the theoretical basis for Cassie-to-Wenzel transition while Chapter 4 explores the wetting transition experimentally.
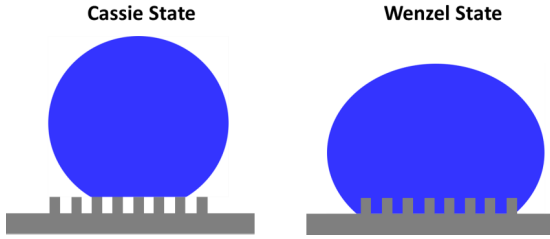

Figure 2.8. Schematic representations of Cassie and Wenzel wetting states on structured superhydrophobic surfaces.

2.3   Superhydrophobicity and contact angle hysteresis

In the previous section we introduced the concept of Young contact angle, which is the contact angle the liquid makes with an ideal surface and defined to be singular and stable. Real surfaces exhibit chemical heterogeneity and defects that locally pin the contact line, which changes accordingly along the roughened surfaces.[69] As a consequence, a small droplet can acquire multiple apparent contact angle values within a range known as contact angle hysteresis (CAH). Each contact angle value within this range corresponds to a local minimum in Gibbs free energy and has to overcome an energy barrier in order to acquire another value.[69,70] The lowest and highest contact angle values within the hysteresis range are the receding contact angle (RCA) and advancing contact angle (ACA), respectively. CAH is a measure of surface stickiness. The higher CAH value is, the higher the force required to immobilize the droplet and is evaluated by changing the droplet volume on a horizontal surface in a controlled manner while monitoring the contact line. ACA is the highest apparent contact angle reached by increasing the droplet volume to the point where the baseline of the droplet starts to advance. RCA is the lowest apparent contact angle obtained by decreasing the droplet volume to the point where the baseline begins to decrease. The difference between ACA and RCA is CAH. Characterization of superhydrophobicity by measuring the advancing and receding contact angles is detailed in the next chapter.

The wetting property of any surface is categorized according to the values of the apparent contact angle and CAH. Non-wettable surfaces exhibit low CAH

(CAH < 10°) and high value of apparent contact angle > 150°, they are known as superhydrophobic surfaces.

Multiple scale hierarchical topography further enhances the non-wettability of surfaces (increased contact angle and reduced CAH) making them more effective of supporting and maintaining Cassie state compared with the equivalent surface with a less degree of hierarchy. Examples of surfaces with multiscale roughness that can support Cassie state are shown in **Figure 1.4** and **Figure 1.5**.

2.4   Cassie-to-Wenzel Transition

It is important to study the changes in free energy between the wetting states in order to verify the important parameters that influence the droplet to be in one of the two wetting states. We will see that the cost of free energy of wetting the surface structures determines the wetting state of the droplet. As we know, the energy of a wetting system can be evaluated by multiplying the interfacial tension by the wetted area (A_{wt}).

In the following we examine a wetting system case consisting of a water droplet on superhydrophobic surface of well-defined square array of cylindrical micropillars with diameter (d), height (h) and spacing (s). The unit cell area of the pattern is illustrated in **Figure 2.9**. The aspect ratio (AR) of the pillars is AR = h/d. The unit cell area (A_c) of the pattern is the pitch squared (p^2); $p^2 = (d+s)^2$.
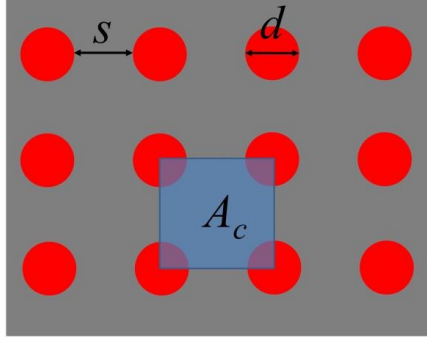
Figure 2.9. Sketch of the mask pattern used to produce square array of cylindrical micropillars. Geometrical parameters of the array are unit cell area (A_c), spacing (s) and diameter (d).

The solid-liquid fraction (φ_s) is defined as the ratio of the wetted area to the footprint area of the drop. In Cassie state only pillar tops are wetted by water which has contact with air elsewhere. The formula of solid-liquid fraction also known as Cassie fraction is

$$\varphi_s = \frac{\pi d^2}{4p^2} \tag{2.15}$$

In this case, the free energy of the wetting system is expressed as follows

$$G_C = \gamma_{SL}\varphi_s A_c + \gamma(1 - \varphi_s)A_c + \gamma_{SV}(r - \varphi_s)A_c \qquad (2.16)$$

The first term of **Equation 2.16** ($\gamma_{SL}\,\varphi_s\,A_c$) corresponds to the contribution to the energy of the wetting system from solid-liquid interface. The second term ($\gamma(1 - \varphi_s)A_c$) is the contribution from liquid-vapor interface and finally the term ($\gamma_{SV}(r - \varphi_s)A_c$) is the contribution from solid-vapor interface.

The free energy of the wetting system in Wenzel state after wetting transition that is when the water fully wets the topography features is expressed as

$$G_W = r\gamma_{SL}A_c \qquad (2.17)$$

The energy changes as the liquid advances between surface features until the point of transition to Wenzel state where the droplet fully impales the structure beneath. The energy difference per unit cell area of the wetting system associated with Cassie-to-Wenzel transition (CW transition) is written as

$$\Delta G_{CW\ transition} = \frac{G_W - G_C}{A_c} = -\gamma[(r - \varphi_s)\cos\theta_{SL} + (1 - \varphi_s)] \qquad (2.18)$$

Cassie state is energetically favorable if for a given surface the transition energy is positive $\Delta G_{CW\ transition} > 0$. Equating $\Delta G_{CW\ transition}$ to 0 in **Equation 2.18** yields a critical contact angle ($\theta_{critical}$) above which the deposited droplet is likely to be in Cassie state. In other words, Cassie regime is favorable when the equilibrium contact angle on a flat surface (θ_{SL}) > $\theta_{critical}$. The relation between the critical contact angle, roughness factor and solid-liquid fraction is expressed in **Equation 2.19**.

$$\cos\theta_{critical} = \frac{\varphi_s - 1}{r - \varphi_s} \qquad (2.19)$$

The formula for $\theta_{critical}$ can also be deduced by equating Wenzel equation (**Equation 2.11**) with Cassie equation (**Equation 2.13**).[59,62,71,72] Transition to thermodynamic equilibrium state from metastable state occurs when $\theta_{SL} < \theta_{critical}$.

It is evident from **Equation 2.19** that $\theta_{critical}$ is defined by the geometry of the surface structure. Superhydrophobic surfaces that are verified to maintain stable Cassie state have $r \gg \varphi_s$ (**Figure 1.2-Figure 1.5**). In this case **Equation 2.19** can be approximated to $\cos\theta_{critical} = -1/r$. For a flat surface of silicon wafer treated hydrophobic layer, the measured value of the apparent contact angle θ_{SL} is 111°, which in this example is assumed to be equal to the equilibrium contact angle. Thus the condition of $\theta_{critical}$ is fulfilled for silicon based superhydrophobic surfaces exhibiting robust Cassie state as demonstrated in **Figure 1.3** and **Figure 1.4** where it is expected that $r > 3$.

The condition for $\theta_{critical}$ (**Equation 2.19**) is computed and plotted in **Figure 2.10** for a surface with square array of cylindrical 10 μm diameter pillars having aspect ratio of 4.5 produced from mask structure shown in

Figure 2.9. In this case the roughness factor can be easily calculated using the following expression

$$r = \frac{P^2 + \pi dh}{P^2} \tag{2.20}$$

Incremental increase of the pitch of the micropillars by 10 μm from 30 μm to 110 μm results in decrease in the values of both r and φ_s.
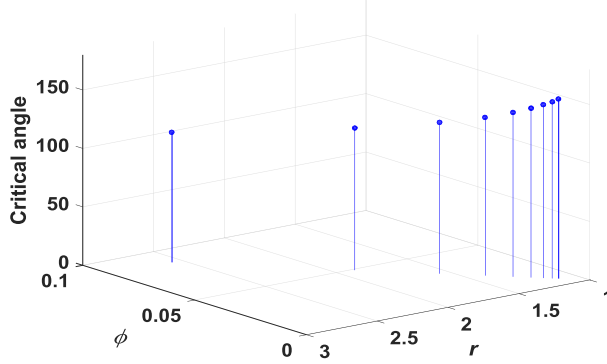

Figure 2.10. The critical contact angle against roughness factor (r) and solid-liquid fraction (φ_s) for square array of cylindrical micropillars. The diameter of the micropillars is 10 μm, the aspect ratio is 4.5 and the pitch is incrementally increased by 10 μm from 30 μm to 110 μm.

The value of critical contact angle shown in **Figure 2.10** increases from 111° to 153° as the value of the pitch increases from 30 μm to 110 μm. Given that for flat hydrophobic surfaces 90°< θ_{SL} < 120°,[58] the condition for a droplet in Cassie state given in **Equation 2.19** is not fulfilled as the pitch value increases indicating that a deposited droplet will be in Wenzel state. This contradicts observations that confirm Cassie state for a droplet deposited on surfaces having similar pattern.[62,73–77] The existing Cassie state in this case is metastable and a droplet occupying this state is prone to collapse to Wenzel state of lower energy.

CW transition of a droplet in a metastable Cassie state is triggered by an external disturbance such as evaporation,[75] vibration[78] or bouncing.[79] The vertical components of surface tension force acting along the perimeter of the pillar structure will oppose the external force caused by the external disturbance acting on a droplet deposited on the micropillared superhydrophobic surface. If the external pressure exerted on the liquid-vapor interface exceeds the maximum sustainable hydraulic pressure known as the critical pressure (P_c), a transition to Wenzel state occurs. Considering superhydrophobic surface with unit cell area (A_c) (**Figure 2.9**) and cross-sectional perimeter of the pillar (S), the balance between the surface tension and the external force is written as follows[80]

$$P_c(1 - \varphi_s)A_c = -\gamma S \cos \theta_A \tag{2.21}$$

Transition to Wenzel state is associated with the motion of the three-phase contact line, which meets the side of the posts with the advancing contact angle θ_A. The total pressure inside the droplet is the sum of contributions from the applied external pressure, the Laplace pressure and the hydrostatic pressure: $P_{total} = P_{ext} + \Delta P_{Y\text{-}L} + \rho g H_d$, H_d is the mean depth of the droplet. CW transition occurs at $P_{total} > P_c$. .

The energy barrier of CW transition can be estimated in terms of P_c, the pressure at which wetting transition is induced and the liquid-air interface moves down to the bottom. The work per unit area of CW transition is expressed as $(1 - \varphi_s)P_c h$, which is equal to transition energy barrier per unit area.

The CW transition is an irreversible process because of the existence of an energy barrier separating the metastable Cassie state of higher energy from Wenzel state. The barrier level that a droplet in Cassie state has to overcome to be in Wenzel state is significantly lower from that associated with Wenzel-to-Cassie transition.[51,81,82]

2.5   Contact angle hysteresis force

The extreme non-wettability of superhydrophobic surfaces benefits several applications where droplet manipulation is essential. Digital microfluidics,[83,84] bioassays[26,85] and icephobic[86,87] surfaces are few examples of critical importance for industrial applications for which droplet retention is detrimental.

As defined in section 2.3 CAH is limited by the lowest metastable contact angle (RCA (θ_R)) and the highest metastable contact angle (ACA (θ_A)). The formula for CAH is

$$\Delta\theta = \theta_A - \theta_R \tag{2.22}$$

CAH is a measure for the resistance to the motion of the three-phase contact line. The force needed to initiate droplet motion is proportional to CAH. In the following an expression for CAH force (F_{CAH}), which is the retention force opposing droplet motion, is derived by considering a water droplet on inclined superhydrophobic surface (**Figure 2.11**a). Due to substrate inclination, the droplet is subjected to a gravitational force $F_g = mg\sin\psi$. The contact area of the droplet is sketched in **Figure 2.11**b is assumed to be circular with contact line length (L_{TCL}). The force acting on infinitesimal segment of the contact line is expressed as $\delta F = -\gamma \delta L_{TCL}\cos\theta - \gamma_{SL}\delta L_{TCL} + \gamma_{SV}\delta L_{TCL}$. The symmetry of the contact line dictates that $\gamma_{SV} = \gamma_{SL}$ along L_{TCL}.   By assuming the contact line meets the solid surface with angle θ_A at the advancing half and θ_R at the trailing half, F_{CAH} is obtained by finding the expressions of the forces acting toward the rear and the front of the drop (**Figure 2.11**).

$$F_R = 2\gamma R \int_0^{\frac{\pi}{2}} \cos\theta_R \cos\varphi \, d\varphi = 2\gamma R \cos\theta_R \tag{2.23}$$

$$F_A = -2\gamma R \int_{\frac{\pi}{2}}^{\pi} \cos\theta_A \cos\varphi \, d\varphi = 2\gamma R \cos\theta_A \qquad (2.24)$$

$$F_{CAH} = F_R - F_A = 2R\gamma(\cos\theta_R - \cos\theta_A) \qquad (2.25)$$

The equilibrium of the droplet at the instant before sliding is written as

$$\sin\psi = \frac{2R\gamma}{\rho Vg}(\cos\theta_R - \cos\theta_A) = \frac{KR\lambda_c^2}{V}(\cos\theta_R - \cos\theta_A) \qquad (2.26)$$

where R is the radius for the patch of the contact area the drop makes on the surface and $\lambda_c = \sqrt{\gamma/\rho g}$ is the capillary length equal to 2.7 mm for a water droplet in air at 20° C.[50,51]

In general, F_{CAH} is presented in a formulation that includes a constant K known as the retentive factor. The value of K depends on the assumption of how the contact angle varies along the contact line. Efforts for deriving F_{CAH} resulted in values between 1 and 3.14. The value of $K = 2$ in **Equation 2.25** originates from the assumption that contact line of the drop meets the surface with two values of the contact angle; θ_A at the front half and θ_R at the rear half.
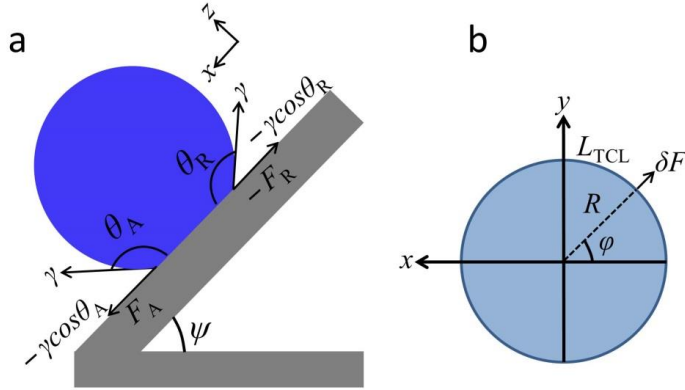
Figure 2.11. Contact angle hysteresis force and sliding angle derivation. a) Sketch illustrating the forces acting on the three-phase contact line of a droplet on an inclined surface. b) The total contact area (footprint area) the droplet makes with surface. The three-phase contact line length, the radius of the footprint area, the azimuthal angle and force acting on infinitesimal segment of the three-phase contact line are indicated.

Another calculation yields $K = 4/\pi$ by assuming that the contact angle over the entire front half of the contact line is θ_A and the value of $\cos\theta$ changes linearly between $\cos\theta_R$ at the rear of the drop to $\cos\theta_A$ at the side of the drop.[88] Additional expression of CAH force is $F_{CAH} = \frac{L_{TCL}}{2}\gamma(\cos\theta_R - \cos\theta_A)$, substituting $L_{TCL} = 2\pi R$ lead to $K = \pi$.[58] Further modification of the CAH force formula in which $K = 48/\pi^3$ was reported to closely resemble the real force induced by the contact line.[89,90] The general formula of CAH force is given as follows

$$F_{CAH} = KR\gamma(\cos\theta_R - \cos\theta_A) \qquad (2.27)$$

In the derivation presented above, the minimum and the maximum contact angles are assumed to be equal to θ_R and θ_A, respectively. For a droplet sliding on inclined surface the measured angles at the receding and advancing edge of the droplet do not necessarily equal to RCA (θ_R) and ACA (θ_A).[91,92] Therefore it is necessary to obtain the measured values of θ_R and θ_A to estimate F_{CAH}.

Controlled droplet motion is important for digital microfluidics.[83,93] Therefore, minimizing F_{CAH} is essential for enhancing the mobility of water droplet. Directional droplet motion on superhydrophobic surfaces can be initiated by designing surfaces with wettability gradients or by implementing a responsive structure that can propel the droplet upon application of an external stimulus. The success of both methods depends on low F_{CAH}. Wettability gradient can be generated by a gradient in solid-liquid fraction. Self-propelled droplet motion towards area of higher solid-liquid fraction is driven by energy minimization of the wetting system.[94-96]

Controlled droplet motion can be achieved by magnetic actuation of superhydrophobic microstructures.[97] This method will be elaborated in Chapter 5.

3. Characterization of Superhydrophobic Surfaces

Progress in research and development of superhydrophobic surfaces require advancement in characterization techniques that can distinguish the non-wettability of different surfaces and provide examination of surface parameters effect on non-wettability. In general, techniques for evaluating wettability are categorized by optical methods or force based methods. The first category includes sessile drop goniometry, which relies on capturing the silhouette of the droplet. Values of contact angle are extracted by optical acquisition of the droplet profile followed by drop shape analysis.[98–100]

Wetting characterization by force based methods relates surface properties that directly influence superhydrophobicity to forces acting upon the droplet.[90,100–107] This thesis introduces the use of oscillating droplet tribometer in successful probing of pattern density and chemical coating variations. Characterization of surface non-wettability was done by measuring dissipative forces of magnetic water droplets experiencing free-decay oscillations on superhydrophobic surfaces of well-defined pattern.

This chapter delves into contact angle goniometry and oscillating droplet tribometer, which are the wetting characterization techniques used in this work. Examples of additional techniques are given below.

Tilting plate method is another approach for evaluating the degree of superhydrophobicity under the category of optical methods. In this technique a droplet of constant volume is deposited onto a horizontal surface followed by gradual tilting of the surface until the sliding of the droplet is initiated at a critical angle known as the sliding angle (SA).[91] The minimum and maximum contact angles at the trailing and leading edges are recorded together with the SA. The droplet is static at inclination angles below SA due to the force balance between the gravitational force and the pinning force caused by CAH (**Figure 1.2**). Low CAH implies low sliding angle as expressed in **Equation 2.26**. As mentioned in the previous section, the maximum contact angle at the leading edge and the minimum contact angle at the trailing edge do not necessarily correspond to ACA and RCA.[91,92] Therefore, except from evaluating the non-wettability of rose petal (**Figure 1.1**) and cicada wing (**Figure 1.2**), this measurement technique was not considered for characterizing the superhydrophobicity of surfaces in this work.

Force based methods for characterizing the superhydrophobicity entails quantifying the strength of interactions between the droplet and the surface. This can be demonstrated by scanning droplet adhesion microscopy (SDAM),

a technique that allows measurement of droplet adhesion forces as small as nanonewton and thus providing visualization of a force wetting map that depicts spatial variation in the wettability.[102,103]

Another force based wetting characterization technique that also relies on measuring the adhesion of a droplet is proposed by using a sessile drop that is stuck to a deflectable capillary. The drop will be dragged across the surface if the adhesion between the drop and capillary is higher than the lateral adhesion between the droplet and the solid surface. The lateral adhesion force is obtained by using Hooke's law when the spring constant and the deflection of the capillary are known.[90,105–107] This technique together with the SDAM is beyond the scope of this thesis.

Results of superhydrophobic surface characterization that are included in this thesis are obtained from the optical method of contact angle goniometry and the force based method of oscillating droplet tribometer. Both techniques are elaborated in this chapter.

3.1   Contact angle goniometry

The most established method for assessing the wetting properties is the sessile drop method. **Figure 3.1** depicts the contact angle goniometry; a drop is deposited on a surface placed on a horizontal stage and the silhouette of the droplet is captured by a camera followed by image analysis that yields the value of the contact angle. Axisymmetric drop shape analysis based on the Laplace equation (**Equation 2.6**) is a reliable fitting tool for determination of contact angle values. The suspended drop is deposited and manipulated by a motorized microliter syringe. The controlled increase or decrease of the droplet volume is enabled by adding or extracting liquid resulting in advancing or receding of the three-phase contact line in a slow rate. This procedure leads to measurement of contact angles of metastable states bound by ACA and RCA.
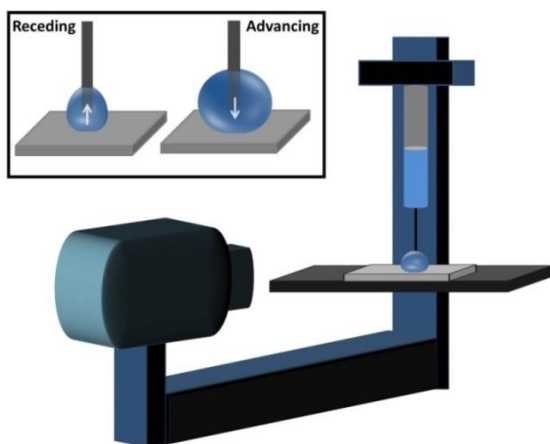

Figure 3.1. A schematic representation of the contact angle goniometer. Inset shows the volume changing method for measuring the advancing and receding contact angles by injection and withdrawal of liquid to and from a droplet.

The limitation of contact angle goniometry is manifested during characterization of superhydrophobic surfaces. In this case, the automatic baseline detection of a droplet having contact angle higher than 150° can fail due to dependence on the image resolution. The baseline indicates intersection points of liquid with the solid surface in the captured side view image of the drop. Blur at the critical segment of the captured image can lead to displacement of the baseline line by the fitting algorithm or by the user. Contact angle measurements on superhydrophobic surfaces are therefore prone to systematic errors from about 1° to beyond 10° as a result of the uncertainty in baseline positioning.[108]

Obtaining accurate assessment of surface wettability via sessile drop goniometry depends on other factors besides the positioning of the baseline. CAH range and droplet size are the main factors contributing to correct interpretation of surface wettability.

Young equation (**Equation 2.8**) introduced in the previous chapter is based on simplifications including atomically smooth unreactive surfaces that are rigid and homogeneous. These assumptions lead to a single Gibbs free energy minimum corresponding to the ideal contact angle,[69] better known as the Young angle, which only depends on surface energies and not on other material properties. In reality surfaces exhibit roughness and heterogeneity that leads to multiplicity of Gibbs energy minima of the wetting system corresponding to multiple metastable equilibrium states.[56,69] Therefore a single apparent contact angle fails to be a quantitative measure of the surface wettability. The range of metastable contact angles depends on interfacial energies of the wetting system and on factors that cause contact line pinning such as roughness and heterogeneity. Correct evaluation of surface wettability entails experimentally measuring the CAH range limited by ACA and RCA.

The number of equilibrium states and the energy barrier level separating them are dependent on the size of the droplet. It has been reported that as the droplet size increases, the number of metastable equilibrium states with smaller energy barrier between them increases.[70,100] Therefore it is important that the size of the droplet is sufficiently large compared with the roughness scale or heterogeneity scale in order for the droplet to be axisymmetric.[68] In general this requirement is met because large droplet (volume > 10 µL) is recommended when RCA is evaluated.[98] This is sufficiently large volume given that the typical scale of roughness is in the order of microns or sub-microns.

Having recognized the important parameters of contact angle measurement, the procedure of wetting characterization is described next. **Figure 3.2** illustrates schematically the measurement of ACA and RCA. A water droplet will attain a contact angle value between ACA and RCA upon its deposition on a planar surface. In the first stage of ACA measurement (**Figure 3.2**a), the drop volume increases at a slow rate during liquid addition while the contact line remains constant. As the volume increases linearly, the contact angle increases and the drop bulges outward about a pinned contact line until ACA is reached. In the second stage, the contact line advances as the liquid continue to be added to the drop. At this point, the width of droplet increases linearly

with time while the contact angle maintains its advancing value as shown in **Figure 3.2**a.

On the other hand, at the first stage of RCA measurement, the liquid is withdrawn from the droplet resulting in a volume decrease. The droplet appears to deflate about a fixed contact line while the contact angle decreases linearly until the RCA value is reached (**Figure 3.2**b). In the second stage, the contact line recedes as the volume decreases linearly. The contact angle is maintained at the RCA value until the drop starts to distort.
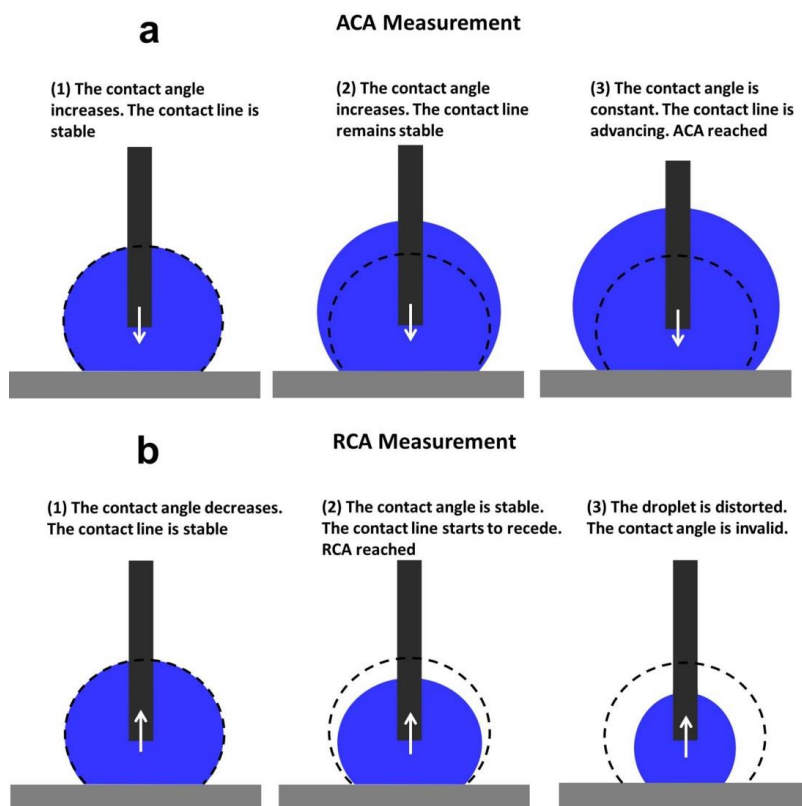
Figure 3.2. A schematic depicting wetting characterization by contact angle goniometry. Measurement procedures for (a) advancing contact angle and (b) receding contact angle.

The variation of contact angle values during ACA and RCA measurements was verified experimentally (Theta Optical Tensiometer, Biolin Scientific, Finland) on two silicon samples that are both treated with hydrophobic perfluorododecyltrichlorosilane (FDTS) self-assembled monolayers. The measurements on a planar silicon sample yield ACA value of 114.7° and the RCA value is 90.8° so the value of CAH is 23.9° (**Figure 3.3**). As expected measurement on silicon surface that is structured with square array of micropillars with circular cross-section (diameter: 10 μm and pitch: 90 μm) yields lower CAH value of 6.9° (**Figure 3.4**).
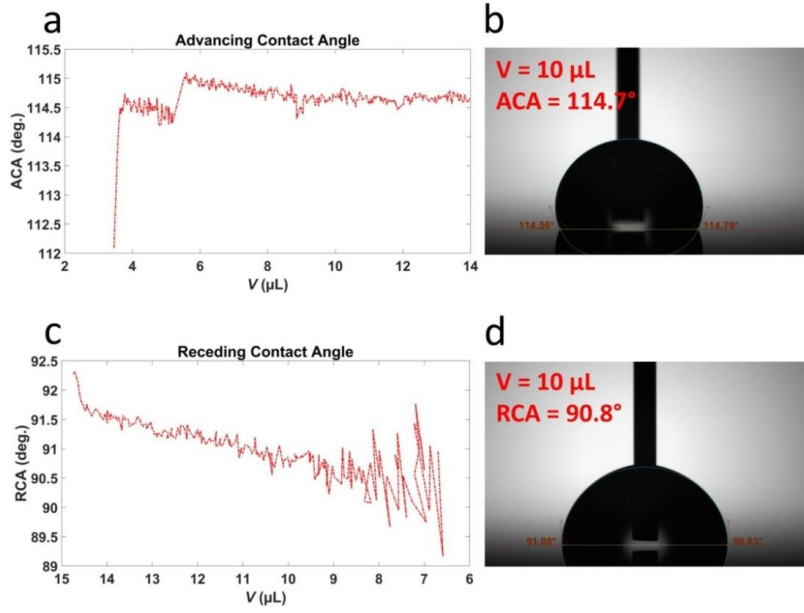
Figure 3.3. Contact angle measurements performed on planar silicon surface treated with perfluorododecyltrichlorosilane. a) Advancing contact angle data. b) Image of 10 µL water drop captured during the advancing contact angle measurement. c) Receding contact angle data. d) Image of the drop captured during the receding contact angle measurement.
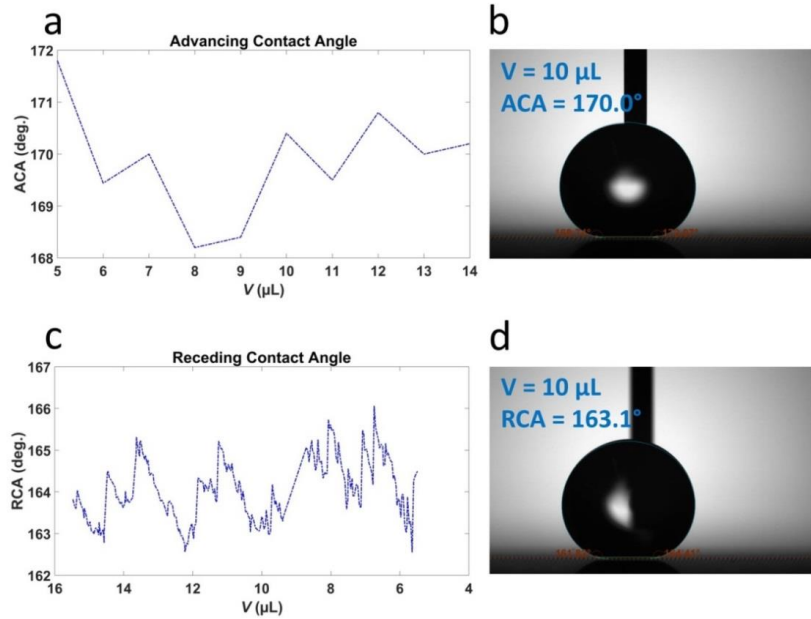
Figure 3.4. Contact angle measurements performed on silicon micropillars (diameter: 10 µm and pitch: 90 µm) treated with perfluorododecyltrichlorosilane. a) Contact angles at discrete volume values during advancing contact angle measurement. b) A 10 µL water drop displaying high contact angle captured during advancing contact angle measurement. c) Receding contact angle data. d) Image of the drop captured during receding contact angle measurement.

The most profound deviation in comparison with the measurement on smooth surface is the behavior of contact angle as function of drop volume during RCA measurement. In contrast to the measurement on the smooth surface where the contact angle monotonically approaches the receding value as the droplet volume shrinks continually. The value of contact angle in Cassie state exhibits periodic oscillation as a result of the stick and slip behavior of the contact line during this stage of RCA measurement on the superhydrophobic surface (**Figure 3.4**c). The stick and slip behavior is a consequence of the discontinuous motion of the contact line during the RCA measurement. During slip the value of contact angle jumps with nearly infinite slope as the contact line gets unpinned from the top faces of the micropillars and pinned onto other micropillars in the inward direction. During pinning contact angle decreases linearly with volume until the point where the contact line gets unpinned again and jumps towards other micropillars.

3.2   Oscillating Droplet tribometer

Limitation of CA measurement on superhydrophobic surfaces has urged researchers to pursue more sensitive techniques based on force measurements. Oscillating droplet tribometer offers a viable alternative for optical methods especially for wetting characterization of surfaces with contact angle > 150°. This technique enables measurement of dissipative forces down to 10 nN.[101]

Characterization of superhydrophobic surfaces using this technique relies on employing water-based ferrofluid droplets, explained in more detail in section 4.3. Measurements are conducted by depositing a ferrofluid droplet on a superhydrophobic surface attached to a horizontal stage. The droplet moves laterally from the initial position on the superhydrophobic surface to an equilibrium position above the permanent magnet fixed below the horizontal stage. The experimental setup is shown in **Figure 3.5** and **Figure 3.6**. The horizontal stage and the permanent magnet are both controlled by two linear precision positioning stages (Aerotech PRO165LM). The motion of the horizontal stage is controlled along the z-direction while the motion of the magnet is controlled horizontally along the x-direction.
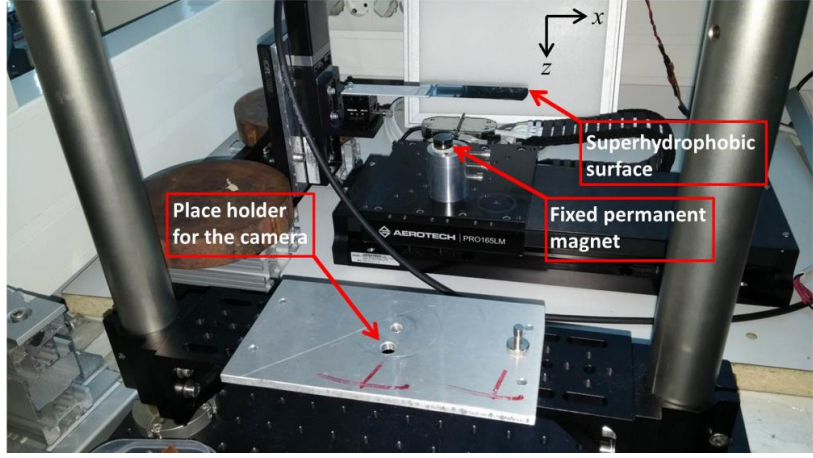
Figure 3.5. The experimental setup of the oscillating droplet tribometer.
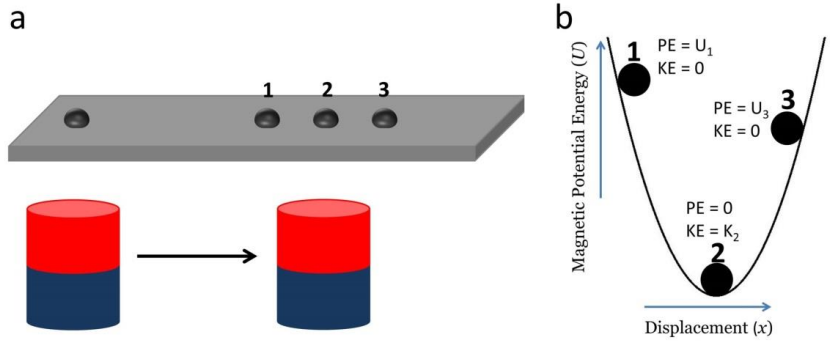
Figure 3.6. Schematics illustrating the procedure of droplet oscillations. a) Translational motion of the permanent magnet to a new position along the *x*-direction generates free decay ferrofluid droplet oscillations around the equilibrium. Three positions (extreme left (1), center (2) and extreme right (3)) during half oscillation cycle are indicated. b) Sketch of harmonic potential well within which droplet oscillation occurs. The total energy (PE+KE) of the droplet oscillates from being completely potential at the extreme points 1 (PE = U_1) and 3 (PE = U_3) to being completely kinetic at the center position 2 (KE = K_2). The total energy of the droplet deceases during the half oscillation cycle as it moves from 1 to 3 due to energy dissipation.

The total potential energy of the droplet above the magnet is $U_{\text{total}} \approx -\mu_0 HMV + mgz$, where ($\mu_0$) is the vacuum permeability, (M) is the magnetization of the droplet, (V) is the droplet volume and (H) is the magnetic field strength, which has the spatial dependency near the symmetry axis $H = H_0 - (cx^2/2)$. (H_0) is the field strength at the symmetry axis ($x = 0$), (c) is the field curvature and (x) is the distance from the center of the magnetic potential well.

The experimental setup makes it possible to control the normal and lateral forces independently. The lateral force, in the x-direction, is a result of a sudden translational movement of the magnet along the x-axis to a new position. Hence a magnetic field gradient is generated and the magnetic potential energy is increased causing droplet displacement. The droplet is then brought into free-decay oscillations by a Hookean restoring force. The

31

transverse motion of the droplet during oscillation is damped by dissipative forces associated with viscous dissipation and contact line pinning. The Hookean restoring force (F_{ext}) can be expressed in terms of the magnetic spring constant (k) as following

$$F_{ext} = -dU_{total}/dx = -\mu_0 Vcx(M+H(dM/dH)) \approx -kx \tag{3.1}$$

The magnetic field induced normal force (F_N) acting on the droplet in the z-direction is sum of gravitational and magnetic force and is written as

$$F_N = -dU_{total}/dz = \mu_0 V(dH/dz)(M+H(dM/dH)) - mg \tag{3.2}$$

The shape of the droplet depends on its proximity with the magnet; it starts to acquire a more flattened shape with higher contact area as the normal force increases leading to an increase in the dissipative forces.

Capturing damped droplet oscillations makes it possible to extract parameters like contact angle hysteresis force and viscous dissipation coefficient which give an indication of pinning and viscous damping, respectively. The dissipative forces are determined by tracking the droplet position with time and fitting the acquired position $x(t)$ with the solution of the general harmonic oscillator as follows

$$m(d^2x/dt^2) = -kx - F_\eta \pm F_\mu \tag{3.3}$$

$F_\eta = 2\beta(dx/dt)$ is the viscous force, (β) is viscous damping coefficient and $F_\mu = \mu mg$ is the CAH force, (μ) is CAH force coefficient. **Equation 3.3** is re-arranged as second-order linear differential equation

$$d^2x/dt^2 + 2(\beta/m)(dx/dt) + (k/m)(x \pm (\mu mg/k)) = 0 \tag{3.4}$$

New variable $y(t)$ is defined as follows

$$y(t) = x(t) \pm (\mu mg/k) \tag{3.5}$$

It is clear from **Equation 3.5** that $d^2y/dt^2 = d^2x/dt^2$. Setting $\beta/m = \lambda$, **Equation 3.4** can be written as follows

$$d^2y/dt^2 + 2\lambda(dy/dt) + (k/m)y = 0 \tag{3.6}$$

The roots of the characteristic equation $R^2 + 2\lambda R + \omega_0^2 = 0$ are $R = -\lambda \pm i\omega$. $\omega = \sqrt{\omega_0^2 - \lambda^2}$ is the angular frequency of the damped harmonic motion and $\omega_0 = \sqrt{k/m}$ is the natural angular frequency of the oscillation. Solution to **Equation 3.6** can be formulated according to the value under the square root. There are three distinct cases, which are the underdamped motion ($\omega_0 > \lambda$), the overdamped motion ($\omega_0 < \lambda$), and the critically damped motion ($\omega_0 = \lambda$). If $\omega_0 > \lambda$, the characteristic roots are imaginary and the general solution for **Equation 3.6** is

$$y(t) = A\,e^{-\lambda t}\cos(\omega t) + B\,e^{-\lambda t}\sin(\omega t) \tag{3.7}$$

A and B are arbitrary constants. This solution can be expressed as following

$$y(t) = C\,e^{-\lambda t}\cos(\omega t - \varphi) \tag{3.8}$$

Using **Equation 3.5** and **Equation 3.8**, the solution for $x(t)$ is given as

$$x(t) = C\,e^{-\lambda t}\cos(\omega t - \varphi) \pm (\mu m g/k) \tag{3.9}$$

If $\omega_0 < \lambda$, the characteristic roots are real. The solution to **Equation 3.6** is

$$y(t) = A\,e^{(-\lambda + \sqrt{\lambda^2 - \omega_0^2})t} + B\,e^{(-\lambda - \sqrt{\lambda^2 - \omega_0^2})t} \tag{3.10}$$

In the case of critically damped motion i.e. when $\omega_0 = \lambda$, the characteristic equation has repeated roots; $-\lambda, -\lambda$. The solution is

$$y(t) = A\,e^{-\lambda t} + Bt\,e^{-\lambda t} \tag{3.11}$$

The overdamped and the critically damped motions do not exhibit oscillations. It is noteworthy that the critically damped motion is known to exhibit the fastest return to the equilibrium position after disturbance.

The ferrofluid droplet confined within the magnetic potential well of the permanent magnet undergoes underdamped oscillations. **Figure 3.7** shows a schematic illustration of the forces acting on the droplet during the oscillatory motion on a superhydrophobic surface. These forces are the Hookean restoring force ($-kx$), dissipative forces ($F_\mu + F_\eta$), the normal force (F_N) and the substrate force (F_S).

The solution to **Equation 3.4** can be expressed in terms of each half-oscillation n as[101,109]

$$x(t) = x(nT/2 + \tau) = x_{n+1}(\tau), \qquad 0 \le \tau \le T/2 \tag{3.12}$$

$$x_{n+1}(\tau) = (-1)^n A_0 \{ \sqrt{1 + \tilde{\beta}^2}\ [(1+\tilde{F})e^{-\tilde{\beta}\pi n} - 2\tilde{F}\sum_{j=0}^{n} e^{-\tilde{\beta}\pi j}\,]\,e^{-\tilde{\beta}\omega\tau}\ \cos(\omega\tau - \cos^{-1}(\frac{1}{\sqrt{1+\tilde{\beta}^2}})) + \tilde{F}\} \tag{3.13}$$

$T = 2\pi/\omega$ is the period of the oscillation, A_0 is the starting amplitude, $\tilde{\beta}$ is the dimensionless viscous dissipation coefficient ($\tilde{\beta} = \beta/m\omega$), $\tilde{F}$ is the dimensionless CAH force ($\tilde{F} = F_\mu/kA_0$), and $n = 0,1,2,...$ is the number of half-oscillations already completed. For example, $n = 2$ represent the state where the droplet has completed a full oscillation cycle and the third half-oscillation is initiated with $\tau = 0$ and $\tau = T/2$ being the initial and final points of the half-oscillation, respectively. The desired parameters $F_\mu = \tilde{F}kA_0$ and $\beta = \tilde{\beta}m\omega$ are extracted by fitting the experimental data with the harmonic oscillator model.
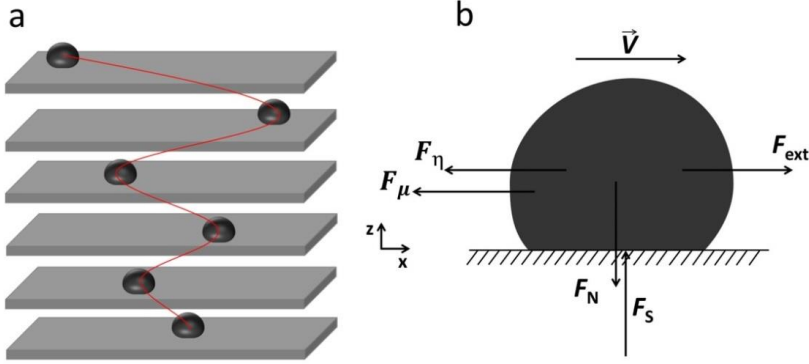
Figure 3.7. Schematic representation of magnetic water droplet oscillation on a superhydrophobic surface. a) Tracking the position of the ferrofluid droplet with time during the oscillatory motion. b) External (F_{ext}), normal (F_N), substrate (F_S) and dissipative forces ($F_\mu + F_\eta$) acting on the ferrofluid droplet in motion.

There are several parameters that can be used to describe the oscillatory motion. The damping ratio (ζ) describes how rapidly the free oscillations decay. In other words it is a measure of the level of damping in a system relative to the critical damping. It is a dimensionless parameter defined as the ratio of the damping coefficient (c) to the critical damping coefficient (c_c). The oscillatory motion after a disturbance can be classified according to the value of the damping ratio; undamped motion ($\zeta = 0$), underdamped motion ($\zeta < 1$), overdamped motion ($\zeta > 1$), and critically damped motion ($\zeta = 1$).

Knowing that $\beta = c/2$ and $c_c = (2\sqrt{km})$, which is derived from the critically damped motion condition ($\omega_o = \lambda$), the damping ratio can be written as

$$\zeta = c/c_c = c/(2\sqrt{km}) = \beta/(\sqrt{km}) \tag{3.14}$$

The quality factor (Q) is another parameter used to determine the qualitative behavior of the damped oscillator. It is defined as the ratio of the energy stored to the energy dissipated in one radian of the oscillation. This is equivalent to 2π times the ratio of the energy stored to the energy lost in a single cycle of oscillation

$$Q = 2\pi \text{ (Energy stored/Energy lost per cycle)} = 2\pi \, (E/{-}\Delta E) \tag{3.15}$$

The energy loss during one cycle of oscillation is $-\Delta E = -\,(\partial E/\partial t)T$. The energy of the oscillator is proportional to the square of the amplitude of the oscillation so the decay of energy is proportional to $e^{-2\tilde{\beta}\omega\tau}$. The decaying energy is given as $E = E_o e^{-2\tilde{\beta}\omega\tau}$, where E_o is the energy value at $\tau = 0$ and $n = 0$.

Using **Equation 3.15**, we find that

$$Q = 1/2\tilde{\beta} = m\omega/2\beta \tag{3.16}$$

For underdamped oscillations with large values of Q and $\omega \cong \omega_0$, the quality factor is approximately the number of radians through which the damped system oscillates as its energy decays to $E = E_0 e^{-1}$.

It can be seen from **Equation 3.14** and **Equation 3.16** that the quality factor can be expressed in terms of the damping ratio

$$Q = 1/(2\zeta) \tag{3.17}$$

Freely decaying oscillations enable quantification of energy dissipation as function of the normal force. Defects and chemical heterogeneities are probed by conducting repeated oscillations with increasing normal force. Thus a relation between dissipative forces and the contact line length or contact area is established. An example of single droplet oscillation measurement is shown in **Figure 3.8**. During this specific measurement the droplet was subjected to a normal force of $F_N = 190 \pm 16$ μN. The parameters obtained from the measurement are: $\mu = 0.0303$, $\beta = 7.8065$ μN/ms^{-1}, $\zeta = 0.0656$ and $Q = 7.622$. Multiple measurements with increasing normal force yield the desired parameters distinct to each measured surface.

Depending on the solid-liquid fraction value of the superhydrophobic surface, increasing the normal force can either result in Cassie-to-Wenzel transition or highly damped oscillation limiting the number of measurements that can be implemented.

The procedure of measurements begins with dispensing a 5 μL ferrofluid droplet on the surface by using a fixed needle at a distance well above the magnet where the normal force is weak. Then the stage with surface attached to it was lowered to a level where the droplet can experience a significant restoring force that can bring the droplet into oscillations. Droplet oscillation was initiated by moving the magnet in the lateral direction by 20 mm at 120 mm/s to displace the droplet from the initial equilibrium position. The oscillations were captured at 1000 fps with the high-speed camera. To avoid the influence of droplet evaporation on the measured results, a maximum of three successive oscillations were captured in a single measurement. The surface was washed with DI-water and dried with N2 flow before depositing a new droplet for a new measurement. For each subsequent measurement the surface was lowered 2 mm towards the magnet to perform experiments with an increased normal force.
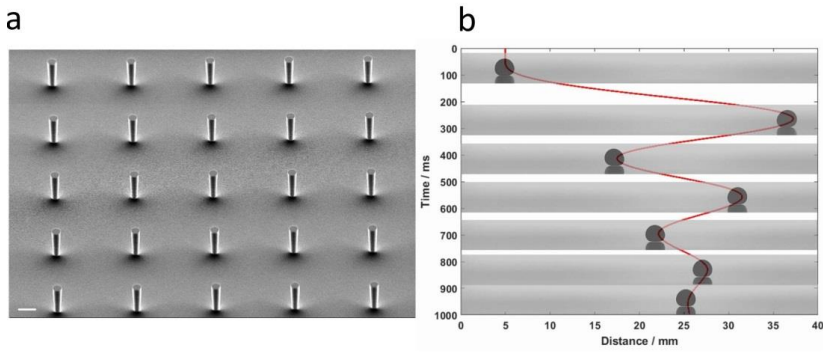
Figure 3.8. Droplet oscillations on a superhydrophobic surface. a) Scanning electron micrograph of the micropillared surface treated with perfluorododecyltrichlorosilane. Diameter of the pillars: 10 µm and pitch: 90 µm. Scale bar 20 µm. b) Oscillatory motion of a magnetic droplet on the micropillared surface shown in (a).

The droplet either undergoes transition to the Wenzel state or the oscillation becomes heavily damped as the normal force increases. This sets a limit to the range above the magnet within which obtaining the desired parameters from the oscillations is feasible. The amplitude of the droplet oscillation decreases as the normal force exerted on the droplet increases as a result of higher magnetic field strength. **Figure 3.9** depicts the variation of the calculated magnetic field strength in the transverse direction within the droplet oscillation region. At moderate values of the normal force, i.e. when the gap between the droplet and the surface of the magnet is 28 mm, the transverse displacement of the droplet during oscillations is confined within a distance no greater than 10 mm on each side of the central axis of the magnet as shown in **Figure 3.8**b. This distance is shortened to approximately 5 mm as the magnetic field induced normal force approaches 260 µN. The magnetic field strength changes only by 4.17 % at a lateral distance of 5 mm from the center axis of the magnet, when the droplet is subjected to a normal force of 355 ± 43 µN (**Figure 3.9**). Therefore, the magnetization of the droplet is assumed to be constant within the oscillation region and the nonlinear term in the magnetic spring constant (**Equation 3.1**) can be neglected.
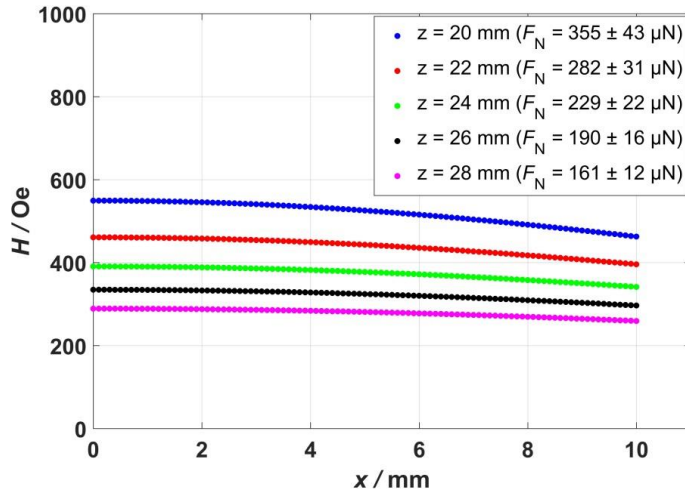
Figure 3.9. Calculated magnetic field strength as a function of the distance (x) from the center axis of the magnet for five different levels above the magnet at which measurements by droplet oscillations are performed. The normal force exerted on the droplet increases within the droplet oscillation region as the distance (z) between the droplet and the surface of the magnet decreases.

Characterization of superhydrophobic surfaces by droplet oscillations will be elaborated in the next chapter.

4. Oscillations and Energy Dissipation of Magnetic Droplets on Micropillared Superhydrophobic Surfaces

Optimization of superhydrophobic surfaces requires reliable and precise characterization of surface non-wettability. Limitations associated with contact angle goniometry in superhydrophobic surface characterization include uncertainty in pinpointing the baseline and difficulty in attaining a symmetric drop shape throughout ACA and RCA measurements due to stronger affinity of the droplet to the needle than the surface. This chapter (Results of which presented in publication I) describes in detail the application of oscillating droplet tribometer as an alternative technique for superhydrophobic surface characterization.

Fundamental parameters affecting the degree of surface non-wettability are topography and surface chemistry. Probing surface parameters is enabled by using free-decay oscillations of magnetic droplets confined in a harmonic magnetic potential well. Dissipative forces that influence energy dissipation such as CAH force and viscous force are extracted by analyzing droplet oscillations. Superhydrophobic surfaces are characterized by monitoring the dependence of energy dissipation to surface parameters.

To validate the sensitivity of the characterization technique, it is important to perform a systematic study of droplet oscillations on superhydrophobic surfaces with well-defined topography. In the study, measurements are repeated on surfaces that are similar in surface structure and subjected to the same chemical modification procedure but differ only in solid-liquid fraction. Thus the effect of solid-liquid fraction on the energy dissipation can be quantified. On the other hand, conducting measurements on surfaces that have similar surface structure but each subjected to a different chemical modification treatment allow quantifying the effect of chemical modification on the energy dissipation.

The influence of the solid-liquid fraction or chemical modification is investigated by using micropillared surfaces of similar pattern geometry and topography but each with unique pitch value or subjected to distinct chemical modification procedure.

For each surface, oscillations are repeated at incrementally decreasing separation between the superhydrophobic surface and the magnet. This way, the robustness of Cassie state of a droplet in motion is evaluated while energy

dissipation parameters are extracted from each captured oscillation. Remarkably, every variation in surface chemistry or pattern density is probed successfully witnessing the high sensitivity of the measurement technique. Moreover, repeated measurements on any sample yield consistent results.

4.1   Fabrication of micropillared surfaces

Micropillared surfaces were fabricated by implementing bulk micromachining process involving photolithography and silicon etch. First, adhesion promoter hexamethyldisilazane (HMDS) was applied to silicon wafers before spin-coating of positive photo-resist AZ5214E at 4000 rpm for 30 sec. Next, the wafers were soft baked on a hot plate for 2 min. at 90°C, followed by UV exposure through glass mask by UV dose equal to 50 mJ/cm^2 using Karl – Süss MA-6 mask aligner. After exposure, the wafers were immersed into the developer solution AZ351B:H$_2$O (1:5) for 1 min. followed by water rinsing and a hard baking on a hot plate for 3 min. at 120°C.

The patterned photo-resist layer was transferred into the underlying silicon substrate by physical-chemical dry etch process known as reactive ion etch (RIE). Anisotropic etching of silicon pillars was accomplished by a variant of RIE called inductively coupled plasma deep reactive ion etch (ICP-DRIE). In this process high density plasma is generated by powerful radio frequency (RF) of 600 W. A mixture of SF$_6$/O$_2$ was used and the flow rates were adjusted at 134 standard cubic centimeters per minute (sccm) for SF$_6$ and 10 sccm for O$_2$. Collisions of electrons with gas molecules produces etchant species, which are fluorine atoms (F), excited atoms (F*), molecular fragments (SF$_x^*$) and ions (F$^+$, SF$_x^+$). O$_2$ is added to the chamber to prevent SF$_x^*$ from recombining to SF$_6$, thus increasing the concentration of F*. The wafer electrode is biased by another RF source at 10 W. Reactive ions are accelerated to the surface of the wafer by the self-bias that develops between the surface and the plasma. Fluorine reacts with silicon to produce volatile etch product (SiF$_4$). This reaction result in isotropic etching of silicon. Alternating etching by ion bombardment and passivation by deposition of octafluorocyclobutane (C$_4$F$_8$) inhibitor is the preferred DRIE technique for etching of high aspect ratio (AR) structures. This etch technique is called Bosch process, where good anisotropy is achieved by balancing the inhibitor deposition and removal. Silicon etch was carried out in advanced silicon etching (ASE), Surface Technology Systems LTD (STS). The duration of the total etch cycle is 20 sec. (etching: 13 sec. and passivating: 7 sec.) and the etch rate is 2 µm/min. Etch proceeds in vertical direction facilitated by removal of the passivation layer from the bottom by impinging ions from SF$_6$ in the plasma. The passivation layer lingers on the sidewalls protecting it from the reactive species. During passivation step, the protecting layer is recovered at the bottom by C$_4$F$_8$ in the plasma before rapid removal by subsequent etch step. After complete etch, the resist layer, which is the etch mask was stripped by sonication in acetone for 15 min. followed by ultrasonic cleaning in isopropanol for 3 min. and cleaning in water for 5 min. Finally the remaining resist residues were removed by Piranha solution H$_2$SO$_4$:

H₂O₂ (5:1) for 12 min. at 110°C. The Piranha treatment is important not only for removing the resist residues but also it provides a surface with hydroxyl terminated groups, which is essential for the reaction of low surface energy monolayers. This will be illustrated in the next section.

Figure 4.1 shows SEM inspection of the micropillared surface produced by the fabrication process. The processed wafer contains multiple fields each with a unique spacing value between the pillars. Droplet oscillation experiments were performed on five different fields of 10 μm diameter pillars. The pitch values of the different fields are 50 μm, 60 μm, 70 μm, 80 μm and 90 μm corresponding to solid-liquid fraction (φ_s) values of 3.14 %, 2.18 %, 1.60 %, 1.23 % and 0.97 %. The solid-liquid fraction values are calculated from **Equation 2.15** multiplied by 100, which refer to the percentage of area fraction wetted by the drop in Cassie state.

a

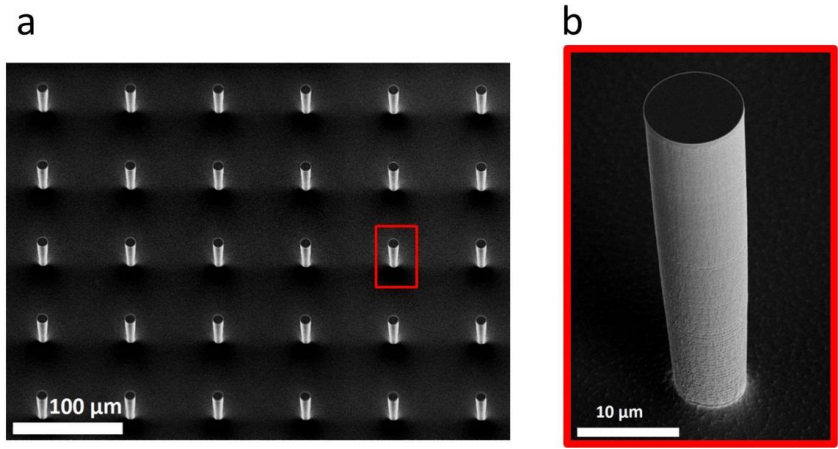b

Figure 4.1. Scanning electron micrograph of the micropillared surface manufactured by the Bosch process. a) Array of 10 μm diameter pillars. Solid fraction of the surface is 1.23%. b) Zoom-in micrograph of a single silicon pillar.

Superhydrophobicity was characterized by measuring RCA and ACA of the micropillared surfaces. The results of the characterization are listed in **Table 1.**

Table 1. Advancing contact angles, receding contact angles and contact angle hysteresis of water droplets measured on micropillared superhydrophobic surfaces of varying solid fraction. The values represent an average of three measurements repeated at different spots on the substrates. Reproduced with permission from publication I. Copyright @ 2017 John Wiley & Sons, Inc.

Solid-liquid fraction φ_s	ACA (º)	RCA (º)	CAH (º)
3.14 %	170.3 ± 0.8	156.8 ± 1.7	13.5 ± 1.9
2.18 %	171.4 ± 1.0	157.2 ± 1.3	14.2 ± 1.6
1.60 %	170.2 ± 0.8	160.0 ± 0.6	10.2 ± 1.0
1.23 %	170.5 ± 0.3	160.6 ± 2.0	9.9 ± 2.0
0.97 %	171.5 ± 1.8	164.3 ± 1.3	7.2 ± 2.2

It can be concluded from **Table 1** that CAH decreases with the solid fraction. However, contact angle goniometry measurement yields higher CAH value for a surface of φ_s = 2.18 % compared with surface of φ_s = 3.14 %. Moreover, comparable CAH values obtained from surfaces of φ_s = 1.60 % and φ_s = 1.23 %. The accuracy of the contact angle goniometry cannot be captured by the reported standard deviations in **Table 1**. The contact angles are so high that a baseline shift up or down by one pixel result in a change of up to 5º.[108]

   Force based techniques offer orders of magnitude better sensitivity in superhydrophobic surface characterization. As we will see in this chapter, droplet oscillation method enables measurement of a CAH force as low as 1.83 ± 0.089 µN on the micropillared superhydrophobic surfaces. In addition, the method can easily probe variation in solid-liquid fraction or applied chemical coating across multiple samples. These advantages allow distinction between superhydrophobic surfaces with seemingly comparable values of CAH.

4.2   Surface modification

Chemical vapor deposition (CVD) refers to the thin film formation from reactions that take place at the surface. An example of CVD is surface modification with low-energy self-assembled monolayers (SAMs). Covalent bonding between head groups of SAMs and surface groups results in molecularly thin film layer. CVD was used to treat the fabricated micropillared surfaces to impart superhydrophobicity to the structure. This was achieved by application of two different variations of CVD processes, which are vapor-phase SAMs deposition and plasma enhanced CVD (PECVD). In addition, solution-phase SAMs deposition was also implemented.

   Prior to vapor-phase deposition of 1H,1H,2H,2H-Perfluorododecyltrichlorosilane (FDTS) ($CF_3(CF_2)_9CH_2CH_2SiCl_3$) at atmospheric pressure, piranha treatment was conducted to obtain hydroxylated Si/SiO_2. FDTS molecule consists of trichlorosilane based head group (-$SiCl_3$), spacer chain –$(CF_2)_9(CH_2)_2$– and trifluoromethyl (-CF_3)

terminal group. The trichlorosilane based head groups react with the hydroxyl groups on the surface releasing hydrogen chloride. This process step generates rigid and stable thin film layer because FDTS is able to form monolayers that are strongly linked by Si–O–Si bonds [110–114] as shown in **Figure 4.2**.
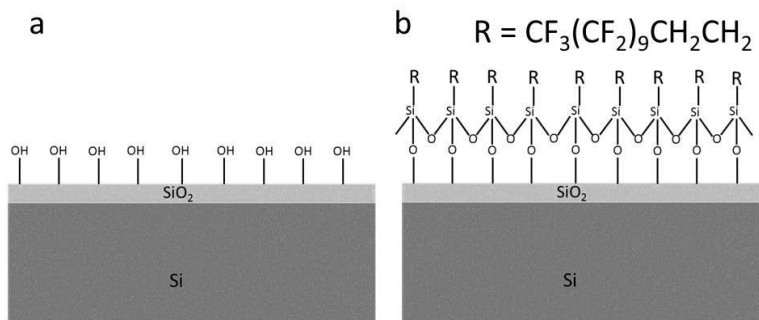

Figure 4.2. Sketch depicting the process of self-assembly and covalent bonding of hydrophobic monolayers. a) Hydroxylated silicon surface after Piranha treatment. b) Reaction of perfluorododecyltrichlorosilane with the hydroxyl groups.

After sample preparation step, which involved Piranha treatment followed by water rinsing and drying under stream of N_2, the micropillared silicon surface was placed inside a glass Petri dish that was closed with a lid. Solid granulates of FDTS with melting point of 50-55°C are located in the vicinity of the sample inside the Petri dish, which was placed on a hot plate maintained at 85°C. The vapors of melting granulates diffuse to the surface where the reaction occurs forming the molecular layer.

SEM characterization of the micropillared structure after surface modification with FDTS is shown in **Figure 4.1**.

Alternatively, micropillared surfaces can be rendered superhydrophobic by methyl-terminated silane SAMs using solution-phase approach. In this case octadecyltrichlorosilane (ODTS), which has trichlorosilane based head group similar to FDTS, $-(CH_2)_{17}-$ spacer chain and methyl terminal group was used for surface modification. 10 mM solution of ODTS was prepared by dispensing 100 μL of ODTS to 25 mL of toluene in N_2 environment inside a glovebox. The micropillared samples were immersed in the solution after the Piranha treatment. After a treatment time of 1-4h, the samples were cleaned in fresh toluene followed by cleaning in acetone and then in isopropanol.

The solution-phase approach was also applied for the surface modification of polymeric thiol-ene micropillars decorated with colloidal micro- and nanoparticles (**Figure 1.5**). As illustrated in publication III, superhydrophobicity is induced by grafting of 1*H*,1*H*,2*H*,2*H*-Perfluorodecanethiol (FDT) ($CF_3(CF_2)_7CH_2CH_2SH$) SAMs onto the surface by photo "click" thiol-ene reaction. The polymeric samples were immersed in 5 vol. % solution of FDT, in ethanol (250 μL FDT in 5 mL ethanol).

The third approach for surface modification is the deposition of Teflon®-like thin film layer $(CF_2)_n$. Plasma enhanced CVD (PECVD) using Trifluoromethane (CHF_3) source gas was used to deposit the thin film polymer layer. This process, which is referred to as polymer growth, is similar to the

application of the passivation layer in the Bosch process. PECVD deposition was carried out in Plasmalab 80+, Oxford Instruments.

Deposition parameters are: Flow rate of CHF_3= 100 sccm, power to platen = 50 W, set pressure = 30 mTorr and deposition time = 5 min. Deposition rate ≈ 6 nm/min.

4.3 Energy dissipation of magnetic droplets on micropillared superhydrophobic surfaces

In this section a systematic study aims at measuring the dissipative forces is presented. The main advantages of droplet oscillation technique for precise probing of factors affecting the degree of surface superhydrophobicity are:

1) Variation in dissipative forces directly reflects inhomogeneity or existing variation of a giving surface property across a series of measured surfaces.

2) Offers capability to independently control lateral and normal forces acting on the dynamic droplet.

In publication I, investigation of dynamic superhydrophobicity was done by performing droplet oscillations on micropillared surfaces of different values of solid-liquid fraction (φ_s). Water based ferrofluid was produced by synthesizing superparamagnetic iron oxide nanoparticles in water using coprecipitation method. The nanoparticles were stabilized with citric acid near pH 7.[115,116] Next, the ferrofluid was diluted with Milli-Q water to concentrations of 0.2 vol. % (dilute ferrofluid) and 4 vol. % (concentrated ferrofluid). The density and viscosity of the aqueous ferrofluid increase as the volume percentage of the magnetic particles increases. For the 4 vol. % ferrofluid, the density is 1.157 g/cm3. The saturation volume magnetization for the 4 vol. % ferrofluid is 14 kA/m and increases linearly with the density. The measured surface tension for the 4 vol. % is 69.9 ± 1.4 mN/m. The viscosity can be predicted by Einstein model according to which the increase in viscosity is $5\Phi/2$, where Φ is the volume fraction of the dispersed solid.[117] In addition, the alignment of the magnetic particles in an external magnetic field contributes to an additional increase of viscosity corresponding to $3\Phi/2$ at maximum according to Hall-Busenberg model.[118] Thus the estimated viscosity for the 4 vol. % ferrofluid is 16 % higher than that of pure water. On the other hand, the measured physical parameters for the 0.2 vol. % ferrofluid deviate no more than 0.7 % for density and 4 % for viscosity when compared to pure water.[101] The measured value of surface tension is 72.6 ± 0.3 mN/m.[101] Judging from the mentioned parameters, the ferrofluid used in this work was diluted to such extent so its physical properties do not deviate significantly from water so the measured energy dissipation reflects that of pure water.

For each surface multiple oscillations were performed with increasing contact line length enabled by adjusting the normal force so the energy dissipation of the dynamic droplet under well-defined forces is measured. This way, the range of measurements for a surface of a given geometrical parameters is determined. Giving that the droplet is in Cassie state and the dissipation forces are not too large compared with the magnetic restoring force,

quantitative values for CAH and viscous dissipation forces are obtained from the damping rate of freely decaying oscillations. These conditions are fulfilled for the oscillation shown in **Figure 4.3**a. Initiating droplet motion at large normal force can either induce CW transition (**Figure 4.3**b) or result in oscillations that are too strongly damped for analysis.
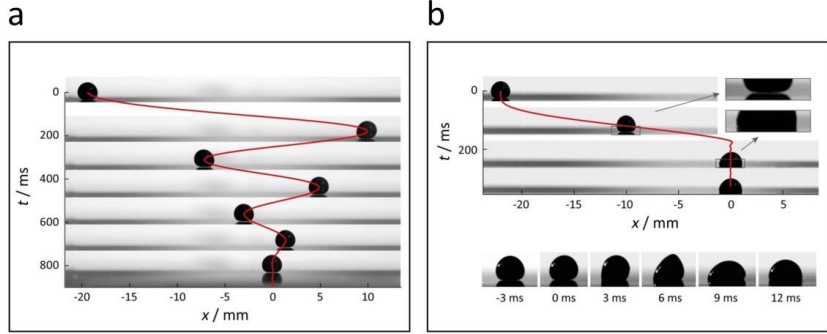
a

b

Figure 4.3. Droplet oscillation and wetting transition of a magnetic droplet on micropillared surface with φ_s = 1.23 %. a) Tracking droplet position with time of the transverse oscillation. The normal force is F_N = 210 ± 20 µN. b) Cassie-to-Wenzel transition of the dynamic droplet in motion subjected to a normal force of F_N = 430 ± 60 µN. Lower inset shows the time interval of the wetting transition. Reproduced with permission from publication I. Copyright @ 2017 John Wiley & Sons, Inc.

The influence of φ_s on the rate at which oscillation decay due to total energy (sum of magnetic potential and kinetic energies) dissipation is shown in **Figure 4.4**.

a

b
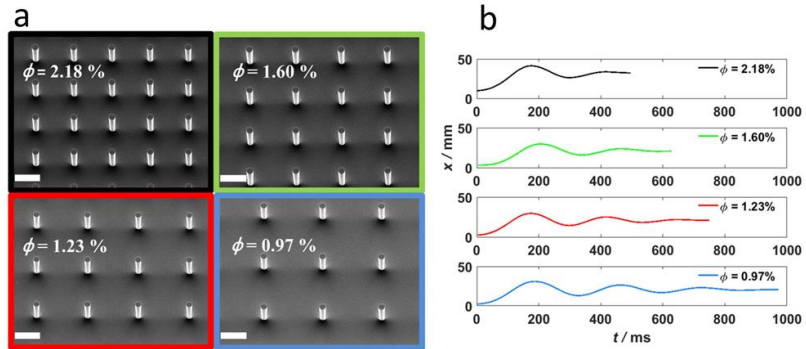
Figure 4.4. a) Scanning electron microscopy images of silicon micropillared superhydrophobic surfaces each with distinct value of solid fraction. b) Profiles of magnetic droplet free-decay oscillation performed on the four surfaces shown in (a). The magnetic droplets are subjected to an equal normal force to reveal the dependency of solid fraction on the damping rate of the oscillation. Reproduced with permission from publication I. Copyright @ 2017 John Wiley & Sons, Inc.

Energy dissipation, which is balanced between CAH force and viscous dissipation, is higher for surfaces with increasing pillar density. The rate at which these oscillation decay determines the dissipative forces by fitting droplet position with time $x(t)$ with the solution of the general harmonic oscillator (**Equation 3.3**).

Characterization of superhydrophobic surfaces by free-decay oscillation involves repeating the oscillations with increased normal force on each surface shown in **Figure 4.4**a. Results of surface characterization using both dilute and concentrated ferrofluids are presented in publication I.

CAH force (F_μ) and viscous dissipation coefficient (β) are extracted from droplet oscillations and plotted against the droplet contact line length and contact area, respectively (**Figure 4.5**). The values of the contact line length and contact area are calculated from the Young-Laplace equation. The calculated values used in **Figure 4.5** are multiplied by φ_s because it is assumed that the droplet is only in contact with the pillar tops during oscillations. The contact line length and contact area increase with the normal force causing a monotonic increase in the measured CAH force and viscous dissipation as shown in **Figure 4.5**.

Measurements on surfaces of 10 μm diameter pillars with solid-liquid fraction values beyond the range 0.78 % < φ_s < 3.14 % are not feasible using the setup presented in **Figure 3.5**. Oscillations performed on micropillared surface with φ_s = 3.14 % are strongly damped for analysis and therefore disregarded. On the other hand, drop undergoes CW transition on a surface with φ_s = 0.78 %.
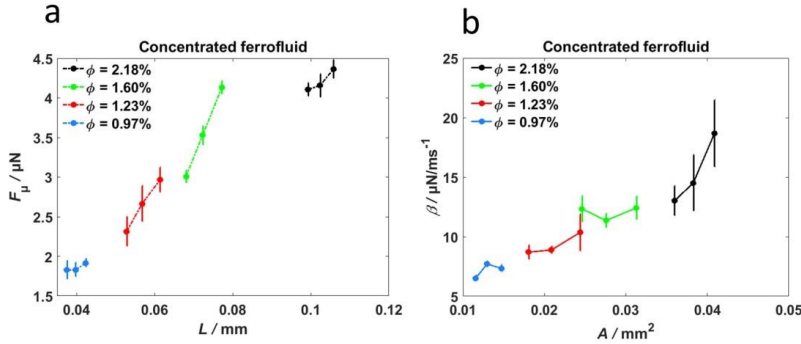
Figure 4.5. Dissipative forces obtained from measurements conducted on micropillared superhydrophobic surfaces each with distinct value of solid-liquid fraction. The surfaces are treated with perfluorododecyltrichlorosilane (FDTS). a) CAH force (F_μ) as function of the contact line length (L). b) Viscous dissipation coefficient (β) as function of the drop contact area (A). Reproduced with permission from publication I. Copyright @ 2017 John Wiley & Sons, Inc.

It is evident from **Figure 4.5** that viscous dissipation increases with increased contact area and φ_s. The droplet is experiencing slip-rolling motion during oscillation across the micropillared superhydrophobic surfaces. Pure rolling motion state is not achieved at any point during the oscillation. However, droplet rotation was noticed at the end of each half-oscillation before the direction of motion is reversed.[101] The influence of the contact area extends into a droplet in pure rolling motion to fill a volume ($V \sim R^3$), near the contact area of radius R, known as Hertz volume.[119] Since the ferrofluid droplet does not reach steady-state rolling motion, we assume that viscous dissipation does not spread far from the contact area to fill the Hertz volume and thereby becomes proportional to the contact area. Hence, the increase of viscous

46

dissipation is dominated by the effect of contact area increase rather than droplet height decrease as the normal force increases. In addition, it has been shown through numerical simulation that the center-of-mass velocity of a droplet in slip-rolling motion state increases steadily with the droplet size.[120] The velocity value plateaus as the size of the droplet approaches the capillary length.[120] At this stage, the droplet deviates from the spherical shape and becomes more flattened. A ferrofluid droplet becomes more flattened as the normal force increases. Therefore it can be assumed that the effect of droplet size on the center-of-mass velocity becomes negligible as the normal force increases even if the size of the droplet is less than the capillary length.

The influence of solid-liquid fraction on the droplet oscillation can also be captured by the damping ratio (ζ) and the quality factor (Q) as depicted in **Figure 4.6**. Droplet oscillations subjected to a normal force $F_N = 229 \pm 22$ μN exhibit higher damping ratio and lower quality factor as solid-liquid fraction increases.
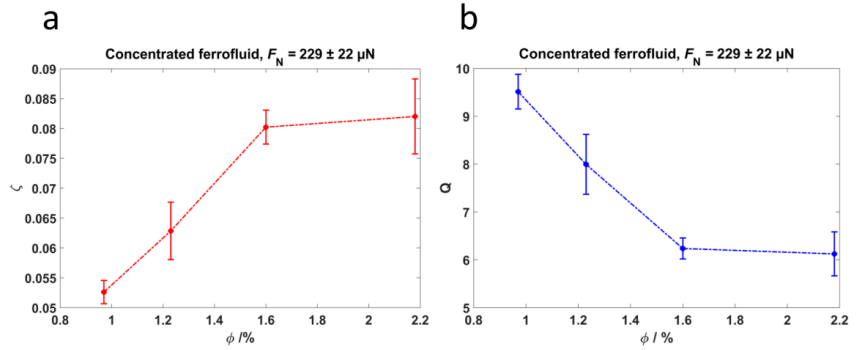
Figure 4.6. Damping ratio (ζ) and quality factor (Q) extracted from oscillations subjected to a constant normal force. The measurements are conducted on four micropillared surfaces each with distinct value of the solid-liquid fraction. a) Damping ratio vs. solid-liquid fraction. b) Quality factor vs. solid-liquid fraction.

The obtained results shown in **Figure 4.5** indicate the success of force based measurements in eliminating the uncertainty of non-wettability characterization because each surface yields unique values of dissipative forces.

The values of the measured CAH force (F_μ) are compared in **Table 2** with the calculated CAH force (F_{CAH}) values obtained from **Equation 2.27** using $K = 48/\pi^3$, contact angle values listed in **Table 1** and $R = L_{TCL}/2\pi$, where L_{TCL} is the calculated contact line length at 24 mm above the magnet.

Table 2. Comparison of the calculated values of contact angle hystereis force (F_{CAH}) with the measured values of contact angle hysteresis force (F_μ). The measured values are extracted from droplet oscillations at 24 mm above the magnet. The oscillations conducted on different micropillared superhydrophobic surfaces each with distinct value of solid-liquid fraction.

Solid-liquid fraction φ_s	F_{CAH} [µN]	F_μ [µN]
2.18 %	5.43	4.10
1.60 %	3.71	3.52
1.23 %	3.31	2.31
0.97 %	2.06	1.91

The versatility of the oscillation method was also used to quantify the influence of chemical modification on the dissipative forces. Droplet oscillation measurements were conducted on three micropillared surfaces, all share the same value of solid-liquid fraction φ_s = 1.23 %. The first was subjected to fluoropolymer deposition by PECVD. The second was treated with ODTS by solution-phase process, whereas the third was treated with FDTS by vapor-phase process. Results of the characterization, which are presented in **Figure 4.7**, show that surfaces treated with SAMs exhibit lower F_μ compared with the values obtained from the surface coated with Teflon®-like fluoropolymer by PECVD. Moreover, droplet oscillation method allows probing the difference between surface treatment with FDTS by vapor-phase CVD and treatment with ODTS by solution-phase process as shown in **Figure 4.7**a.

In contrast to experiments conducted on surfaces with varied solid-liquid fraction, viscous dissipation, which is related to the contact area of the drop, is not influenced by variation of chemical surface modification as shown in **Figure 4.7**b.
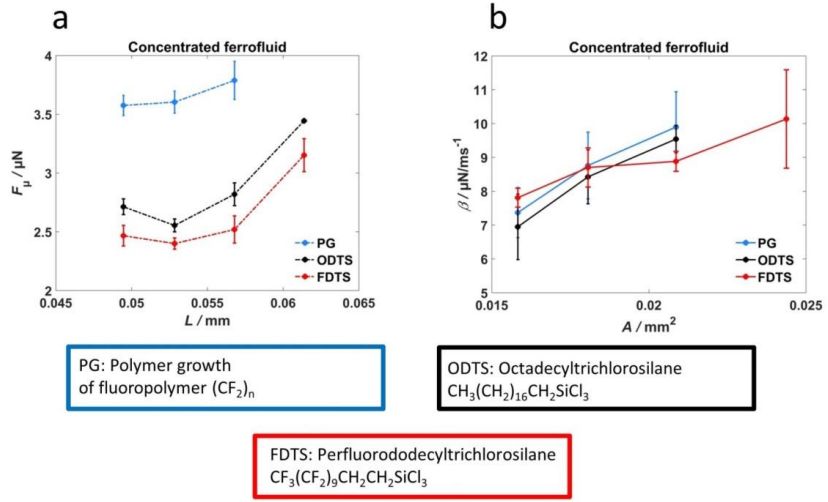
Figure 4.7. Dissipative forces obtained from droplet oscillation measurements conducted on micropillared superhydrophobic surfaces each subjected to distinct surface modification procedure. Solid fraction is 1.23 %. a) CAH force (F_μ) as function of contact line length (L). b) Viscous dissipation coefficient (β) as function of the drop contact area (A). (Al-Azawi et al. unpublished).

It is worth mentioning that the contact line fraction of the dynamic droplet on the micropillared superhydrophobic surfaces was assumed to be equal to the solid-liquid fraction φ_s. This assumption is based on the approximation of circular three-phase contact line of the droplet on the micropillared superhydrophobic surface. The value of contact line fraction ($\kappa = L/L_{TCL}$) was estimated by employing a simple simulation where a circle of a random size is generated at a random location on an array of pillar tops whose dimensions are similar to those of the fabricated micropillars. The result of two simulation runs of the three-phase contact line on two arrays one with $\varphi_s = 0.0218$ and the other one with $\varphi_s = 0.0097$ is displayed in **Figure 4.8**. Intersection points of the contact line with the top surface of the pillars are indicated by the red markings. The simulation shows that the contact line intersects with six pillars on the array with $\varphi_s = 0.0218$, on the other hand it intersects with three pillars on the array with $\varphi_s = 0.0097$. For each array, the simulation was repeated 30 times. The obtained values of the contact line fraction are 0.0215 ± 0.0095 for the array with $\varphi_s = 0.0218$ and 0.0110 ± 0.0076 for the array with $\varphi_s = 0.0097$. Additionally, the contact line fraction values for the arrays with $\varphi_s = 0.016$ and $\varphi_s = 0.0123$ are 0.0149 ± 0.0060 and 0.0163 ± 0.0057, respectively.
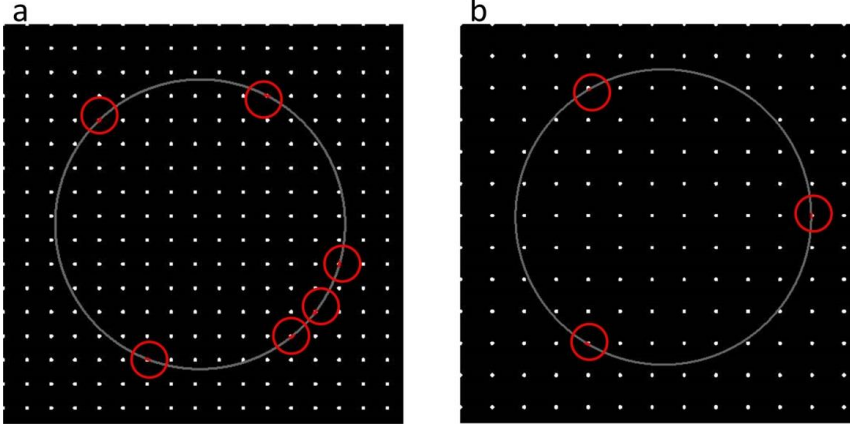
Figure 4.8. Simulation of the three-phase contact line on the pillar arrays. Contact line fraction is calculated by finding the portion of the contact line length, which is in contact with the pillar tops. a) Pillared surface of solid-liquid fraction equal to 0.0218. The calculated value of the contact line fraction is 0.0215 ± 0.0095. b) The solid-liquid fraction of the surface is equal to 0.0097 and the calculated value of the contact line fraction is 0.0110 ± 0.0076.

The similarity between the contact line fraction and the solid-liquid fraction can be shown by describing the apparent contact angle on the superhydrophobic surface in terms of the contact line fraction.[121] First, we must consider the formula for the work of adhesion (W_a) given by the Young-Dupré equation[122]

$$W_a = \gamma_{SV} + \gamma - \gamma_{SL} = \gamma(1+\cos\theta) \tag{4.1}$$

Equation 4.1 refers to the work required to separate a water droplet from the solid surface. For a droplet on a composite air-solid superhydrophobic surface, the work of adhesion along the length of the three-phase contact line (W_{TPCL}) is given by the Pease's equation[121,123] (**Equation 4.2**)

$$W_{TPCL} = W_{SL}\,L_{SL} + W_{LV}\,L_{LV} \tag{4.2}$$

The work of adhesion along the contact line length of solid-liquid interface (L_{SL}) is W_{SL}, whereas the work of adhesion along the contact line length of liquid-vapor interface (L_{LV}) is W_{LV}. Applying **Equation 4.1** into **Equation 4.2** yields[121]

$$\gamma(1+\cos\theta)\,L_{TPCL} = \gamma(1+\cos\theta_{SL})\,L_{SL} + \gamma(1+\cos\theta_{LV})\,L_{LV} \tag{4.3}$$

θ, θ_{SL}, θ_{LV} denote the apparent contact angle, the equilibrium contact angle on smooth solid surface, and the contact angle with air, respectively. Dividing **Equation 4.3** by ($L_{TPCL}\,\gamma$) and knowing that the solid-liquid and liquid-vapor contact line fractions are given by $\kappa_s = L_{SL}/L_{TPCL}$ and $\kappa_v = L_{LV}/L_{TPCL}$, respectively, we obtain

$$(1+\cos\theta) = (1+\cos\theta_{SL})\,\kappa_s + (1+\cos\theta_{LV})\,\kappa_v \tag{4.4}$$

Noting that $\kappa_s + \kappa_v = 1$ **Equation 4.4** becomes[121]

$$\cos\theta = \kappa_s \cos\theta_{SL} + \kappa_v \cos\theta_{LV} \tag{4.5}$$

Equation 4.5 relates the apparent contact angle to contact line fractions and is based on the balance between the works of adhesion along the three-phase contact line.[121] The similarity between the contact line fraction and the contact area fraction is evident when **Equation 4.5** is compared to **Equation 2.14**, which relates the apparent contact angle to the contact area fractions. This similarity was verified by the estimation of the contact line fraction through the simulation presented in **Figure 4.8**.

4.4 Cassie–to–Wenzel transition of magnetic droplets on micropillared superhydrophobic surfaces

A major challenge in the application of superhydrophobic surfaces is the transition of the droplet from Cassie state to Wenzel state. Upon such transition, low droplet friction and high mobility is lost. A droplet in metastable Cassie state has to overcome threshold of energy barrier to be in Wenzel state. Hence, impalement of water-air interface is observed by applying pressure. In publication I, CW transition and its dependence on solid-liquid fraction is studied. It was observed that the pressure at which a droplet in motion undergoes transition on a surface of constant solid-liquid fraction is lower compared with a static droplet on the same surface. Critical pressure (P_c) is defined as the maximum sustainable pressure acting on the structure before CW transition occurs. It is reached by increasing the normal force for each subsequent droplet oscillation until the droplet undergoes CW transition. At the instance of transition, the total force exerted at the water-air interface is expressed in terms of the critical pressure as $P_c(1 - \varphi_s)A_c$, where A_c is the repeated unit area also denoted unit cell area illustrated in **Figure 2.9**. Up to the point of transition the total force is countered by the vertical component of the water-air interfacial tension acting on the cross-sectional perimeter (S) of the pillar and is given as $-\gamma S\cos\theta_A$. A unified expression of (P_c)[72,80] valid for different values of solid-liquid fraction and pillar cross-section is obtained by re-arranging **Equation 2.21**.

$$P_c = \frac{-\gamma S \cos\theta_A}{(1-\varphi_s)A_c} \tag{4.6}$$

When the total pressure inside the droplet exceeds P_c, the ferrofluid droplet undergoes transition to Wenzel state as the contact line depins from the side of the pillars. Analytically calculated P_c values are compared with CW transition pressure values that were determined experimentally for dynamic droplets as well as static droplets. The comparison is presented in **Figure 4.9**, where both analytical and experimental critical pressure values increase as the solid-liquid fraction increases from $\varphi_s = 0.97$ % to $\varphi_s = 2.18$ % (**Figure 4.9**a). Higher pressure values of CW transition compared with the analytical P_c

values can be attributed to contact line pinning to sidewall roughness of the pillars (**Figure 4.1**b).

The applied pressure and φ_s relation to friction and wetting transition is presented through four regions (**Figure 4.9**b). Increasing the normal force induce either CW transition or heavily damped droplet oscillation depending on φ_s. On surfaces with low φ_s values, dynamic droplet is prone to collapse into Wenzel state. Oscillation may be heavily damped due to enhanced friction on surfaces with high φ_s values. Factors contributing to CW transition of the dynamic droplets at lower pressure values compared to static droplets may include fluid rotation inside the droplet, vibrations and variation in the magnetic field induced normal force.
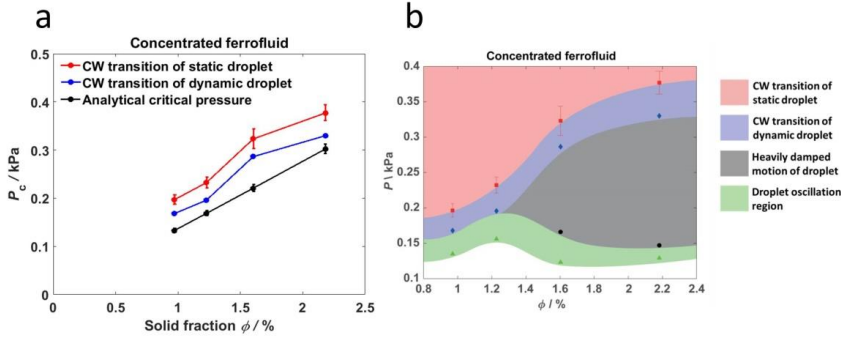

Figure 4.9. The influence of solid-liquid fraction of 10 µm diameter pillared surfaces on Cassie-Wenzel transition. Ferrofluid (4 vol. %) is used in the experiments. a) Comparison of analytical calculated critical pressure to experimental Cassie-to-Wenzel transition pressure of both dynamic and static droplets. b) Different regions are categorized according to the effect of pressure and solid-liquid fraction on droplet oscillation and wetting transition. The regions are: droplet oscillation, heavily damped motion and Cassie-to-Wenzel transition of dynamic and static droplets. Reproduced with permission from publication I. Copyright @ 2017 John Wiley & Sons, Inc.

By maximizing the value P_c, superhydrophobic surfaces can better withstand CW transition. Design considerations that can be taken into account when designing robust superhydrophobic surfaces are summarized in the following.

1) Increasing φ_s leads to higher P_c according to **Equation 4.6**. However, this results in an undesired increase of CAH.

2) Increasing the cross-sectional perimeter by changing the shape of micropillar's cross-section while keeping φ_s and unit cell area A_c unaltered. For example, ~13 % increase in P_c is achieved if micropillars of square cross-section are used instead of micropillars of circular cross-section.[80]

3) Reducing the scale of both cross-sectional area and A_c by factor $(1/x)$ while keeping φ_s unaltered lead to (x) times increase in P_c. For example, P_c for a square array of 10 µm diameter pillars having φ_s = 0.0314 is 0.458 kPa. In comparison, P_c for a surface consisting of 50 nm (10 µm/200) diameter pillars that also arranged in square array and having similar solid-liquid fraction φ_s = 0.0314, is 91.6 kPa. This value of P_c is comparable with the impact pressure of a rain drop, which is 10–100 kPa.[80,124] Therefore surface topography of hydrophobic densely packed pillar like structure in the sub-µm range such as

the structure of the cicada wings (**Figure 1.2**) and the black silicon surface treated with hydrophobic coating (**Figure 1.3**) exhibit remarkable robustness making them efficient self-cleaning surfaces.

5. Responsive Superhydrophobic Surfaces

Advancement in research of superhydrophobicity requires development of fabrication processes that impart advanced functionalities to surfaces. Successful application of superhydrophobic surfaces requires certain capabilities like maintaining high droplet mobility, robustness against collapse to fully wetting Wenzel state, wear resistance and compatibility with different materials. Material of choice is therefore a key point for synthesizing superhydrophobic surfaces that besides of fulfilling fundamental capabilities can manifest expanded functionalities like responsive properties.

Nature provides several examples of surfaces with intriguing properties. Biomimicry is adopting smart solutions observed in nature by engineering surfaces that mimics these solutions. Among remarkable phenomena found in nature is the microscale ciliary structure covering organs such as cilia present on the respiratory passage and epithelial passage responsible for clearing mucus.[125,126] The beat motion of this class of cilia induces motion and performs vital transportation processes.[127] Another class of cilia is stationary cilia, which main function is sensing.[128]

Inspired by cilia, development of artificial stimuli-responsive surfaces has gained significant interest due to the potential of achieving enhanced sensing performance and fluid manipulation in analytical microsystems. Reversible switching on demand of surface topography can be triggered by thermal gradients,[129] magnetic field gradient,[130–133] electric field[134] and mechanical force[135,136] allowing multiple functions like tunable wetting,[137] tunable light transmittance,[138] tactile sensing,[136] and tunable adhesion.[139] Cilia inspired stimuli-responsive surfaces based on magnetically actuated pattern has emerged as a strong candidate due to 3D motion capability and the non-invasive nature of the magnetic fields, which enable real-time manipulation without adversely affect the system in which they operate. This is especially beneficial for real-time manipulation of living cells.[140,141]

Both polydimethylsiloxane (PDMS) and thiol-ene are polymeric flexible materials that offer excellent compatibility with existing microfabrication techniques and can accommodate magnetic particles easily. PDMS has several advantages including flexibility, transparency and biocompatibility,[142,143] however permeability constitute an issue.[144] Thiol-ene is a viable alternative as it offers similar advantages such as flexibility and transparency but unlike PDMS it does not exhibit swelling in solvent due to the low permeability.[145,146] Moreover, thiol-ene features fast curing by UV exposure, ability to tune the

mechanical properties through composition chemistry and modification of surface chemistry or topography is achieved through reaction of surface groups.[147−149]

Tuning the surface and the mechanical properties of magnetic cilia to induce superhydrophobicity allows controlled droplet manipulation, which is important for different technological applications.[132,138,150,151] Digital microfluidics,[152] liquid collection[153] and interfacing with biomatter[154] are among applications that can benefit from remote control and real-time non-destructive tuning of the pattern geometry.

Fabrication of magnetic cilia applied to droplet manipulation can be divided into two categories. A template-free bottom-up approach where the structure is defined by the intensity of the magnetic field lines shaping prepolymer mixed with magnetic particles into array of micropillars along the direction of the magnetic field.[131,150,155−158] In the second approach replica molding process is utilized to replicate the structure from a patterned mold.[130,151,159−161] Compared with the first approach, replica molding technique allows control over the pitch, the aspect ratio (AR) and the diameter of the cilia-like pillars. Despite the simplicity of the maskless method of the first approach, non-uniform distribution of the magnetic ciliary structure adversely influences the application and limits the integration within microsystems.

This chapter focuses on fabrication and application of cilia-inspired magnetic micropillared surfaces for water droplet manipulation. Aspects such as tunability and elastic as well as surface properties are explored for both PDMS and thiol-ene cilia-inspired magnetic micropillars.

5.1   Fabrication of magnetically responsive surfaces

Fabrication of cilia-inspired PDMS and thiol-ene magnetic micropillars involves common process steps and materials. In both cases the fabrication process starts by preparing silicon micropillared master. The fabrication process of the master was elaborated in **Section 4.1**. Silicon was selected as the template material because high AR pillars are obtained easily using Bosch process (publication II and publication III). Fabrication of sub-10 μm diameter pillars having AR ≥ 8 using silicon micromachining is therefore preferred over using SU8 (epoxy based resist) micromachining. Achieving standing pillars of similar dimensions in SU8 is challenging due to bending and irregular deformation.[162]

Following master fabrication, micromolding process is utilized to produce a PDMS template, which in turn is used to produce thiol-ene or PDMS micropillared surfaces by double replication process. Magnetic actuation is enabled by embedding superparamagnetic carbonyl iron particles (CIP) within PDMS or thiol-ene during the fabrication process.

Except from template preparation, different process steps are tailored for each type of magnetic micropillars as presented in publication II and publication III. In the following a step-by-step description of both PDMS and thiol-ene magnetic micropillars fabrication is given.

The PDMS template selected for the replication of PDMS magnetic micropillars, the process of which is presented in **Figure 5.1**, was treated with FDTS by CVD after oxygen plasma treatment (**Figure 5.1**a). Modifying the surface with low energy SAMs is a necessary step to ensure separation of PDMS magnetic micropillars from the substrate. Next, superparamagnetic carbonyl iron particles (CIP) were mixed with PDMS 50 wt. %. PDMS-CIP composite was then poured on to the template (**Figure 5.1**b) followed by placing a flat layer of cured PDMS that have similar dimensions to the template. The flat layer was pushed gently in order to squeeze the PDMS-CIP composite into the cavities. The assembly was then fixed on top of a permanent magnet before curing it in the oven (**Figure 5.1**c). This way, a thin layer of PDMS-CIP composite is confined between the flat layer and the template while the assembly is fixed above the magnet. After curing, the assembly was soaked in liquid nitrogen. The mismatch in thermal expansion coefficient between the PDMS template and the PDMS-CIP composite layer causes cleavage at the interface resulting in separation of the template from the CIP-PDMS composite attached to the flat PDMS layer (**Figure 5.1**d). This cryogenic separation yields a clean template where PDMS-CIP composite is confined within the cavities only. Afterwards, a new PDMS is prepared and poured onto the PDMS template and subsequently cured in the oven to form a substrate layer (**Figure 5.1**e). Unlike the surface of the template, the PDMS within cavities was not subjected to FDTS treatment. As a result, the substrate layer only binds to PDMS within cavities during curing. Finally, the template is manually separated from the substrate layer, which after separation has the magnetic pillar array attached to it (**Figure 5.1**f). At this point, the PDMS template can be re-used to produce another sample of magnetic micropillars.

A weight ratio of 10:1(base elastomer: curing agent) was chosen in all of the PDMS processing.
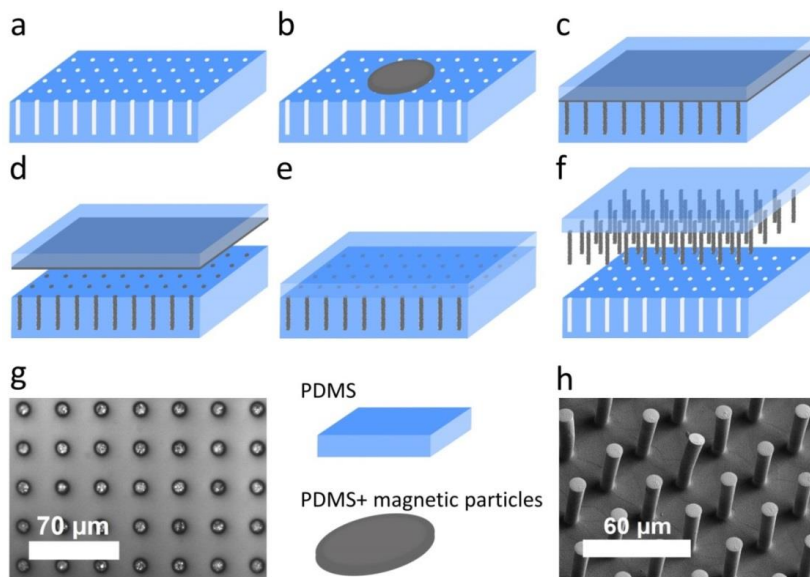
Figure 5.1. Fabrication and characterization of PDMS magnetic micropillars. a) PDMS template obtained by micromolding and treated with hydrophobic self-assembled monolayer of perfluorododecyltrichlorosilane (FDTS). b) PDMS-carbonyl iron particles (CIP) composite applied onto the surface of the template. c) Backing layer of flat and cured PDMS is placed on top of the template and the assembly is fixed above a permanent magnet followed by curing in the oven. d) The assembly is soaked in liquid nitrogen causing cleavage of the PDMS-CIP composite layer at the interface with the PDMS template. e) Uncured PDMS is poured onto the template followed by curing to form a substrate layer. f) The substrate layer with the magnetic pillars attached to it is manually separated from the template in ethanol. g) Inspection of the PDMS template after the separation step (d) by optical microscopy. h) SEM characterization of the magnetic pillars (aspect ratio = 4.8) after separation from the template in step (f) and freeze drying. (Publication II).

Cryogenic separation implemented in the fabrication process produces transparent templates where magnetic particles are confined within the cavities only. This was confirmed by optical microscope characterization of the template (**Figure 5.1**g). This process step eliminates the need of removing excess particles from the patterned template. After replication, only magnetic micropillars and not the sample as a whole respond to the magnetic field.

Additionally, the template can be used multiple times for replication of the magnetic micropillar array. Visualization of such array was done by SEM (**Figure 5.1**h).

Photocurable thiol-ene has emerged as a viable option in the fabrication of polymeric microdevices due its remarkable features like the ability to tune surface as well as mechanical properties, fast curing, transparency, presence of reactive functional groups and compatibility with the established micromolding techniques.[145,146]

Thiol-ene photopolymerization is based on the addition of thiol groups to allyl groups. The reaction can be triggered simultaneously by UV illumination or through radical initiator. The initial step of the reaction is the formation of thiyl radical by cleavage of S-H bond of a thiol functional group through

58

photolysis or radical initiator. The reaction continues by the addition of the formed thiyl radical to an allyl functional group to form a carbon centered radical (propagation). Then the thiyl radical is regenerated by transfer of a hydrogen atom from another thiol functional group to the carbon centered radical (chain transfer). The thiyl radical continues propagation and chain transfer reactions. At the end, different radical-radical recombination reactions occur (termination).[145–147]

In Publication III, a fabrication process for thiol-ene magnetic micropillars is developed. A schematic illustrating the fabrication steps is shown in **Figure 5.2**a. Once the PDMS template was prepared (**Figure 5.2**a-i), it was placed inside a Petri dish and treated with oxygen plasma to clean and increase the surface energy of the template. Next, the selected thiol-ene mixture was poured into the Petri dish, which was placed on top of a permanent block magnet (**Figure 5.2**a-ii). Afterwards, thiol-ene mixed with CIP was pipetted onto the template followed by moving the magnet in contact with the backside of the Petri dish back and forth for 5 min. to drive CIP into the thiol-ene filled cavities (**Figure 5.2**a-iii). To improve the packing of CIP within the cavities, the Petri dish was subjected to two sonication steps, each with 80-90 sec. duration. First step was done without magnet followed by a sonication step on top of the magnet (**Figure 5.2**a-iv). CIP excess was then scraped off the template while it was placed on top the magnet and immersed in thiol-ene. A mixture of thiol-ene that has not been mixed with CIP was then added to the Petri dish after withdrawal of the same amount to refresh the thiol-ene layer above the template. UV flood exposure was then applied to cure thiol-ene (**Figure 5.2**a-v). Finally, the template was cut from the surrounding thiol-ene within the Petri dish and manually separated from the thiol-ene layer in ethanol (**Figure 5.2**a-vi). At this point the thiol-ene sample was ready for actuation. Implementing freeze-drying of thiol-ene sample after fabrication allowed SEM characterization of the arrays as shown in **Figure 5.2**b. In addition, characterization by optical microscopy allowed inspection of CIP distribution within thiol-ene micropillars (**Figure 5.2c**). The magnetic micropillars were collapsed by N_2 flow prior to the characterization.

Reliable fabrication of thiol-ene magnetic micropillar arrays constitutes a foundation for further modification. The tailorable properties of thiol-ene due to composition and reactive chemistry allow tuning of surface and elastic properties.

Magnetic actuation of PDMS as well as thiol-ene micropillar arrays is presented in **Section 5.2**. Surface and elastic properties are detailed in **Section 5.3**.
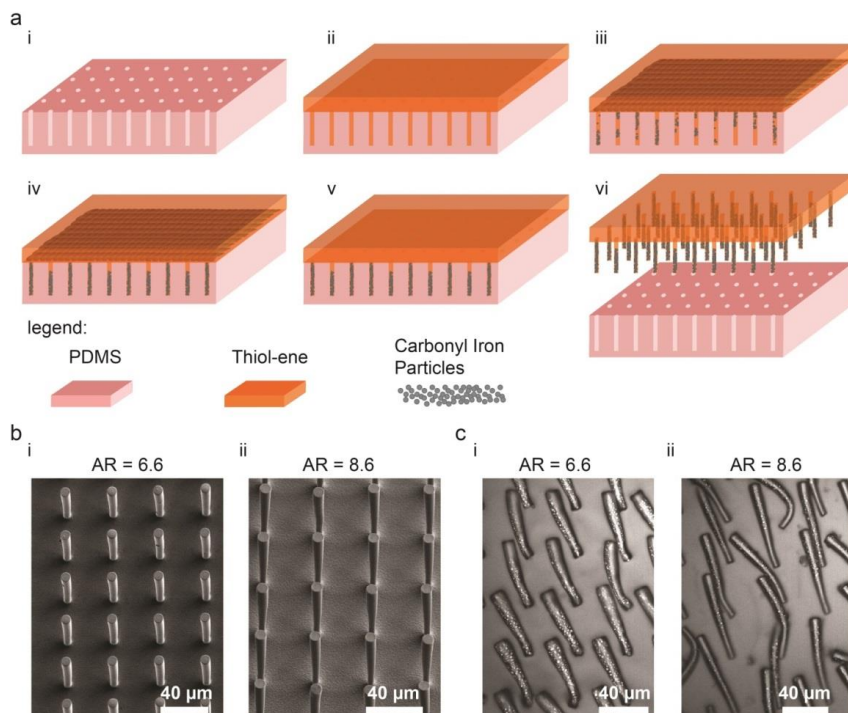
Figure 5.2. Thiol-ene magnetic micropillars synthesis and characterization. a) Sketch of the fabrication process. i) The PDMS template is obtained from micropillared silicon master by soft lithography process. ii) Uncured thiol-ene without carbonyl iron particles (CIP) is poured onto the template. iii) The template is placed on top of a permanent magnet and uncured thiol-ene mixed with CIP is pipetted onto the PDMS template, which was immersed in thiol-ene. iv) Combination of sonication and magnetic field is applied to improve the distribution of CIP within thiol-ene filled cavities of the template. v) Curing of the thiol-ene layer by UV exposure. vi) Separation of the thiol-ene layer from the template in ethanol. b) SEM inspection of two arrays of thiol-ene micropillars after separation and freeze drying. The micropillars are identified according to the value of aspect ratio (AR). c) Optical microscopy characterization of the thiol-ene magnetic micropillars after separation and N_2 flow reveals the distribution of CIP. Reproduced with permission from publication III. Copyright @ 2020 John Wiley & Sons, Inc.

5.2 Bending of magnetic micropillars

Powerful bending actuation of PDMS as well as thiol-ene magnetic micropillars is demonstrated in this section. Omnidirectional bending of the cilia-inspired magnetic micropillars was achieved by magnetic field gradients directed by a permanent magnet, which was controlled manually beneath the sample and in close proximity to it. Actuation of the pillars is demonstrated while the sample was immersed in a liquid medium to avoid pillar collapse caused by the capillary force acting on the free end of the pillars during evaporation of the liquid.[163,164]. The gap between the magnet and the sample was approximately 2 cm during actuation. Magnetic field strength measured with gauss meter is 150 – 200 mT. Magnetic actuation of PDMS magnetic micropillars is illustrated in **Figure 5.3**, which shows bending of micropillars of AR = 4.8 and AR = 8.8.
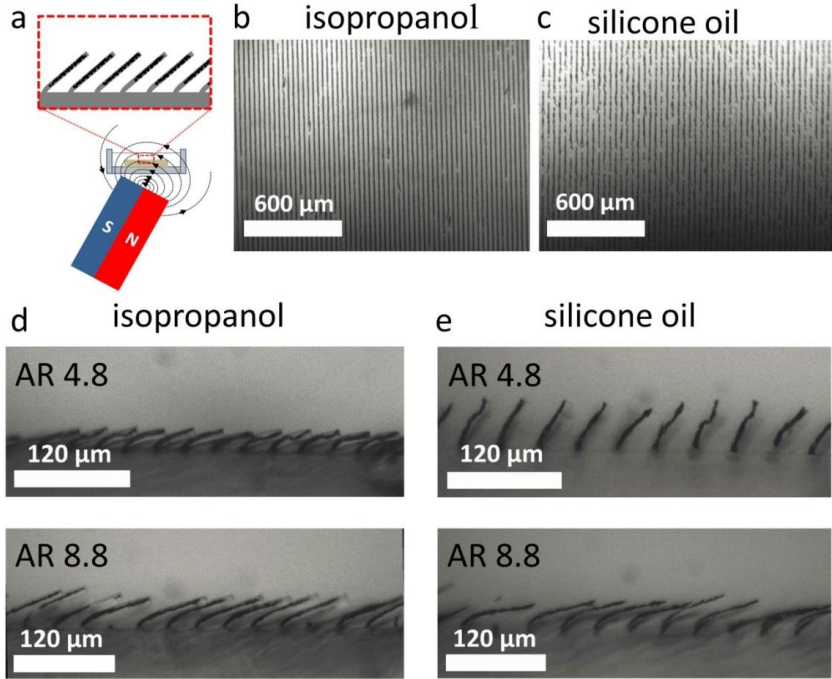
Figure 5.3. Actuation of PDMS magnetic micropillars. a) Schematic of the bending actuation by a permanent block magnet. b, c) Snapshot images of videos recorded by optical microscopy showing top view of magnetic actuation of the micropillar array in isopropanol (b) and silicone oil (c). The aspect ratio of the micropillars is 8.8. d, e) Snapshot images showing side view of magnetic actuation of micropillars of aspect ratio 4.8 and 8.8 in isopropanol (d) and silicone oil (e). The images are acquired from videos captured by optical microscopy. (Publication II).

In silicone oil ($[-Si(CH_3)_2O-]_n$, viscosity: 5 cSt, density: 0.913 g/mL) micropillars of AR = 4.8 bend to less extent compared with the micropillars of AR = 8.8. Limited bending is attributed to change of the elastic properties of PDMS in oil. The permeability of PDMS allows infiltration of solvents into the polymer matrix causing swelling and change in mechanical properties. The swelling ratio (S_W) is a parameter indicating the degree of PDMS swelling in different solvents and is estimated as $S_W = D/D_o$, where D is the PDMS segment length in a solvent and D_o is the length of the dry PDMS segment.[144] The swelling ratio of PDMS in isopropanol is 1.09[144] and in publication II, the estimated value of S_W for PDMS in silicone oil is 1.31.

Flexible micropillars bend along the direction of the magnetic field. The relation between bending and the external magnetic field can be established by balancing the elastic torque (bending moment (M_B)) and the magnetic field torque (T_m) as following[139,165]

$$M_B = T_m \tag{5.1}$$

Small angle bending equation is given as follows[166]

$$EI\frac{d^2\delta(z)}{dz^2} = M_B \tag{5.2}$$

Using **Equation 5.1** and the expression of the magnetic field torque, the following relation is obtained

$$EI \frac{d^2 \delta(z)}{dz^2} = V_M MB \sin(\alpha - \vartheta) \qquad (5.3)$$

(E) is the elastic modulus, (I) is the second moment of area of the pillar cross-section, $\delta(z)$ is the deflection along the micropillar height, V_M is the volume of the magnetic material, M is the magnetization of the micropillar, B is the external magnetic field, (ϑ) is the deflection angle of the micropillar and (α) is the angle of the magnetic field. Both angles are defined with respect to the original axial direction of the pillars, i. e. $\vartheta = 0°$ for upright pillar and $\alpha = 90°$ for a magnetic field perpendicular to the sidewall of the free end of the micropillar. ($\alpha - \vartheta$) is the angle between the tilted magnetic micropillar and the magnetic field at the pillar top.

Solving **Equation 5.3** by applying the boundary conditions: $\frac{d\delta(z)}{dz} = 0$ and $\delta(z) = 0$ at $z = 0$ yield[165]

$$\tan \vartheta = \frac{V_M MB \sin(\alpha - \vartheta)}{EI} z \qquad (5.4)$$

Considering a point load at the pillar top where $z = h$ and knowing that the second moment of area is $I = \pi d^4/64$, **Equation 5.4** is written as

$$\tan \vartheta = \frac{64 V_M MB \sin(\alpha - \vartheta)}{E \pi d^4} h \qquad (5.5)$$

A formula for the equilibrium deflection angle is given as[138,139,167]

$$\vartheta = \frac{V_M MB \sin(\alpha - \vartheta)}{K_\vartheta} \qquad (5.6)$$

$K_\vartheta \vartheta$ is the elastic torque and $K_\vartheta = c_0(EI/h)$ is the equivalent torsion spring constant,[138] where c_0 is a correction coefficient. For array of micropillars of similar dimensions and magnetization, the elastic modulus and pillar height are the factors contributing to the extent of deflection during pillar bending. Compared with micropillar actuation in isopropanol, pillars immersed in silicone oil exhibit limited bending for pillars of AR = 4.8 due to an increase of the elastic modulus.

Thiol-ene magnetic micropillars also display simultaneous bending in the presence of magnetic field gradient. In contrast to PDMS magnetic micropillars, swelling was not noticed during the actuation of thiol-ene pillars. This was confirmed by carrying out side-by-side comparison of micropillars actuation in oil and in ethanol (part of the work included in Publication III).

Collective actuation of thiol-ene magnetic pillars in ethanol is demonstrated in **Figure 5.4**.
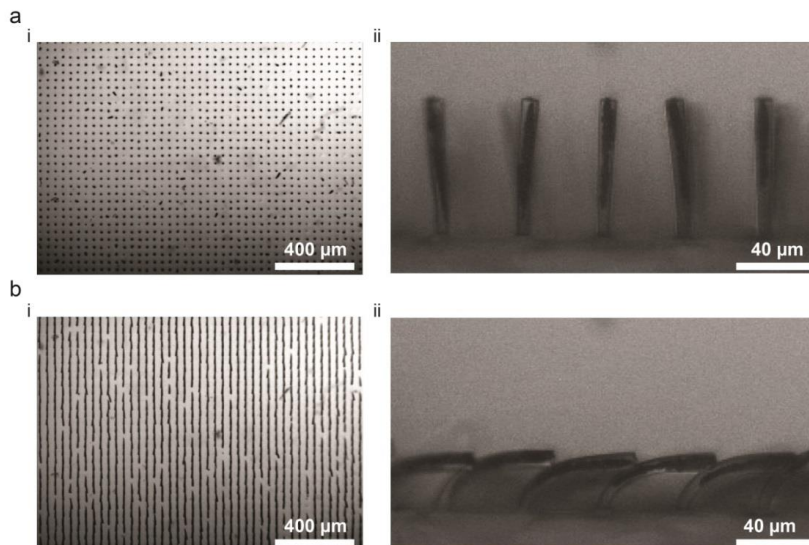
Figure 5.4. Snapshot images of recorded videos by optical microscopy showing collective bending of thiol-ene magnetic micropillars in ethanol. a) Magnetic field off: top view (i) and side view (ii) of the micropillars before actuation. b) Magnetic field on: top view (i) and side view (ii) of the micropillars during actuation. Reproduced with permission from publication III. Copyright @ 2020 John Wiley & Sons, Inc.

5.3 Elastic and surface properties

Bending with large deflection angle and fast response time are prerequisites for various applications of the cilia-inspired magnetic micropillars. Identifying parameters that produce magnetic micropillars of low elastic modulus is beneficial since it enables large deflection at low magnetic field strength. Therefore evaluating the elastic properties of thiol-ene as well as PDMS magnetic micropillars is crucial. Synthesis and testing of the magnetic micropillars with varying elastic properties are detailed in publication II and publication III.

A fixed weight ratio of 10:1 (base elastomer: curing agent), uniform PDMS-CIP composite without aggregation, no phase separation when the mixture was subjected to a magnetic field are confirmed during synthesis of PDMS magnetic micropillars. This means that the elastic property of the PDMS magnetic pillars fabricated by the process presented in **Figure 5.1** is determined by the percentage of CIP loaded and oil infiltration.

In the case of thiol-ene, factors contributing to the elastic properties are the functionality of thiol-ene monomers and the off-stoichiometric ratio, which are determined by the selected composition chemistry during synthesis. Thiol-ene is prepared by selecting the monomer components of thiol and allyl groups. In the simplest form thiol-ene is composed of two chemical components, one with thiol groups and the other with allyl groups. It is the stoichiometry and functionality of the chosen monomers that determine the elastic and surface properties of the replicated structure. Thiol-ene magnetic micropillars based on two types of thiol-ene mixtures are presented in

publication III. Thiol-ene mixture containing trimethylolpropane tris[3-mercaptopropionate] (trithiol) and trimethylolpropane diallyl ether (dialyl) result in flexible thiol-ene magnetic micropillars, whereas a mixture of trithiol with 1,3,5-triallyl-1,3,5-triazine-2,4,6(1H,3H,5H)-trione (triallyl) increases the crosslinking density and thus produces stiff pillars. Stoichiometry of the thiol-ene mixture also impacts the mechanical properties and the surface adhesion of the fabricated thiol-ene samples.

Investigation of the elastic properties was done by comparing Young's modulus values determined through tensile test measurements of thin segments of elastomeric materials. The results are presented in **Table 3**.

Table 3. Tensile tester characterization of elastomeric materials utilized in the fabrication of magnetic micropillars. The characterization yields values of Young's modulus of PDMS, oil infused PDMS, thiol-ene and thiol-ene subjected to oil immersion.

Sample	Young's Modulus [MPa]
PDMS	1.59 ± 0.05
Oil infused PDMS	1.80 ± 0.13
PDMS-CIP	2.05 ± 0.20
Oil infused PDMS-CIP	3.38 ± 0.41
Trithiol:Triallyl stoichiometric thiol-ene	788 ± 72
Trithiol:Diallyl off-stoichiometric thiol-ene (50% thiol excess)	1.17 ± 0.21
Trithiol:Diallyl stoichiometric thiol-ene	7.58 ± 0.52
Trithiol:Diallyl stoichiometric thiol-ene in oil	7.98 ± 0.96

Young's modulus value of PDMS obtained from the characterization is in agreement with several reports.[139,141,168,169] Further, loading PDMS with CIP or infiltrating it with silicone oil increases the measured value of Young's modulus.

The highest measured value of Young's modulus was observed for Trithiol:Triallyl thiol-ene. This is due to the higher functionality of allyl monomers leading to higher crosslinking density, and thus higher Young's modulus value. On the other hand, the off-stoichiometric ratio in the thiol-ene mixture leads to a reduction in the crosslinking density. The change in the measured value of Young's modulus is significantly less compared with selecting thiol-ene monomers with a higher degree of functionality.

Thiol-ene offers the ability to tailor the elastic properties by controlling the crosslinking density to an extensive degree. In fact it is possible to tune the elastic properties of thiol-ene from low Young's modulus values of less than 11 MPa[145] to high Young's value of 1750 MPa.[146] In comparison, tuning the elastic modulus of PDMS is limited between 0.5 MPa for the ratio 33:1 (base elastomer: curing agent) to 3.6 MPa for 5:1 ratio.[170]

Another technique was employed for the mechanical characterization of thiol-ene magnetic micropillars (publication III). Therein, local non-contact actuation of magnetic micropillars was achieved by a robotized

electromagnetic needle (**Figure 5.5**). The electromagnetic needle offers precision in manipulating microscale objects.[171] The mechanical properties of the pillars were characterized by relating the pillar deflection to the current supplied to the needle. The measurements were performed by positioning the needle at a fixed distance from the edge of the free end of the micropillar followed by supplying current at four subsequent steps starting at 150 mA and succeeded by an incremental increase of 150 mA in the following steps. Displacement of the micropillar (δ) for each current value was acquired and the procedure was repeated at an increased pillar-needle separation. In total, the characterization of a single micropillar involved measurements with four current values at four pillar-needle separations. Schematic representation of the measurement is shown in **Figure 5.5**a. Increased displacement δ of stoichiometric thiol-ene Diallyl:Trithiol micropillar as a response to an increasing supplied current is shown in **Figure 5.5**b. The effect of crosslinking density on δ was verified by measurements with supplied constant current of 600 mA on three micropillars each with distinct thiol-ene chemistry (**Figure 5.5**c). Small δ values was observed for the Triallyl:Trithiol pillar due to the increased crosslinking density. Results of the elasticity characterization for stoichiometric Diallyl:Trithiol micropillars and off-stoichiometric Diallyl:Trithiol micropillars are shown in **Figure 5.5**d and **Figure 5.5**e, respectively. Characterization results of Triallyl:Trithiol stoichiometric micropillars are shown in **Figure 5.5**f, where the two initial pillar-needle separation distances furthest away from the micropillar were disregarded because of barely noticeable δ.
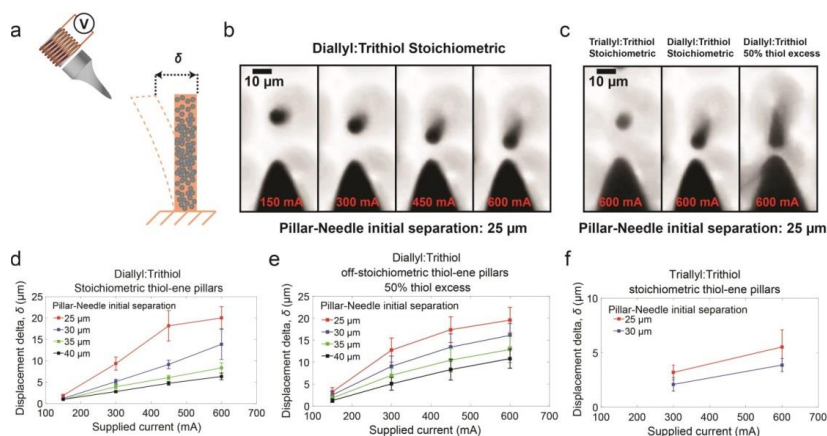
Figure 5.5. Elasticity characterizations using electromagnetic needle to measure displacement δ of thiol-ene magnetic micropillars immersed in water. a) Schematic illustration of the measurement. b) Snapshot images of videos captured by a high-speed camera show top view of Diallyl:Trithiol stoichiometric micropillars actuation with increasing displacement as a result of increasing current through the needle. c) The effect of crosslinking density on displacement δ of three micropillars each with distinct thiol-ene chemistry. Supplied current is 600 mA. d-f) Displacement δ as function of the supplied current to the needle at four initial separation distances between the needle and (d) stoichiometric Diallyl:Trithiol micropillars, (e) off-stoichiometric Diallyl:Trithiol micropillars with 50% excess thiol,(f) Triallyl:Trithiol stoichiometric micropillars. Reproduced with permission from publication III. Copyright @ 2020 John Wiley & Sons, Inc.

The consistent results prove that local actuation using electromagnetic needle is a viable option for probing the effect of crosslinking density variation.

In addition to elasticity, surface modification is of an equal significance to the functionality and application of magnetic micropillars. Surface modification was achieved through different strategies that depend on the material of the magnetic micropillars. For PDMS, tuning synthesis parameters like elastomer:curing agent ratio and curing temperature do not change the surface chemistry.[172] However, the surface energy of PDMS, which is 19-21 mN/m[173] can be increased by oxygen plasma. In addition, PDMS is compatible with different solvents manifested by the swelling of PDMS to different degrees indicated by the swelling ratio S_W.[144] As mentioned in the previous section the value of S_W in silicone oil is 1.31 indicating high compatibility with PDMS. The surface properties of the PDMS sample changes after immersion in silicone oil. This was confirmed in publication II by performing wetting characterization using contact angle goniometer. The measured ACA is 115.4° and RCA is 100.8° on flat PDMS in air. The corresponding values of PDMS magnetic micropillar samples immersed in silicone oil are ≈ 171° for both ACA and RCA. Negligible CAH confirms that super non-wettability is conferred to the PDMS magnetic micropillars due to the lubricant infusion. Slippery liquid infused porous surfaces (SLIPS) is a class of engineered materials that relies on lubricant infusion and features excellent liquid- and ice repellency, manipulation of droplets of different values of surface tension.[87,174–177] In the next section, water droplet manipulation by PDMS and thiol-ene magnetic micropillar arrays will be elaborated.

Surface modification of thiol-ene is facilitated by accessible allyl and thiol groups. The surface properties of thiol-ene depend on the off-stoichiometric ratio.[146] In publication III, surface adhesion measurement of stoichiometric Diallyl:Trithiol thiol-ene is compared with the a measurement conducted on Diallyl:Trithiol thiol-ene with 50 % excess thiol. The measured values of the maximum force of adhesion on flat thiol-ene surfaces are 0.51±0.14 mN and 1.05±0.1 mN for the stoichiometric and the off-stoichiometric thiol-ene respectively. This characterization is essential for the replication process as thiol-ene with a high level of adhesion is detrimental for the replication of the micropillars from the PDMS template.

The accessible surface groups are utilized for UV-grafting of polyvinyltrimethoxysilane (PVTMS) colloidal micro- and nanoparticles. The particles, which were prepared using Stöber method,[178] are terminated with allyl groups. UV initiated click chemistry reaction was utilized to covalently bond the particles onto the surface thus modifying the surface topography of the magnetic micropillars. Hydrophobic SAMs were then grafted onto the surface of the decorated micropillars to achieve superhydrophobicity.

SAMs were also grafted directly onto the surface of the thiol-ene micropillars. Converting surface allyl groups to thiol groups prior to functionalizing with the allyl terminated PVTMS particles was accomplished by UV grafting of 1,6-hexanedithiol. This was done to maximize the reaction sites with the colloidal PVTMS particles. Hydrophilic SAMs were also used to

66

modify the surface energy before freeze drying to allow SEM inspection of the pillars (**Figure 5.2**b).

Decorating the surface with PVTMS particles improves the stability of the micropillars without compromising the actuation capabilities. Arrays of decorated thiol-ene micropillar exhibit stability in the absence of a liquid medium. The conformal coverage of PVTMS colloidal particles provides an exoskeleton for the micropillars. Hence, the decorated high AR thiol-ene micropillars are not prone to the collapse driven by the capillary forces. This allowed actuation of the thiol-ene magnetic micropillar array in air as demonstrated in **Figure 5.6**.
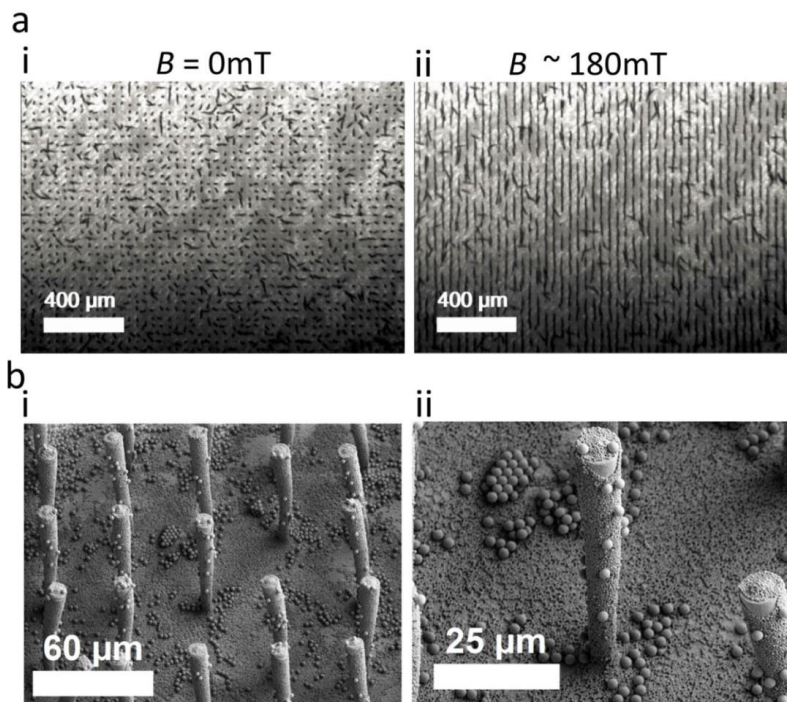
Figure 5.6. Topography modification of thiol-ene magnetic micropillars by polyvinyltrimethoxysilane (PVTMS) colloidal micro- and nanoparticles. a) Snapshot images of videos recorded by optical microscopy showing top view of the array of thiol-ene micropillars of aspect ratio 8.6 (i) before actuation and (ii) during actuation in air. b) Coverage of colloidal micro- and nanoparticles that are covalently bonded onto the surface of the micropillars as revealed by scanning electron microscopy of (i) array of micropillars and (ii) zoom-in of an individual micropillar.

Thiol-ene offers high level of surface tunability and low permeability to common solvents. The degree of surface roughness as well as the dimensions of the magnetic micropillars can be tuned by multiple steps of grafting colloidal PVTMS particles.

Pairing surface topography modification with grafting of hydrophobic SAMs produce responsive and robust superhydrophobic surfaces that can sustain and manipulate water droplets in Cassie state.

5.4　Applications of magnetic micropillars

Intriguing wetting phenomena relevant for many practical applications of superhydrophobic surfaces are associated with low CAH and robust Cassie state. Both of these two criteria are fulfilled by lubricant infused PDMS micropillars (Publication II) and decorated thiol-ene micropillars treated with SAMs (Publication III). Wetting characterization by contact angle goniometer yielded negligible CAH for oil infused PDMS pillars and the value of CAH for decorated thiol-ene pillars is 10°. Low value of CAH corresponds to low retention force (**Equation 2.27**). This combined with the fast actuation aided by the flexibility of the micropillars allowed controlled droplet motion driven by repetitive bending and recovery of the superhydrophobic magnetic micropillars as illustrated in **Figure 5.7**. The mechanism leading to the unidirectional droplet motion is composed of two steps namely; bending and recovery. During the first step, known as the magnetic stroke, each magnetic micropillar bends in response to the applied magnetic field, thereby accumulating elastic energy. The direction of the magnetic field is controlled manually by orienting the permanent block magnet beneath and in close proximity to the sample. The magnetic micropillars recover to the upright position releasing the accumulated elastic energy once the magnetic field is momentarily directed away from the sample. Unidirectional motion of the water droplet is caused by repeating the procedure of continuous bending (magnetic stroke) and recovery (elastic stroke). The same actuation mechanism has been applied to induce unidirectional motion of solid particles.
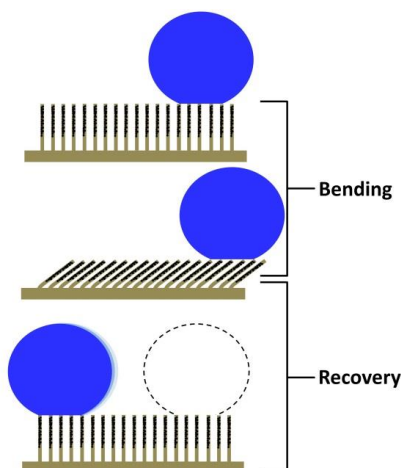
Figure 5.7. A schematic showing not-to-scale illustration of the mechanism leading to the unidirectional motion of a water droplet. The repeated sequence of bending and recovery of the magnetic micropillars causes directional droplet motion.

The driving force acting on the three-phase contact line of the droplet originates from continuous and collective bending and recovery of the magnetic pillars.

The relation between the force and the displacement of the pillar is expressed in the following[166]

$$F = 3\frac{EI}{h^3}\delta \qquad\qquad\qquad (5.7)$$

Equation 5.7 is deduced from the equation of small angle bending of beams **Equation 5.2**. To account for large deflection of the flexible pillars, a relation between dimensionless forces and deflections has been reported using numerical modelling.[169]

Repeated bending and recovery of the magnetic micropillars induces droplet motion. The omnidirectional bending capability of the pillars, fast response time and low adhesion to water droplet assist controlled water droplet motion along any direction. This is demonstrated in **Figure 5.8** where motion of 286 μm wide water droplet along different directions in silicone oil proceeds easily by the actuation of PDMS magnetic micropillars.

For thiol-ene magnetic micropillars, low CAH is attributed to the secondary roughness achieved through conformal coverage of colloidal PVTMS micro- and nanoparticles on the surface of the micropillars. Treating the particles with low energy SAMs of perfluorodecanethiol (FDT) lowers the surface energy. This allows directional water droplet by repeated bending and recovery of the micropillars as shown in **Figure 5.9**. In addition to superhydrophobicity, decoration of thiol-ene micropillars with sub-10 μm particles (2.2 μm average diameter) and sub-μm particles (547 nm average diameter) imparts mechanical stability so high AR thiol-ene micropillars can be actuated in air as well as in different liquid media. Droplet motion in this case was achieved in silicone oil to avoid evaporation of the droplet.

Topography modification of the thiol-ene micropillars produced samples of CAH ≈ 10°. Further reduction of CAH can be attained by increasing the degree of surface roughness in combination with grafting different type of hydrophobic SAMs.

Both PDMS magnetic micropillars and thiol-ene magnetic micropillars demonstrated the capability of directional transport of solid microbeads as reported in publication II and publication III.
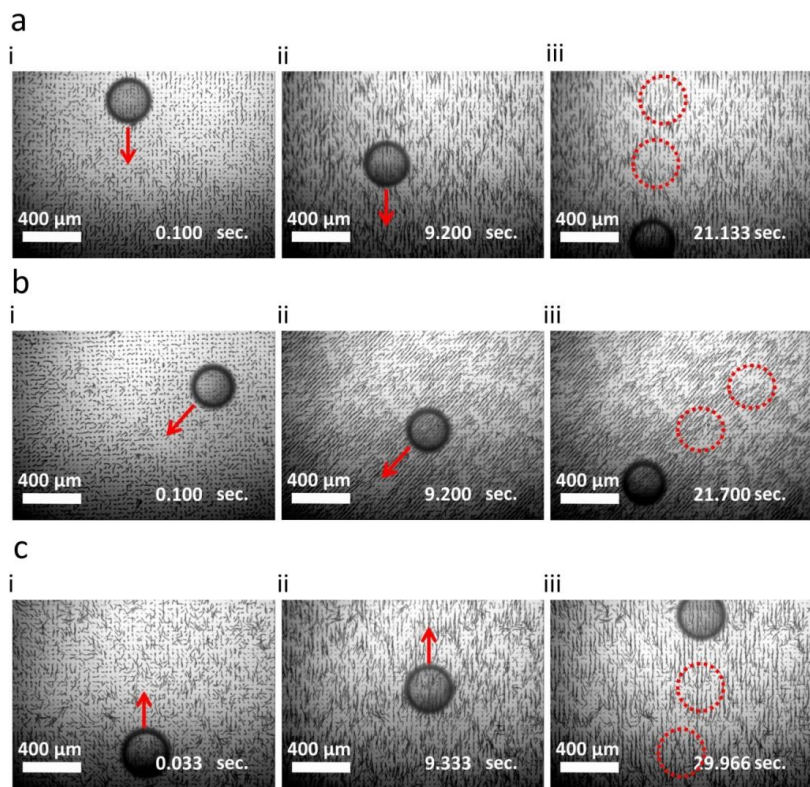
Figure 5.8. Controlled water droplet transport in silicone oil by repetitive bending and recovery of PDMS magnetic micropillars of AR = 8.8. a-c) Snapshot images of videos recorded by optical microscopy showing top view of the water droplet motion along different directions. The droplet is ≈ 286 μm wide and the velocity of motion induced by the pillars is ~ 2.75 mm/min. (Publication II).
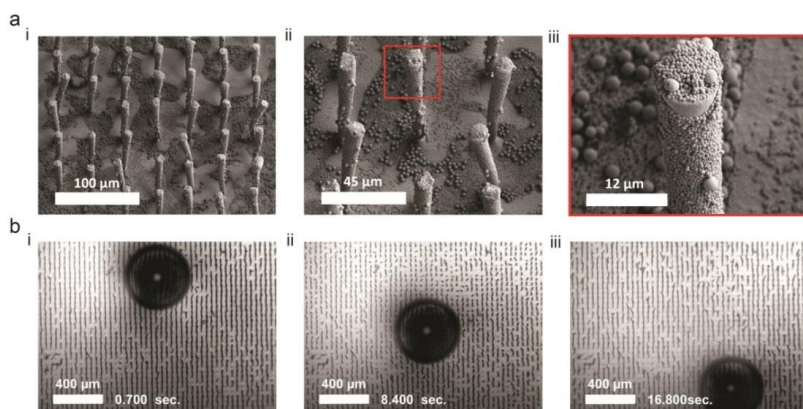
Figure 5.9. Droplet motion directed by thiol-ene magnetic micropillars of AR = 8.6. a) SEM images of thiol-ene magnetic micropillars decorated with polyvinyltrimethoxysilane (PVTMS) colloidal micro- and nanoparticles. b) Water droplet motion induced by repetitive bending and recovery of the micropillars as it is seen under the optical microscope. Reproduced with permission from publication III. Copyright @ 2020 John Wiley & Sons, Inc.

The unidirectional droplet motion shown in **Figure 5.8** and **Figure 5.9** was achieved along the direction of the elastic stroke. The same actuation mechanism can be applied to induce bubble motion. The magnetic micropillars exhibit under-oil superoleophilicity meaning that oil readily fills the interspaces of the surface microstructure forming a trapped layer that cannot be replaced by water droplets or air bubbles. In this case, the cilia-inspired micropillared surfaces show extremely low adhesion to air bubbles, which would rise up by the buoyant force instead of adhering to the surface. The adhesion force (F_a) and the buoyant force (F_b) are given as follows

$$F_a = \gamma(2\pi R_b \sin\varepsilon)\sin\varepsilon \tag{5.8}$$

$$F_b = \rho_f V_b g \tag{5.9}$$

Liquid-air interfacial tension, radius of the bubble, the angle between the surface and the tangent to the liquid-air interface at the point where the three immiscible phases meet, density of the ambient fluid and the volume of the bubble are denoted by γ, R_b, ε, ρ_f and V_b, respectively.

An air bubble can be supported on the surface by fixing the cilia-inspired micropillared sample upside down while immersed in oil. By virtue of repetitive bending and recovery of the magnetic micropillars, unidirectional motion of the bubble can be initiated along the direction of the elastic stroke (opposite direction to the pillar bending).

The properties of the cilia-inspired magnetic micropillars such as fast response time, stability against capillary-driven collapse and tunable elasticity enable essential applications within microfluidic devices ranging from fluid manipulation to sensing. One potential application is using the cilia-inspired magnetic micropillars as actuators to propel liquids in microfluidic devices.[130,179–181] Two different modes of collective pillar actuation can be implemented for the generation of fluid flow. The conical tilted motion is the first type of motion in which each magnetic pillar in the array exhibits rotational synchronous 3D asymmetric motion.[130,180] This type of motion consists of an effective stroke when each individual cilium beats straight as the tip is furthest from the surface and a recovery stroke when the cilia beat closer to the surface mimicking the motion of biological cilia in the embryonic node.[180,182] The second type of motion is metachronal 2D motion in which magnetic micropillars execute whip-like motion consisting of magnetic stroke and elastic stroke.[180] During magnetic stroke each pillar bends and assumes a curved shape as it aligns to the magnetic field, thereby accumulating elastic energy. In recovery stroke, the elastic energy is released resulting in rapid motion of the pillars as they recover to the upright position. Under the influence of periodic non-uniform magnetic field, the magnetic pillars beat in metachronal fashion, where slight phase difference between neighboring pillars is present.[180]

Ciliary fluid propulsion with synchronous 3D actuation mode was demonstrated in both water and glycerol. The maximum generated flow speed

of water is 90 μm/s achieved at an actuation frequency of 20 Hz.[180] At higher actuation frequencies flow speed drops due to inertial effects that counteract the flow.[180] In glycerol, flow speed of 120 μm/s can be reached at an actuation frequency of 60 Hz, which is the frequency limit of the rotating magnet below the sample.[180]

Fluid propulsion with the metachronal 2D motion actuation mode can achieve significantly higher flow speeds in water. At an actuation frequency of 100 Hz, the reported water flow rate is 3000 μm/s.[180] In this case, inertial effects contribute to the flow rate. In glycerol, where the inertial effects are absent, flow speed of up to 60 μm/s can be generated at actuation frequency of 100 Hz, which is the limit of the actuation setup. [180]

Application of the cilia-inspired magnetic micropillars as a microfluidic pump that is competitive to the existing pumping techniques can be accomplished by fulfilling the following criteria. First, a fabrication process capable of rapid prototyping of magnetic micropillars has to be utilized. In Publication II, a new fabrication method that can be easily adopted for the production of magnetic micropillar arrays in microfluidic systems is presented. Second, the magnetic micropillars must be flexible, resistant against capillary-force-induced collapse and exhibit fast response time, which is the time required for the pillar to reach steady state during actuation. The response time for Diallyl:Trithiol thiol-ene magnetic micropillars is 2.66 - 3.40 ms (Publication III) measured by the electromagnetic needle. Finally, the actuation setup must be compact, simple and can provide a periodic and non-uniform magnetic field.

Besides the application as an actuator that responds to an external stimulus, the magnetic micropillar arrays can function as a sensing element as well.[135,136] One potential application of the magnetic micropillars is within flow sensing.[135] Fluid flow monitoring is important for lab-on-a-chip devices, medical instrumentation, chemical and automotive industries. A widely implemented approach for measuring the fluid flow using miniaturized systems is based on thermal flow sensing.[183–185] In this technique, the flow rate is determined by registering the heat transferred per unit time from a resistive wire heater to a moving fluid by two thermistors. Thermal flow sensors have high detection limit with resolution below 10 mm/s at low power consumption of 177 μW.[184] However, increasing the resolution can come at the expense of increased power consumption.[185]

Non-invasive flow sensors based on cilia-inspired magnetic micropillars provide an attractive alternative as they can be tuned to operate with power consumption as little as 80 nW while maintaining a resolution of 32 μm/s.[135] The advantages of developing flow sensors based on the principle of detecting flow by bending of the decorated thiol-ene micropillars are clear in that the elastic properties are tunable enabling detection of wide range of fluid flow velocities. In addition, resistance against corrosion of the magnetic particles is ensured by the limited permeability of thiol-ene. These advantages combined with the mechanical stability of the decorated pillars make them prominent choice for detection of liquid flow rates within microfluidic systems.

The operating principle is based on the integration of the pillar array on top of giant magneto impedance (GMI) sensor, which consists of 200 nm thick Cu layer sandwiched between two 100 nm thick $Ni_{80}Fe_{20}$ layers.[135] The magnetic pillars are embedded with ferromagnetic particles or rods. The GMI sensor has magnetic anisotropy along the longitudinal axis achieved by applying magnetic field in the transverse direction during the deposition of the thin film layers.[135,136] The segment occupied by the multilayer GMI sensor is 400 μm wide and 8 mm long[135] and it can be patterned at the bottom of a microfluidic channel at the location(s) where fluid flow need to be measured. A change of the stray field of the magnetic micropillars is detected by the GMI sensor in the presence of fluid flow. The change of the stray field, which is a function of the micropillar displacement, translates to an impedance change of the GMI sensor.

The relation between the displacement of the pillar and the force exerted on the area of the pillar facing the flow is given by the displacement-force relationship of an elastic cylindrical beam (**Equation 5.7**). The sensitivity and the resolution of the flow sensor depend on the diameter of the micropillar as well as the configuration of the pillar array.[135,136] Given the low pitch value of the magnetic thiol-ene micropillar array shown in **Figure 5.9** and the possibility to tune the elasticity of the individual pillars, different configurations of the flow sensors can be easily implemented to target specific operation range and sensor performance.

6. Conclusion and Outlook

This thesis describes fabrication, characterization and application of superhydrophobic surfaces. Emphasis has been directed towards accurate characterization of non-wettability and fabrication of cilia-inspired responsive superhydrophobic surfaces.

Publication I investigates friction and wetting transition of aqueous ferrofluid droplets on superhydrophobic surfaces using magnetic field-induced oscillations. Variations in properties that directly influence the degree of surface superhydrophobicity were probed by implementing free-decay droplet oscillations on micropillared superhydrophobic surfaces. Compared with the standard characterization method of contact angle goniometry, minor variations in pattern density were easily revealed by the oscillating droplet tribometer. On each surface, distinct values of contact angle hysteresis force and viscous dissipation coefficient were extracted from the droplet oscillation profiles. This characterization technique allowed surfaces of seemingly comparable advancing and receding contact angles to be distinguished. Through a systematic study, it has been identified that the solid-liquid fraction range within which droplet oscillations are feasible is between 0.78 % and 3.14 % for square array of 10 μm diameter pillars of circular cross-section.

The stability of Cassie state of a droplet in motion was investigated by relating CW transition to the solid-liquid fraction and the magnetic field-induced normal force. The transition was found to occur at lower pressure for a droplet during oscillation on micropillared silicon surfaces treated with FDTS, compared with a static droplet on the same surfaces.

Oscillating droplet tribometer was also proven to be an effective technique to probe the effect of different surface treatment procedures applied on similar silicon micropillared surfaces. This was indicated in this thesis by comparing the measured contact angle hysteresis force from droplet oscillations performed on identical miropillared surfaces each was subjected to distinct surface modification procedure. Coating with FDTS yielded the lowest contact angle hysteresis force compared with surface treatment with ODTS, and Teflon®-like fluorocarbon thin film coating.

This technique can be applied to reveal the influence of packing density, alkyl chain length and branching of the self-assembled monolayers on the measured contact angle hysteresis force and the robustness of Cassie state. This allows distinction between the superhydrophobicity of different surfaces, each of which treated with a unique chemical. Attempts to perform droplet oscillation experiments on micropillared surfaces treated with SAMs of short alkyl chain

lengths like trichloro(3,3,3-trifluoropropyl)silane and butyltrichlorosilane have failed due to CW transition of the droplet during the oscillation. In this case, surfaces consisting of cylindrical micropillars cannot sustain dynamic water-based ferrofluid droplets in Cassie state. Micropillars with double re-entrant structures can provide stability against the wetting transition thus droplet oscillations on such surfaces can be conducted even if they are treated with SAMs of short alkyl chain lengths.

Characterization of superoleophobic surfaces can also benefit from the high sensitivity of the oscillating droplet tribometer. In this case, oil-based ferrofluid can be synthesized to be implemented in the oscillation measurements. Factors that are essential for the superoleophobicity include surface energy, the re-entrant shape of the micro-and nanostructures, surface roughness and surface tension of liquids. The effect of these parameters on friction and wetting transition of oil-based ferrofluid droplets can be revealed by employing droplet oscillations.

Publication II introduced a facile fabrication process for synthesizing cilia-inspired, slippery and magnetically responsive surfaces. Droplet manipulation was demonstrated at the sub-mm scale aided by negligible retention force of the surface. This allowed controlled droplet motion along different directions. Moreover, directional transport of polyethylene microbeads was demonstrated to simulate clearance of solid contaminants. The demonstrated fabrication technique allows rapid prototyping of cilia-inspired and magnetically responsive surfaces. Further studies should be centered on fabricating microfluidic systems with integrated array of magnetic micropillars to enable on-demand fluid propulsion and mixing.

In publication III, a new type of cilia-inspired magnetic micropillars based on thiol-ene is introduced. Thiol-ene as the material of choice for constructing magnetically responsive superhydrophobic surface enabled tuning of both surface and elastic properties. Tuning the elastic properties of the magnetic micropillars was achieved by controlling the crosslinking density of the monomers. This allowed fabrication of flexible micropillars (Diallyl:Trithiol) and stiff micropillars (Triallyl:Trithiol). Smaller incremental change in the mechanical properties of the magnetic pillars was achieved by tuning the off-stoichiometric ratio of the thiol-ene mixture. Variations in the mechanical properties were probed successfully using local actuation of individual pillars by an electromagnetic needle. This was accomplished by relating thiol-ene chemistry to the free-end displacement of the magnetic micropillars at a given value of the supplied current to the needle. Moreover, the effect of thiol-ene chemistry on the responsiveness of the pillars was also revealed by the local actuation using the electromagnetic needle.

Surface topography modification of the magnetic thiol-ene micropillars was accomplished by UV grafting of colloidal polyvinyltrimethoxysilane micro- and nanoparticles onto the surface of the pillars. Decorating the pillars provides mechanical stability without compromising the fast and powerful actuation capabilities. This feature allows actuation of high aspect ratio pillars in air. To this day, cilia-inspired magnetic micropillars of high aspect ratio relied on

critical point drying to enable functionality in air and the stability issue has not been addressed. Furthermore, superhydrophobicity or superhydrophilicity can be gained by UV grafting of hydrophobic or hydrophilic self-assembled monolayers.

The fast responsiveness of the pillars, enhanced stability, tunable surface and mechanical properties are essential features for many practical applications. Flow sensor integrated in microfluidic system and miniaturized tactile sensor capable of measuring mechanical deformations are among applications that can be achieved by integrating an array of thiol-ene micropillars on top of a giant magneto impedance sensing element.

Transparency combined with enhanced stability and superhydrophobicity can promote the use of thiol-ene magnetic micropillars as a microfluidic elastometer for blood coagulation monitoring. In this application, blood samples are in direct contact with the micropillar array. Coagulation of blood is correlated to the applied magnetic field, which magnitude must increase in order to induce a constant deflection of the pillars during the coagulation.

References

1. Barthlott, W. & Neinhuis, C. Purity of the sacred lotus, or escape from contamination in biological surfaces. *Planta* **202**, 1–8 (1997).

2. Bixler, G. D. & Bhushan, B. Fluid drag reduction and efficient self-cleaning with rice leaf and butterfly wing bioinspired surfaces. *Nanoscale* **5**, 7685–7710 (2013).

3. Choi, C. H., Ulmanella, U., Kim, J., Ho, C. M. & Kim, C. J. Effective slip and friction reduction in nanograted superhydrophobic microchannels. *Phys. Fluids* **18**, 087105 (2006).

4. Lee, C. & Kim, C. J. Maximizing the giant liquid slip on superhydrophobic microstructures by nanostructuring their sidewalls. *Langmuir* **25**, 12812–12818 (2009).

5. Kirschner, C. M. & Brennan, A. B. Bio-Inspired Antifouling Strategies. *Annu. Rev. Mater. Res.* **42**, 211-229 (2012).

6. Zhang, P., Lin, L., Zang, D., Guo, X. & Liu, M. Designing Bioinspired Anti-Biofouling Surfaces based on a Superwettability Strategy. *Small* **13**, 1503334 (2016).

7. Zhao, J., Song, L., Yin, J. & Ming, W. Anti-Bioadhesion on Hierarchically Structured, Superhydrophobic Surfaces. *Chem. Commun.* **49**, 9191–9193 (2013).

8. Liu, T. Yin, B., He, T., Guo, N., Dong, L. & Yin, Y. Complementary effects of nanosilver and superhydrophobic coatings on the prevention of marine bacterial adhesion. *ACS Appl. Mater. Interfaces* **4**, 4683–4690 (2012).

9. Fürstner, R., Barthlott, W., Neinhuis, C. & Walzel, P. Wetting and self-cleaning properties of artificial superhydrophobic surfaces. *Langmuir* **21**, 956–961 (2005).

10. Sun, T., Feng, L., Gao, X. & Jiang, L. Bioinspired surfaces with special wettability. *Accounts of Chemical Research* **38**, 644–652 (2005).

11. Celia, E., Darmanin, T., Taffin de Givenchy, E., Amigoni, S. & Guittard, F. Recent advances in designing superhydrophobic surfaces. *Journal of Colloid and Interface Science* **402**, 1–18 (2013).

12. Bixler, G. D. & Bhushan, B. Rice-and butterfly-wing effect inspired self-cleaning and low drag micro/nanopatterned surfaces in water, oil, and air flow. *Nanoscale* **6**, 76–96 (2014).

13. Neinhuis, C. & Barthlott, W. Characterization and distribution of water-repellent, self-cleaning plant surfaces. *Ann. Bot.* **79**, 667–677 (1997).

14. Ensikat, H. J., Mayser, M. & Barthlott, W. Superhydrophobic and adhesive properties of surfaces: Testing the quality by an elaborated scanning electron microscopy method. *Langmuir* **28**, 14338–14346 (2012).

15. P. Feynman, R. There is plenty of room at the bottom. *Engineering and Science* **23**, 22–36 (1960).

16. Singh, T., Rangarajan, S., John, D., Schreiber, R., Oliver, S., Seahra R. & Schaefer, A. Zen 2: The AMD 7nm Energy-Efficient High-Performance x86-64 Microprocessor Core. in *Digest of Technical Papers - IEEE International Solid-State Circuits Conference- (ISSCC)*, San Francisco, CA, USA, 42–44 (2020).

17. Callies, M. & Quéré, D. On water repellency. *Soft Matter* **1**, 55–61 (2005).

18. Bhushan, B. & Nosonovsky, M. The rose petal effect and the modes of superhydrophobicity. *Phil. Trans. R. Soc. A.* **368**, 4713–4728 (2010).

19. Wang, J., Yang, Q., Wang, M., Wang, C. & Jiang, L. Rose petals with a novel and steady air bubble pinning effect in aqueous media. *Soft Matter* **8**, 2261–2266 (2012).

20. Sun, M., Watson, G. S., Zheng, Y., Watson, J. A. & Liang, A. Wetting properties on nanostructured surfaces of cicada wings. *J. Exp. Biol.* **212**, 3148–3155 (2009).

21. Hong, S. H., Hwang, J. & Lee, H. Replication of cicada wing's nano-patterns by hot embossing and UV nanoimprinting. *Nanotechnology* **20**, 385303 (2009).

22. Ivanova, E. P., Hasan, J., Webb, H. K., Truong, V. K., Watson, G. S., Watson, J. A., Baulin, V. A., Pogodin, S., Wang, J. Y., Tobin, M. J., Löbbe, C. & Crawford, R. J. Natural bactericidal surfaces: Mechanical rupture of pseudomonas aeruginosa cells by cicada wings. *Small* **8**, 2489–2494 (2012).

23. Solga, A., Cerman, Z., Striffler, B. F., Spaeth, M. & Barthlott, W. The dream of staying clean: Lotus and biomimetic surfaces. *Bioinsp. Biomim* **2**, 126–134 (2007).

24. Hasan, J., Crawford, R. J. & Ivanova, E. P. Antibacterial surfaces: The quest for a new generation of biomaterials. *Trends Biotechnol.* **31**, 295–304 (2013).

25. Dou, X. Q., Zhang, D., Feng, C. & Jiang, L. Bioinspired Hierarchical Surface Structures with Tunable Wettability for Regulating Bacteria Adhesion. *ACS Nano* **9**, 10664–10672 (2015).

26. Jokinen, V., Kankuri, E., Hoshian, S., Franssila, S. & Ras, R. H. A. Superhydrophobic Blood-Repellent Surfaces. *Adv. Mater.* **30**, 1705104 (2018).

27. Bixler, G. D. & Bhushan, B. Biofouling: lessons from nature. *Philos. Trans. R. Soc. A.* **370**, 2381–2417 (2012).

28. Tian, Y., Su, B. & Jiang, L. Interfacial Material System Exhibiting Superwettability. *Adv. Mater.* **26**, 6872–6897 (2014).

29. Liu, H., Wang Y., Huang, J., Chen, Z., Chen, G. & Lai, Y. Bioinspired Surfaces with Superamphiphobic Properties: Concepts, Synthesis, and Applications. *Adv. Funct. Mater.* **28**, 1707415 (2018).

30. Wang, S., Liu, K., Yao, X. & Jiang, L. Bioinspired surfaces with superwettability: New insight on theory, design, and applications. *Chem. Rev.* **115**, 8230–8293 (2015).

31. Ju, J., Bai, H., Zheng, Y., Zhao, T., Fang, R. & Jiang, L. A multi-structural and multi-functional integrated fog collection system in cactus. *Nature communications* **3**, 1247 (2012).

32. Cao, M., Ju, J., Li, K., Dou, S., Liu K. & Jiang, L. Facile and large-scale fabrication of a cactus-inspired continuous fog collector. *Adv. Funct. Mater.* **24**, 3235–3240 (2014).

33. Bixler, G. D. & Bhushan, B. Fluid drag reduction with shark-skin riblet inspired microstructured surfaces. *Adv. Funct. Mater.* **23**, 4507–4528 (2013).

34. Krieger, K. Do pool sharks swim faster? *Science* **305**, 636–637 (2004).

35. Rahmawan, Y., Xu, L. & Yang, S. Self-assembly of nanostructures towards transparent, superhydrophobic surfaces. *J. Mater. Chem. A* **1**, 2955–2969 (2013).

36. Feng, J., Tuominen, M. T. & Rothstein, J. P. Hierarchical superhydrophobic surfaces fabricated by dual-scale electron-beam-lithography with well-ordered secondary nanostructures. *Adv. Funct. Mater.* **21**, 3715–3722 (2011).

37. Hoshian, S., Jokinen, V., Hjort, K., Ras, R. H. A. & Franssila, S. Amplified and

Localized Photoswitching of TiO_2 by Micro- and Nanostructuring. *ACS Appl. Mater. Interfaces* **7**, 15593–15599 (2015).

38. Liu, X., Coxon P. R., Peters, M., Hoex, B., Cole, J. M., & Fray, D. J. Black silicon: Fabrication methods, properties and solar energy applications. *Energy Environ. Sci.* **7**, 3223–3263 (2014).

39. Huang, S., Li, J., Liu, L., Zhou, L. & Tian, X. Lossless Fast Drop Self-Transport on Anisotropic Omniphobic Surfaces: Origin and Elimination of Microscopic Liquid Residue. *Adv. Mater.* **31**, 1901417 (2019).

40. Lv, J., Song, Y., Jiang, L. & Wang, J. Bio-Inspired Strategies for Anti-Icing. **8**, 3152–3169 (2014).

41. Zhang, J. & Seeger, S. Polyester materials with superwetting silicone nanofilaments for oil/water separation and selective oil absorption. *Adv. Funct. Mater.* **21**, 4699–4704 (2011).

42. Chen, F., Lu, Y., Liu, X., Song, J., He, G., Tiwari, M. K., Carmalt, C.J. & Parkin, I. P. Table Salt as a Template to Prepare Reusable Porous PVDF–MWCNT Foam for Separation of Immiscible Oils/Organic Solvents and Corrosive Aqueous Solutions. *Adv. Funct. Mater.* **27**, 1702926 (2017).

43. Liu, T. & Kim, C. J. Turning a Surface Superrepellent Even to Completely Wetting Liquids. *Science* **346**, 1096–1100 (2014).

44. Nosonovsky, M. & Bhushan, B. Why re-entrant surface topography is needed for robust oleophobicity. *Phil. Trans. R. Soc. A.* **374**, 20160185 (2016).

45. Das, R., Ahmad, Z., Nauruzbayeva, J. & Mishra, H. Biomimetic Coating-free Superomniphobicity. *Sci. Rep.* **10**, 7934 (2020).

46. Liu, X., Gu, H., Ding, H., Du, X., He, Z., Sun, L., Liao, J., Xiao, P. & Gu, Z. Programmable Liquid Adhesion on Bio-Inspired Re-Entrant Structures. *Small* **15**, 1902360 (2019).

47. Liu, X, Gu, H., Wang, M., Du, X., Gao, B., Elbaz, A., Sun, L., Liao, J., Xiao, P. & Gu, Z. 3D Printing of Bioinspired Liquid Superrepellent Structures. *Adv. Mater.* **30**, 1800103 (2018).

48. Hoshian, S., Kankuri, E., Ras, R. H. A., Franssila, S. & Jokinen, V. Water and Blood Repellent Flexible Tubes. *Sci. Rep.* **7**, 16019 (2017).

49. Wang, D., Sun, Q., Hokkanen, M. J., Zhang, C., Lin, F. Y., Liu, Q., Zhu, S. P., Zhou, T., Chang, Q., He, B., Zhou, Q., Chen, L., Wang, Z., Ras, R. H. A. & Deng, X., Design of robust superhydrophobic surfaces. *Nature* **582**, 55–59 (2020).

50. Bruus, H. Theoretical Microfluids. *Oxford Master Series in Condensed Matter Physics* (2008).

51. Quéré, D. Wetting and Roughness. *Annu. Rev. Mater. Res.* **38**, 71–99 (2008).

52. de Gennes, P. G. Wetting: statics and dynamics. *Rev. Mod. Phys.* **57**, 827–863 (1985).

53. Shirtcliffe, N. J., McHale, G., Atherton, S. & Newton, M. I. An introduction to superhydrophobicity. *Adv. Colloid Interface Sci.* **161**, 124–138 (2010).

54. Thomas, Y. An Essay on the Cohesion of Fluids. *Phil. Trans. R. Soc.* **95**, 65–87 (1805).

55. Marmur, A., Volpe, C. D., Siboni, S., Amirfazli, A. & Drelich, J. W. Contact angles and wettability: Towards common and accurate terminology. *Surf. Innov.* **5**, 3–8 (2017).

56. Drelich, J. & Marmur, A. Physics and applications of superhydrophobic and superhydrophilic surfaces and coatings. *Surf. Innov.* **2**, 211–227 (2014).

57. Roura, P. & Fort, J. Local thermodynamic derivation of Young's equation. *J. Colloid Interface Sci.* **272**, 420–429 (2004).

58. Quéré, D. Non-sticking drops. *Reports Prog. Phys.* **68**, 2495–2532 (2005).

59. Bico, J., Thiele, U. & Quéré, D. Wetting of textured surfaces. *Colloids and Surfaces A: Physicochemical and Engineering Aspects* **206**, 41–46 (2002).

60. Wenzel, R. N. Resistance of solid surfaces to wetting by water. *Ind. Eng. Chem.* **28**, 988-994 (1936).

61. Mongkhontreerat, S., Öberga, K., Erixona, L., Löwenhielmb, P., Hulta, A. & Malkoch, M. UV initiated thiol-ene chemistry: A facile and modular synthetic methodology for the construction of functional 3D networks with tunable properties. *J. Mater. Chem. A* **1**, 13732–13737 (2013).

62. Dorrer, C. & Rühe, J. Condensation and wetting transitions on microstructured ultrahydrophobic surfaces. *Langmuir* **23**, 3820–3824 (2007).

63. Sarkar, A. & Kietzig, A. M. General equation of wettability: A tool to calculate the contact angle for a rough surface. *Chem. Phys. Lett.* **574**, 106–111 (2013).

64. Nosonovsky, M. & Ramachandran, R. Geometric interpretation of surface tension equilibrium in superhydrophobic systems. *Entropy* **17**, 4684–4700 (2015).

65. Tuteja, A., Choi, W., Ma, M., Mabry, J. M., Mazzella, S. A., Rutledge, G. C., McKinley, G. H. & Cohen, R. E. Designing superoleophobic surfaces. *Science* **318**, 1618–1622 (2007).

66. Cassie, A. B. D. & Baxter, S. Wettability of porous surfaces. *Trans. Faraday Soc.* **40**, 546–551 (1944).

67. Cassie, A. B. D. Contact angles. *Discuss. Faraday Soc.* **3**, 11–16 (1948).

68. Marmur, A. Soft contact: Measurement and interpretation of contact angles. *Soft Matter* **2**, 12–17 (2006).

69. Marmur, A. Solid-Surface Characterization by Wetting. *Annu. Rev. Mater. Res* **39**, 473–89 (2009).

70. Marmur, A. Thermodynamic aspects of contact angle hysteresis. *Adv. Colloid Interface Sci.* **50**, 121–141 (1994).

71. Lafuma, A. & Quéré, D. Superhydrophobic states. *Nat. Mater.* **2**, 457–460 (2003).

72. Milne, A. J. B. & Amirfazli, A. The Cassie equation: How it is meant to be used. *adv. Colloid Interface Sci.* **170**, 48–55 (2012).

73. Yoshimitsu, Z., Nakajima, A., Watanabe, T. & Hashimoto, K. Effects of surface structure on the hydrophobicity and sliding behavior of water droplets. *Langmuir* **18**, 5818–5822 (2002).

74. He, B., Patankar, N. A. & Lee, J. Multiple equilibrium droplet shapes and design criterion for rough hydrophobic surfaces. *Langmuir* **19**, 4999-5003 (2003).

75. Reyssat, M., Yeomans, J. M. & Quéré, D. Impalement of fakir drops. *EPL* **81**, 26006 (2008).

76. Schellenberger, F., Encinas, N., Vollmer, D. & Butt, H. J. How Water Advances on Superhydrophobic Surfaces. *Phys. Rev. Lett.* **116**, 096101 (2016).

77. Park, C. I., Jeong, H. E., Lee, S. H., Cho, H. S. & Suh, K. Y. Wetting transition and optimal design for microstructured surfaces with hydrophobic and hydrophilic materials. *J. Colloid Interface Sci.* **336**, 298–303 (2009).

78. Bormashenko, E., Pogreb, R., Whyman, G., Bormashenko, Y. & Erlich, M. Vibration-induced Cassie-Wenzel wetting transition on rough surfaces. *Appl. Phys. Lett.* **90**, 201917 (2007).

79. Lee, C., Nam, Y., Lastakowski, H., Janet, I. H., Shin, S., Biance, A. L., Pirat, C., Kim, C. J. & Ybert, C. Two types of Cassie-to-Wenzel wetting transitions on superhydrophobic surfaces during drop impact. *Soft Matter* **11**, 4592–4599.

80. Zheng, Q. S., Yu, Y. & Zhao, Z. H. Effects of hydraulic pressure on the stability

and transition of wetting modes of superhydrophobic surfaces. *Langmuir* **21**, 12207–12212 (2005).

81. Ishino, C., Okumura, K. & Quéré, D. Wetting transitions on rough surfaces. *EPL* **68**, 419 (2004).

82. Patankar, N. A. Transition between superhydrophobic states on rough surfaces. *Langmuir* **20**, 7097–7102 (2004).

83. Barbulovic-Nad, I., Yang, H., Park, P. S. & Wheeler, A. R. Digital microfluidics for cell-based assays. *Lab Chip* **8**, 519–526 (2008).

84. Wang, K. & Fatoyinbo, H. O. Microfluidics in Detection Science. *RSC Detection Science* (Eds: Fatoyinbo, H. O. & Labeed, F. H.), 84–135 (2015).

85. Lima, A. C. & Mano, J. F. Micro/nano-structured superhydrophobic surfaces in the biomedical field: Part II: Applications overview. *Nanomedicine* **10**, 271–297 (2015).

86. Golovin, K., Kobaku, S. P. R., Lee, D. H., DiLoreto, E. T., Mabry, J. M. & Tuteja, A. Designing durable icephobic surfaces. *Sci. Adv.* **2**, e1501496 (2016).

87. Kreder, M. J., Alvarenga, J., Kim, P. & Aizenberg, J. Design of anti-icing surfaces: Smooth, textured or slippery? *Nature Reviews Materials* **1**, 15003 (2016).

88. Extrand, C. W. & Gent, A. N. Retention of liquid drops by solid surfaces. *J. Colloid Interface Sci.* **138**, 431–442 (1990).

89. ElSherbini, A. I. & Jacobi, A. M. Retention forces and contact angles for critical liquid drops on non-horizontal surfaces. *J. Colloid Interface Sci.* **299**, 841–849 (2006).

90. Pilat, D. W., Papadopoulos, P., Schäffel, D., Vollmer, D., Berger, R. & Butt, H. J. Dynamic measurement of the force required to move a liquid drop on a solid surface. *Langmuir* **28**, 16812–16820 (2012).

91. Pierce, E., Carmona, F. J. & Amirfazli, A. Understanding of sliding and contact angle results in tilted plate experiments. *Colloids Surfaces A Physicochem. Eng. Asp.* **323**, 73–82 (2008).

92. Krasovitski, B. & Marmur, A. Drops down the hill: Theoretical study of limiting contact angles and the hysteresis range on a tilted plate. *Langmuir* **21**, 3881–3885 (2005).

93. Keng, P. Y., Chen, S., Ding. H., Sadeghi, S., Shah, G. J., Dooraghi, A., Phelps, M. E. Satyamurthy, N., Chatziioannou, A. F., Kim, C. J. & van Dam R. M. Micro-chemical synthesis of molecular probes on an electronic microfluidic device. *PNAS* **109**, 690–695 (2012).

94. Shastry, A., Case, M. J. & Böhringer, K. F. Directing droplets using microstructured surfaces. *Langmuir* **22**, 6161–6167 (2006).

95. Li, J., Tian, X., Perros, A. P., Franssila, S. & Jokinen, V. Self-Propelling and Positioning of Droplets Using Continuous Topography Gradient Surface. *Adv. Mater. Interfaces* **1**, 1400001 (2014).

96. Li, J., Qin, Q. H., Shah, A., Ras, R. H. A., Tian, X. & Jokinen, V. Oil droplet self-transportation on oleophobic surfaces. *Sci. Adv.* **2**, e1600148 (2016).

97. Zhou, Y., Huang, S. & Tian, X. Magnetoresponsive Surfaces for Manipulation of Nonmagnetic Liquids: Design and Applications. *Adv. Funct. Mater.* **30**, 1906507 (2019).

98. Korhonen, J. T., Huhtamäki, T., Ikkala, O. & Ras, R. H. A. Reliable measurement of the receding contact angle. *Langmuir* **29**, 3858–3863 (2013).

99. Huhtamäki, T., Tian, X., Korhonen, J. T. & Ras, R. H. A. Surface-wetting characterization using contact-angle measurements. *Nat. Protoc.* **13**, 1521–1538 (2018).

100. Kung, C. H., Sow, P. K., Zahiri, B. & Mérida, W. Assessment and Interpretation of Surface Wettability Based on Sessile Droplet Contact Angle Measurement: Challenges and Opportunities. *Adv. Mater. Interfaces* **6**, 1900839 (2019).

101. Timonen, J. V. I., Latikka, M., Ikkala, O. & Ras, R. H. A. Free-decay and resonant methods for investigating the fundamental limit of superhydrophobicity. *Nat. Commun.* **4**, 2398 (2013).

102. Liimatainen, V., Vuckovac, M., Jokinen, V., Sariola, V., Hokkanen, M. J., Zhou, Q., & Ras, R. H. A. Mapping microscale wetting variations on biological and synthetic water-repellent surfaces. *Nat. Commun.* **8**, 1798 (2017).

103. Daniel, D., Lay, C. L., Sng, A., Lee, C. J. J., Neo, D. C. J., Ling, X. Y. & Tomczak, N. Mapping micrometer-scale wetting properties of superhydrophobic surfaces. *PNAS* **116**, 25008–25012 (2019).

104. Butt, H. J., Roisman, I. V., Brinkmann, M., Papadopoulos, P., Vollme, D. & Semprebon, C. Characterization of super liquid-repellent surfaces. *Current Opinion in Colloid and Interface Science* **19**, 343–354 (2014).

105. Backholm, M., Molpeceres, D., Vuckovac, M., Nurmi, H., Hokkanen, M. J., Jokinen, V., Timonen, J. V. I & Ras R. H. A. Water droplet friction and rolling dynamics on superhydrophobic surfaces. *Commun. Mater.* **1**, 64 (2020).

106. Mannetje, D., Banpurkar, A., Koppelman, H., Duits, M. H. G., van den Ende, D. & Mugele, F. Electrically tunable wetting defects characterized by a simple capillary force sensor. *Langmuir* **29**, 9944–9949 (2013).

107. Gao, N., Geyer, F., Pilat, D. W., Wooh, S., Vollmer, D., Butt, H. J. & Berger, R. How drops start sliding over solid surfaces. *Nat. Phys.* **14**, 191–196 (2018).

108. Liu, K., Vuckovac, M., Latikka, M. & Ras, R. H. A. Improving surface-wetting characterization. *Science* **363**, 1147–1148 (2019).

109. A. Ricchiuto and A. Tozzi. Motion of a harmonic oscillator with sliding and viscous friction. *Am. J. Phys.* **50**, 176–179 (1982).

110. Chen, R., Kim, H., McIntyre, P. C., Porter, D. W. & Bent, S. F. Achieving area-selective atomic layer deposition on patterned substrates by selective surface modification. *Appl. Phys. Lett* **86**, 191910 (2005).

111. Dong, J., Wang, A., Ng, K. Y. S. & Mao, G. Self-assembly of octadecyltrichlorosilane monolayers on silicon-based substrates by chemical vapor deposition. *Thin Solid Films* **515**, 2116–2122 (2006).

112. Zhuang, Y. X., Hansen, O., Knieling, T., Wang, C., Rombach, P., Lang, W., Benecke, W., Kehlenbeck, M. & Koblitz, J. Thermal stability of vapor phase deposited self-assembled monolayers for MEMS anti-stiction. *J. Micromech. Microeng.* **16**, 2259–2264 (2006).

113. Knieling, T., Lang, W. & Benecke, W. Gas phase hydrophobisation of MEMS silicon structures with self-assembling monolayers for avoiding in-use sticking. *Sensors Actuators, B Chem.* **126**, 13–17(2007).

114. Arkles, B. Hydrophobicity, hydrophilicity and silanes. *Paint Coatings Ind.* **22**, 114–135 (2006).

115. Massart, R. Preparation of aqueous magnetic liquids in alkaline and acidic media. *IEEE Trans. Magn.* **17**, 1247–1248 (1981).

116. Sahoo, Y., Goodarzi, A., Swihart, M. T., Ohulchanskyy, T. Y., Kaur, N., Furlani, E. P. & Prasad, P. N. Aqueous ferrofluid of magnetite nanoparticles: Fluorescence labeling and magnetophoretic control. *J. Phys. Chem. B* **109**, 3879–3885 (2005).

117. Einstein, A. A new determination of molecular dimensions. *Ann. Phys.* **19**, 289 (1906).

118. Hall, W. F. & Busenberg, S. N. Viscosity of magnetic suspensions. *J. Chem.*

Phys. (1969).

119. Mahadevan, L. & Pomeau, Y. Rolling droplets. *Phys. Fluids* **11**, 2449–2453 (1999).

120. Smith, A. F. W., Mahelona, K. & Hendy, S. C. Rolling and slipping of droplets on superhydrophobic surfaces. *Phys. Rev. E* **98**, 033113 (2018).

121. Annavarapu, R. K., Kim, S., Wang, M., Hart, A. J. & Sojoudi, H. Explaining Evaporation-Triggered Wetting Transition Using Local Force Balance Model and Contact Line-Fraction. *Sci. Rep.* **9**, 405 (2019).

122. Schrader, M. E. Young-Dupre Revisited. *Langmuir* **11**, 3585–3589 (1995).

123. Pease, D. C. The significance of the contact angle in relation to the solid surface. *J. Phys. Chem.* **49**, 107–110 (1945).

124. Erpul, G., Norton, L. D. & Gabriels, D. Raindrop-induced and wind-driven soil particle transport. *Catena* **47**, 227–243 (2002).

125. Shah, A. S., Yehuda, B. S., Moninger, T. O., Kline, J. N. & Welsh, M. J. Motile cilia of human airway epithelia are chemosensory. *Science* **325**, 1131–1134 (2009).

126. Button, B., Cai, L. H., Ehre, C., Kesimer, M., Hill, D. B., Sheehan, J. K., Boucher, R. C. & Michael Rubinstein, M. A periciliary brush promotes the lung health by separating the mucus layer from airway epithelia. *Science* **337**, 937–941 (2012).

127. Satir, P. & Christensen, S. T. Overview of Structure and Function of Mammalian Cilia. *Annu. Rev. Physiol.* **69**, 377–400 (2006).

128. Singla, V. & Reiter, J. F. The primary cilium as the cell's antenna: Signaling at a sensory organelle. *Science* **313**, 629–633 (2006).

129. Chen, C. M. & Yang, S. Directed water shedding on high-aspect-ratio shape memory polymer micropillar arrays. *Adv. Mater.* **26**, 1283–1288 (2014).

130. Shields, A. R., Fiser, B. L., Evans, B. A., Falvo, M. R., Washburn, S. & Superfine, R. Biomimetic cilia arrays generate simultaneous pumping and mixing regimes. *PNAS* **107**, 15670–15675 (2010).

131. Wang, Y., Gao, Y., Wyss, H., Anderson, P. & den Toonder, J. Out of the cleanroom, self-assembled magnetic artificial cilia. *Lab Chip* **13**, 3360–3366 (2013).

132. Drotlef, D. M., Blümler, P., Papadopoulos, P. & Del Campo, A. Magnetically actuated micropatterns for switchable wettability. *ACS Appl. Mater. Interfaces* **6**, 8702–8707 (2014).

133. Drotlef, D. M., Blümler, P. & Del Campo, A. Magnetically actuated patterns for bioinspired reversible adhesion (dry and wet). *Adv. Mater.* **26**, 775–779 (2014).

134. den Toonder, J., Bos, F., Broer, D., Filippini, L., Gillies, M., de Goede, J., Mol, T., Reijme, M., Talen, W., Wilderbeek, H., Khatavkar, V. & Anderson, P. Artificial cilia for active micro-fluidic mixing. *Lab Chip* **8**, 533–541 (2008).

135. Alfadhel, A., Li, B., Zaher, A., Yassine, O. & Kosel, J. A magnetic nanocomposite for biomimetic flow sensing. *Lab Chip* **14**, 4362–4369 (2014).

136. Alfadhel, A. & Kosel, J. Magnetic Nanocomposite Cilia Tactile Sensor. *Adv. Mater.* **27**, 7888–7892 (2015).

137. Zhou, Y., Huang, S. & Tian, X. Magnetoresponsive Surfaces for Manipulation of Nonmagnetic Liquids: Design and Applications. *Adv. Funct. Mater.* **30**, 1906507 (2020).

138. Yang, Z., Park, J. K. & Kim S. Magnetically Responsive Elastomer-Silicon Hybrid Surfaces for Fluid and Light manipulation. *Small* **14**, 1702839 (2018).

139. Gillies, A. G., Kwak, J. & Fearing, R. S. Controllable particle adhesion with a

magnetically actuated synthetic gecko adhesive. *Adv. Funct. Mater.* **23**, 3256–3261 (2013).

140. Sniadecki, N. J., Anguelouch, A., Yang, M. T., Lamb, C. M., Liu, Z., Kirschner, S. B., Liu, Y., Reich, D. H. & Chen, C. S. Magnetic microposts as an approach to apply forces to living cells. *PNAS* **104**, 14553–14558 (2007).

141. Cheng, Q., Sun, Z., Meininger, G. & Almasri, M. PDMS elastic micropost arrays for studying vascular smooth muscle cells. *Sensors Actuators, B Chem.* **188**, 1055–1063 (2013).

142. McDonald, J. C. & Whitesides, G. M. Poly (dimethylsiloxane) as a Material for Fabricating Microfluidic Devices. *Acc. Chem. Res.* **35**, 491–99 (2002).

143. Ng, J. M. K., Gitlin, I., Stroock, A. D. & Whitesides, G. M. Components for integrated poly(dimethylsiloxane) microfluidic systems. *Electrophoresis* **23**, 3461–3473 (2002).

144. Lee, J. N., Park, C. & Whitesides, G. M. Solvent Compatibility of Poly(dimethylsiloxane)-Based Microfluidic Devices. *Anal. Chem.* **75**, 6544–6554 (2003).

145. Good, B. T., Reddy, S., Davis, R. H. & Bowman, C. N. Tailorable low modulus, reversibly deformable elastomeric thiol-ene materials for microfluidic applications. *Sensors Actuators, B Chem.* **120**, 473–480 (2007).

146. Carlborg, C. F., Haraldsson, T., Öberg, K., Malkoch, M. & van der Wijngaart, W. Beyond PDMS: off-stoichiometry thiol–ene (OSTE) based soft lithography for rapid prototyping of microfluidic devices. *Lab Chip* **11**, 3136–3147 (2011).

147. Carlborg, C. F., Vastesson, A., Liu, Y., van der Wijngaart, W., Johansson, M. & Haraldsson, T. Functional off-stoichiometry thiol-ene-epoxy thermosets featuring temporally controlled curing stages via an UV/UV dual cure process. *J. Polym. Sci. Part A Polym. Chem.* **52**, 2604–2615 (2014).

148. Hansson, J., Yasuga, H., Haraldsson, T. & van der Wijngaart, W. Synthetic microfluidic paper: high surface area and high porosity polymer micropillar arrays. *Lab Chip* **16**, 298–304 (2016).

149. Vitale, A., Hennessy, M. G., Matar, O. K. & Cabral, J. T. A Unified Approach for Patterning via Frontal Photopolymerization. *Adv. Mater.* **27**, 6118–6124 (2015).

150. Huang, Y., Stogin, B. B., Sun, N., Wang, J., Yang, S. & Wong T. S. A Switchable Cross-Species Liquid Repellent Surfaces. *Adv. Mater.* **29**, 1604641 (2017).

151. Ben, S., Zhou, T., Ma, H., Yao, J., Ning, Y., Tian, D., Liu, K. & Jiang, L. Multifunctional Magnetocontrollable Superwettable-Microcilia Surface for Directional Droplet Manipulation. *Adv. Sci.* **6**, 1900834 (2019).

152. Yang, C., Zhang, Z. & Li, G. Programmable droplet manipulation by combining a superhydrophobic magnetic film and an electromagnetic pillar array. *Sensors Actuators, B Chem.* **262**, 892–901 (2018).

153. Peng, Y., He, Y., Yang, S., Ben, S., Cao, M., Li, K., Liu, K. & Jiang, L. Magnetically induced fog harvesting via flexible conical arrays. *Adv. Funct. Mater.* **25**, 5967–5971 (2015).

154. Judith, R. M., Fisher, J. K., Spero, R. C., Fiser, B. L., Turner, A., Oberhardt, B., Taylor, R. M., Falvoa, M. R. & Superfine, R. Micro-elastometry on whole blood clots using actuated surface-attached posts (ASAPs). *Lab Chip* **15**, 1385–1393 (2015).

155. Timonen, J. V. I., Johans, C., Kontturi, K., Walther, A., Ikkala, O. & Ras, R. H. A. A facile template-free approach to magnetodriven, multifunctional artificial cilia. *ACS Appl. Mater. Interfaces* **2**, 2226–2230 (2010).

156. Kim, J. H., Kang, S. M., Lee, B. J., Ko, H., Bae, W. G., Suh, K. Y., Kwak, M. K. &

Jeong, H E. Remote Manipulation of Droplets on a Flexible Magnetically Responsive Film. *Sci. Rep.* **5**, 17843 (2015).

157. Cao, M., Jin, X., Peng, Y., Yu, C., Li, K., Liu, K. & Jiang, L. Unidirectional Wetting Properties on Multi-Bioinspired Magnetocontrollable Slippery Microcilia. *Adv. Mater.* **29**, 1606869 (2017).

158. Yang, C., Wu, L. & Li, G. Magnetically Responsive Superhydrophobic Surface: In Situ Reversible Switching of Water Droplet Wettability and Adhesion for Droplet Manipulation. *ACS Appl. Mater. Interfaces* **10**, 20150–20158 (2018).

159. Grigoryev, A., Tokarev, I., Kornev, K. G., Luzinov, I. & Minko, S. Superomniphobic magnetic microtextures with remote wetting control. *J. Am. Chem. Soc.* **134**, 12916–12919 (2012).

160. Ben, S., Tai, J., Ma, H., Peng, Y., Zhang, Y., Tian, D., Liu, K. & Jiang, L. Cilia-Inspired Flexible Arrays for Intelligent Transport of Viscoelastic Microspheres. *Adv. Funct. Mater.* **28**, 1706666 (2018).

161. Lin, Y., Hu, Z., Zhang, M., Xu, T., Feng, S., Jiang, L. & Zheng, Y. Magnetically Induced Low Adhesive Direction of Nano/Micropillar Arrays for Microdroplet Transport. *Adv. Funct. Mater.* **28**, 1800163 (2018).

162. Amato, L., Keller, S. S., Heiskanen, A., Dimaki, M., Emnéus, J., Boisen, A. & Tenje, M. Fabrication of high-aspect ratio SU-8 micropillar arrays. *Microelectron. Eng.* **98**, 483–487 (2012).

163. Chandra, D. & Yang, S. Capillary-force-induced clustering of micropillar arrays: Is it caused by isolated capillary bridges or by the lateral capillary meniscus interaction force? *Langmuir* **25**, 10430–10434 (2009).

164. Pokroy, B., Kang, S. H. & Aizenberg, J. Self-Organization of a Mesoscale Bristle into Ordered, Hierarchical Helical Assemblies. *Science* **323**, 237–240 (2009).

165. Adhikari, R., Kaundal, R., Sarkar, A., Rana, P. & Das, A. K. The cantilever beam magnetometer: A simple teaching tool for magnetic characterization. *Am. J. Phys.* **80**, 225–231 (2012).

166. Senturia, S. D. Microsystem Design. *Kluwer Academic Publishers* 207–217 (2001).

167. Judy, J. W., Muller, R. S. & Zappe, H. H. Magnetic Microactuation of Polysilicon Flexure Structures. *J. Microelectromechanical Syst.* **4**, 162–169 (1995).

168. Roca-Cusachs, P., Rico, F., Martínez, E., Toset, J., Farré, R. & Navajas, D. Stability of Microfabricated High Aspect Ratio Structures in Poly(dimethylsiloxane). *Langmuir* **21**, 5542–5548 (2005).

169. Xiang, Y. & LaVan, D. A. Analysis of soft cantilevers as force transducers. *Appl. Phys. Lett.* **90**, 133901 (2007).

170. Wang, Z., Volinsky, A. A. & Gallant, N. D. Crosslinking effect on polydimethylsiloxane elastic modulus measured by custom-built compression instrument. *J. Appl. Polym. Sci.* **131**, 41050 (2014).

171. Cenev, Z., Zhang, H., Sariola, V., Rahikkala, A., Liu, D., Santos, H. A. & Zhou, Q. Manipulating Superparamagnetic Microparticles with an Electromagnetic Needle. *Adv. Mater. Technol.* **3**, 1700177 (2018).

172. Mata, A., Fleischman, A. J. & Roy, S. Characterization of polydimethylsiloxane (PDMS) properties for biomedical micro/nanosystems. *Biomed. Microdevices* **7**, 281–293 (2005).

173. Kuo, A. C. M. Poly(dimethylsiloxane). *Polymer Data Handbook. Oxford University Press* 411– 435 (1999).

174. Wong, T. S., Kang, S. H., Tang, S. K. Y., Smythe, E. J., Hatton, B. D., Grinthal, A. & Aizenberg, J. Bioinspired self-repairing slippery surfaces with pressure-

stable omniphobicity. *Nature* **477**, 443–447 (2011).

175. Yao, X., Hu, Y., Grinthal, A., Wong, T. S., Mahadevan, L. & Aizenberg, J. Adaptive fluid-infused porous films with tunable transparency and wettability. *Nat. Mater.* **12**, 529–534 (2013).

176. Manna, U. & Lynn, D. M. Fabrication of Liquid-Infused Surfaces Using Reactive Polymer Multilayers: Principles for Manipulating the Behaviors and Mobilities of Aqueous Fluids on Slippery Liquid Interfaces. *Adv. Mater.* **27**, 3007–3012 (2015).

177. Zhang, X., Sun, L., Wang, Y., Bian, F., Wang, Y. & Zhao, Y. Multibioinspired slippery surfaces with wettable bump arrays for droplets pumping. *PNAS* **116**, 20863–20868 (2019).

178. Stöber, W., Fink, A. & Bohn, E. Controlled growth of monodisperse silica spheres in the micron size range. *J. Colloid Interface Sci.* **26**, 62–69 (1968).

179. Gorissen, B., de Volder, M. & Reynaerts, D. Pneumatically-actuated artificial cilia array for biomimetic fluid propulsion. *Lab Chip* **15**, 4348–4355 (2015).

180. Zhang, S., Cui, Z., Wang, Y. & den Toonder, J. M. J. Metachronal actuation of microscopic magnetic artificial cilia generates strong microfluidic pumping. *Lab Chip* **20**, 3569–3581 (2020).

181. den Toonder, J. M. J. & Onck, P. R. Microfluidic manipulation with artificial/bioinspired cilia. *Trends in Biotechnology* **31**, 85– 91 (2013).

182. Chen, D., Norris, D. & Ventikos, Y. Ciliary behaviour and mechano-transduction in the embryonic node: Computational testing of hypotheses. *Med. Eng. Phys.* **33**, 857–867 (2011).

183. Wang, Y. H., Chen, C. P., Chang, C. M., Lin, C. P., Lin, C. H., Fu, L. M. & Lee, C. Y. Microfluidics MEMS-based gas flow sensors. *Microfluid. Nanofluidics* **6**, 333–346 (2009).

184. Cubukcu, A. S., Zernickel, E., Buerklin, U. & Urban, G. A. A 2D thermal flow sensor with sub-mW power consumption. *Sensors Actuators, A Phys.* **163**, 449–456 (2010).

185. Kuo, J. T. W., Yu, L. & Meng, E. Micromachined Thermal Flow Sensors-A Review. *Micromachines* **3**, 550–573 (2012).

Errata

Publication I, page 3

The equation $F\mu = L/2(\cos\theta R - \cos\theta A)$ is missing a Parentheses. The correct form is $F\mu = (L/2)(\cos\theta R - \cos\theta A)$.

Publication I, page 6

In the Experimental Section, the value of the dose was incorrectly given as 3.18 J cm^{-2}. The correct dose value is 50 mJ cm^{-2}.

Publication III, page 6

In the last paragraph the application was incorrectly designated as micro-elastomer. The correct term is micro-elastometer.

BUSINESS +
ECONOMY

ART +
DESIGN +
ARCHITECTURE

SCIENCE +
TECHNOLOGY

CROSSOVER

DOCTORAL
DISSERTATIONS